Acta Pharmaceutica Sinica B 2026;16(4):1991−2028

Chinese Pharmaceutical Association
Institute of Materia Medica, Chinese Academy of Medical Sciences

Acta Pharmaceutica Sinica B

www.elsevier.com/locate/apsb
www.sciencedirect.com

REVIEW

Fluorescence bioimaging of drug nanocarriers based on Förster resonance energy transfer, aggregation-induced emission and aggregation-caused quenching

Runtong Zhang[a], Haisheng He[a], Yi Lu[a,c,d], Aun Raza[a,*], Wei Wu[a,b,c,d,*]

[a]*School of Pharmaceutical Sciences, Fudan University, Key Laboratory of Smart Drug Delivery of MOE and National Key Laboratory of Advanced Drug Formulations for Overcoming Delivery Barriers, Shanghai 201203, China*
[b]*Center for Medical Research and Innovation, Shanghai Pudong Hospital, Fudan University Pudong Medical Center, Shanghai 201399, China*
[c]*Shanghai Skin Disease Hospital, Tongji University School of Medicine, Shanghai 200443, China*
[d]*Fudan Zhangjiang Institute, Shanghai 201203, China*

Received 23 April 2025; received in revised form 18 June 2025; accepted 26 June 2025

KEY WORDS

Nanocarrier;
Drug delivery;
Fluorescence bioimaging;
Environment-responsive;
Förster resonance energy transfer;
Aggregation-induced emission;
Aggregation-caused quenching;
In vivo fate

Abstract The introduction of environment-responsive probes has greatly improved the accuracy of fluorescence bioimaging in evaluating drug nanocarriers. This review highlights the key roles of Förster resonance energy transfer, aggregation-induced emission, and aggregation-caused quenching in advancing nanomedicine. These technologies have enhanced our understanding of nanocarrier pharmacokinetics, biodistribution, and intracellular behavior, providing valuable insights for optimizing drug delivery systems. Their integration into imaging platforms has enabled precise monitoring of nanocarriers in complex biological environments. This review outlines detailed progress in the use of environment-responsive probes, emphasizing their importance in improving the design and effectiveness of nanomedicines. Looking forward, advances in probe engineering and multimodal imaging, combined with computational tools, are expected to drive the development of more targeted, efficient, and personalized therapeutic strategies.

This article is part of special issue entitled: Hot Topic Reviews in Drug Delivery (II) published in Acta Pharmaceutica Sinica B.
*Corresponding authors.
E-mail addresses: aunraza@fudan.edu.cn, razaaun1990@gmail.com (Aun Raza), wuwei@shmu.edu.cn (Wei Wu).
Peer review under the responsibility of Chinese Pharmaceutical Association and Institute of Materia Medica, Chinese Academy of Medical Sciences.

https://doi.org/10.1016/j.apsb.2025.10.023

1. Introduction

Over the past few decades, the field of drug delivery has experienced rapid and transformative advancements. Among various strategies, nanocarriers have emerged as a cornerstone for transporting therapeutic and diagnostic agents to targeted sites with improved efficacy. Nanocarrier drug delivery systems have become a major focus of research, as evidenced by the publication of tens of thousands of papers annually and substantial investment in the nanomedicine sector[1,2]. Despite the commercial approval of over 60 nanomedicine products, the clinical translation rate remains relatively low, revealing a significant disparity between research output and returns[3,4]. One of the key limiting factors is the insufficient understanding of the *in vivo* biological processes that govern nanocarrier behavior[2,5-7].

Elucidating the *in vivo* and subcellular dynamics of nanocarriers is essential for optimizing formulations, repurposing designs, conserving development resources, and accelerating clinical translation. Accurate spatiotemporal tracking of nanocarriers is critical for unraveling their interactions with both payloads and biological systems[2,5]. However, mapping these distributions remains challenging due to the nanoscale dimension and degradability of most carrier materials. Moreover, the major components of nanocarriers, such as lipids, polymers, and proteins, typically lack intrinsic imaging signals, necessitating the use of external probes, such as fluorophores and nuclides, to enable visualization[8].

Compared to radionuclide labeling, which requires specialized handling facilities and protocols, fluorophores offer a more accessible and versatile option for routine imaging studies[9,10]. Therefore, fluorescence bioimaging (FB) has emerged as a powerful technique for investigating the fundamental biological processes and mechanisms underlying diseases and therapeutic interventions. Fig. 1 outlines the wavelength ranges of different emission colors from ultraviolet to near-infrared (NIR), as well as the corresponding fields of applications. It is advised to refer to recent reviews for advances in FB[11-15]. One important branch of FB applications is bioimaging of drug nanocarriers[16-20].

FB allows for real-time tracking of nanocarrier translocation, assessment of targeting efficiency, and evaluation of biodistribution, cellular uptake, PK, and drug release[21-23]. These insights are of substantial pharmacological and toxicological importance[24-28]. Since most nanocarriers lack inherent fluorescence, they are commonly labeled with fluorophores *via* chemical conjugation or physical embedment. However, this labeling introduces new challenges, particularly the risk of probe detachment and constant emission, which can lead to inaccurate or misleading imaging results in complex biological environments[8,29-32].

To overcome these hurdles, the advent of environment-responsive fluorophores (ERFs) has significantly enhanced the accuracy of FB for nanocarrier studies[32-35]. ERFs alter their signals in response to environmental stimuli, allowing differentiation between intact carrier-associated signals and those from detached probes[8,32,33,36,37]. This capacity improves imaging precision and supports the quantification of nanocarriers *in vivo*[38-40]. To date, several ERF strategies have been successfully applied in FB, primarily Förster resonance energy transfer (FRET)[20,36,38,41], aggregation-caused quenching (ACQ)[32,33,39,40,42,43], and aggregation-induced emission (AIE)[44-46].

This review aims to provide a comprehensive overview of these ERFs, including their fundamental characteristics, environmental response mechanisms, imaging principles, and current applications in nanocarrier research.

2. Fundamental considerations for bioimaging nanocarriers using fluorescence techniques

Initially, fluorophores were directly employed to investigate biological processes. However, limitations such as poor water solubility, low stability, and non-specific distribution often hinder their direct application in bioimaging. To address these issues,

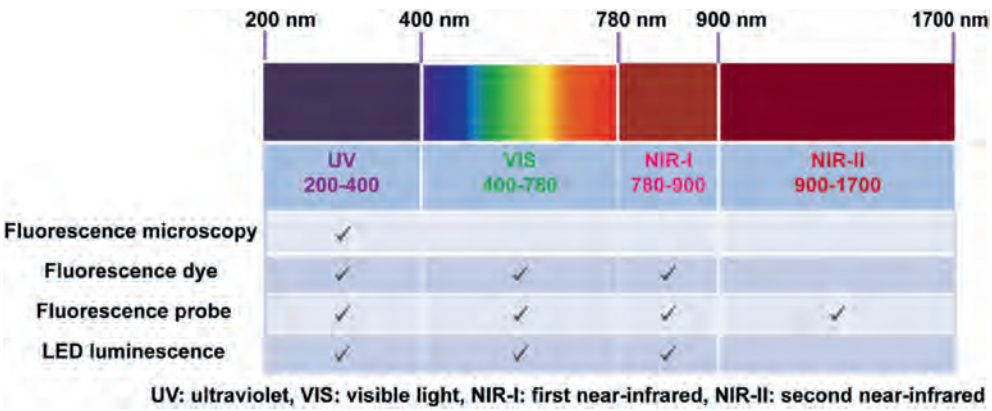

Figure 1 Operational wavelength ranges of fluorescence technologies. This schematic illustrates the spectral bands across the electromagnetic spectrum where fluorescence microscopy, dyes, probes, and light-emitting diodes (LEDs) operate. Checkmarks indicate the applicable technology for each spectral band.

nanocarriers are introduced to encapsulate and deliver fluorophores more effectively. Lipid or polymeric nanoparticles, micelles, and vesicles not only enhance the solubility and stability of fluorophores but also enable their targeted and controlled delivery to specific biological sites. These systems provide structural protection and facilitate more precise biodistribution of fluorophores, significantly improving imaging efficiency[13,14,47].

Targeted delivery can be achieved through various mechanisms, such as passive accumulation through natural uptake by the mononuclear phagocyte system (MPS), or *via* the enhanced permeation and retention (EPR) effect, especially in tumor tissues[40,48,49]. However, accurately attributing observed fluorescence signals to nanocarriers that have reached the target site *in vivo* remains a major challenge. Overcoming this is essential for reliable analysis of nanocarrier biodistribution and for achieving effective and specific illumination of target sites.

Both encapsulated and free fluorophores contribute to FB. When the focus of FB is to trace the nanocarriers themselves, the analytical precision becomes paramount. The presence of free or released probes can interfere with data interpretation, potentially leading to overestimation of nanocarrier accumulation or misleading spatial distribution patterns[30,50]. This issue, often referred to as fluorescence bias in FB, has become a central concern in recent studies[8,16].

Given the challenges associated with fluorophore behavior in biological systems, a thorough understanding of nanocarrier structure and labeling strategies is essential. Such knowledge not only aids in mitigating analytical bias but also enhances the overall accuracy and efficacy of fluorescence-based tracking. The following sections will provide a detailed discussion on the structural classification of nanocarriers, diverse fluorescence labeling strategies, and the key challenges currently faced in this field, offering a comprehensive overview of the state and future directions of nanocarrier bioimaging *via* fluorescence techniques.

2.1. *Structural classification of nanocarriers*

Understanding the structural classification of nanocarriers is essential for the effective implementation of fluorescence labeling strategies. Statistics indicate that the majority of clinically approved or development-stage drug nanocarriers are composed of biodegradable materials, primarily including lipids, polymers, and proteins[1,3,4]. The structural design of these nanocarriers varies considerably depending on the physicochemical properties of the constituent materials and the specific objectives of drug delivery. These structural variations play a pivotal role in determining appropriate probe labeling strategies for FB. Fig. 2 illustrates the fundamental structures of commonly studied drug nanocarriers.

To provide a clearer understanding of fluorescence labeling methods, drug nanocarriers are classified into distinct categories based on their structural characteristics, as illustrated in Fig. 2. These include: 1) micelles; 2) vesicles; 3) matrices; 4) drug particles, further subdivided into crystalline and amorphous types; and 5) inorganic nanocarriers.

Micelles are formed by the self-assembly of a single layer of amphiphiles, such as surfactants and copolymers, with sizes ranging from a few to more than one hundred nanometers and a hydrophobic/hydrophilic "core/shell" structure[29]. Probes can be chemically conjugated to the hydrophilic or hydrophobic ends of amphiphilic molecules[51] or physically embedded into the hydrophobic cores[52].

Vesicles, also self-assembled systems, are composed of bilayers of lipids and/or lipid derivatives. Their unique architecture comprises a hydrophobic bilayer and an aqueous internal cavity, allowing encapsulation of both hydrophilic and hydrophobic agents[53]. Common examples include liposomes, niosomes, and extracellular vesicles (EVs), all of which are extensively investigated for drug delivery applications[54].

Matrix-based nanocarriers consist of solid matrices constructed from biocompatible and biodegradable materials, including lipids, polymers, or proteins. These carriers typically have a uniform structure and can accommodate both hydrophilic and hydrophobic agents, depending on the material properties. Notably, when pure drug crystals are downsized to the nanometer scale, they can form nanoparticles with solid matrices. These drug nanoparticles are generally referred to as nanosuspensions, regardless of the physical state of the drug molecules (whether crystalline or amorphous), or as nanocrystals (NCs) specifically in the case of crystalline forms[55].

Inorganic nanoparticles form a distinct class. For example, "Ferumoxytol" stands as a successfully marketed nanomedicine based on inorganic iron oxide nanoparticles, its primary use is as an intravenous therapy for iron deficiency anemia in adults with chronic kidney disease[56,57]. However, there is a noticeable gap in research regarding the use of this type of nanoparticle as a drug nanocarrier since inorganic materials are usually non-degradable with poor biocompatibility and toxicity.

Additionally, hybrid nanocarriers, which integrate features from multiple types of fundamental systems, are gaining attention for their potential to optimize drug loading, stability, and release characteristics[58].

The structural diversity of nanocarriers presents both opportunities and challenges in fluorescence labeling. Each nanocarrier type demands tailored labeling strategies to ensure accurate, efficient, and stable probe integration, which is essential for reliable fluorescence-based tracking in complex biological environments.

2.2. *Strategies for fluorescence labeling*

Given the complexity of nanocarrier systems, the development of an effective fluorescence labeling strategy requires a customized approach, considering the unique characteristics of both the nanocarriers and the probes to achieve practical and efficient outcomes. Fig. 3 summarizes commonly utilized strategies for fluorescence labeling of nanocarriers.

Some nanocarriers, such as quantum dots and carbon dots, exhibit intrinsic fluorescence, enabling self-illumination and simplifying imaging workflows[11,59]. In certain cases, the drug payload itself exhibits strong autofluorescence to facilitate bioimaging[60,61]. However, in most applications where neither the nanocarrier nor the drug possesses inherent fluorescence, exogenous fluorophores must be introduced to visualize nanocarrier biodistribution and behavior. Two primary labeling strategies are employed: chemical conjugation and physical embedding. Chemical conjugation, though more synthetically complex, offers superior labeling stability by covalently anchoring fluorophores to nanocarrier components[62]. In contrast, physical embedment, where fluorophores are loaded into nanocarriers *via* non-covalent interactions, is a simpler process but may suffer from reduced stability, especially if the affinity between the fluorophore and the carrier matrix is insufficient[63]. Both strategies are vulnerable to probe leakage during nanocarrier biodegradation, a frequent

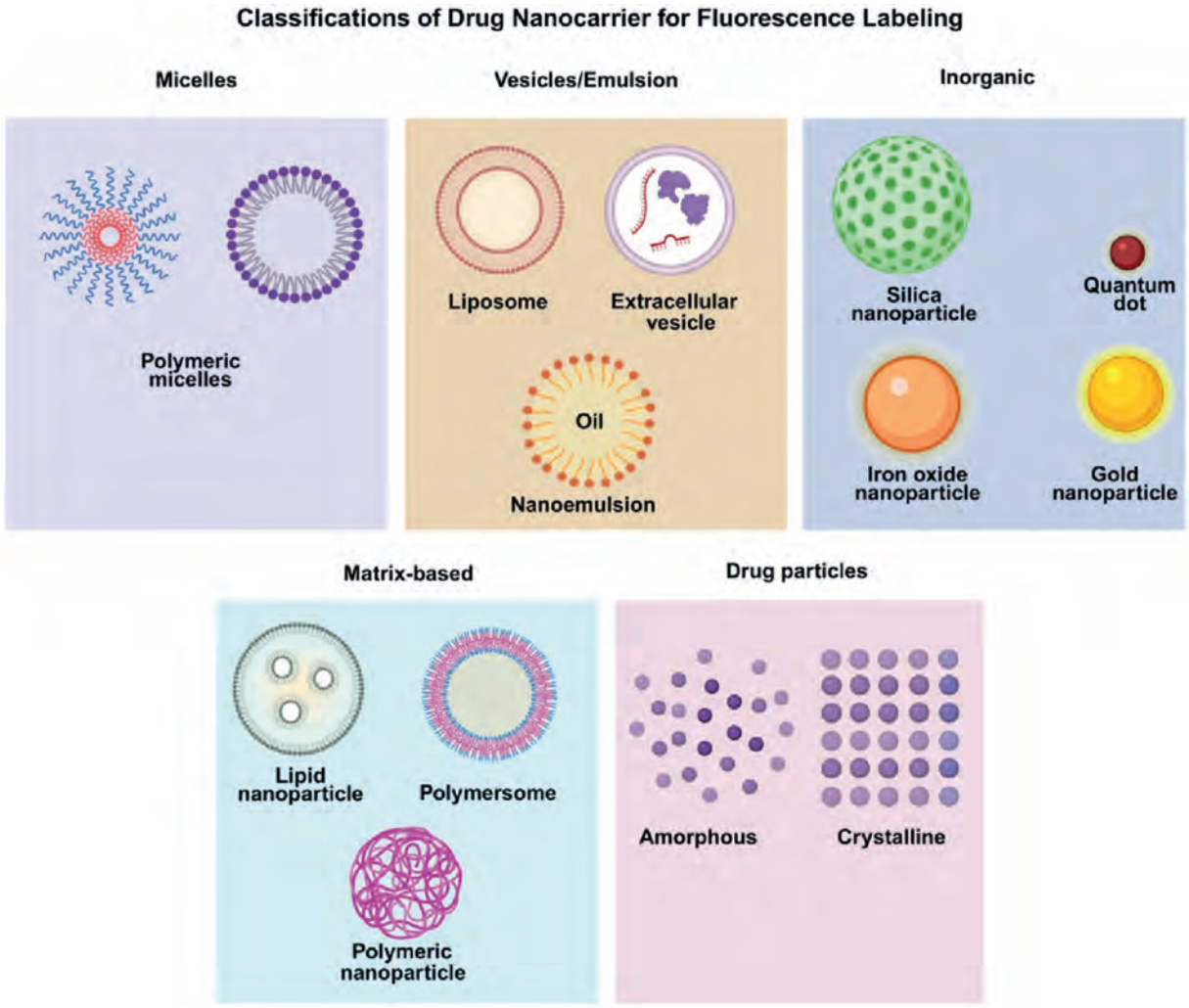

Figure 2 Classification of nanocarriers for fluorescent labeling in drug delivery. This diagram categorizes nanocarriers into five distinct types: (1) Micelles (polymer structures and small-molecule surfactants) for solubilizing hydrophobic drugs; (2) Vesicles (encompassing liposomes and extracellular vesicles (EVs)) for encapsulating therapeutic agents; (3) Inorganic nanoparticles (including silica and metal-based types) for precision targeting; (4) Matrix-based carriers (such as lipid and polymer constructs) for sustained release; and (5) Drug particles (depicted as amorphous or crystalline) for diverse dissolution profiles. These systems represent cutting-edge nanomedicine, offering tailored solutions for advanced therapeutic and diagnostic applications.

concern given the widespread use of biodegradable organic materials in drug delivery systems[8,9,33].

The choice between chemical and physical labeling strategies depends on several factors, including the availability of conjugation sites, internal space within the nanocarrier, and the specific goals of the experimental design[64,65]. For example, in the case of liposomes, fluorophores can either be chemically attached to phospholipids or other components[66], or physically embedded into the lipid bilayers using lipophilic fluorescent dyes[67]. Additionally, concentration-dependent quenching/dequenching effects can be harnessed by encapsulating water-soluble fluorophores within the aqueous core of liposomes, allowing for real-time monitoring of structural integrity under physiological or stress conditions[68,69].

The physicochemical composition of nanocarriers strongly influences probe loading efficiency and signal fidelity. Lipid-based systems (*e.g.*, liposomes, SLNs, nanoemulsions) offer high affinity for hydrophobic probes *via* physical embedment in lipid bilayers or cores. However, lipid fluidity and susceptibility to enzymatic degradation (*e.g.*, lipases) may cause probe leakage. For instance, ACQ studies have shown that SLN lacking lipase inhibitor (orlistat) degrade rapidly, compromising fluorescence stability[70]. Polymeric nanocarriers (*e.g.*, PLGA, PEG-PCL) offer tunable covalent conjugation sites for probes (*e.g.*, Cy5, FITC), enhancing label stability. Nevertheless, their degradation *via* hydrolysis or enzyme-triggered breakdown influences fluorophore retention over time. Inorganic carriers (*e.g.*, silica, iron oxide) possess rigid matrices that minimize leakage, though they face limitations in terms of biocompatibility and functional versatility. This challenge can be mitigated through the development of hybrid systems that combine inorganic cores with organic coatings (*e.g.*, lipid shells), thereby enhancing biocompatibility while maintaining structural integrity[71].

The diverse array of fluorescent probe labeling strategies outlined above provides researchers with diverse choices for tracking

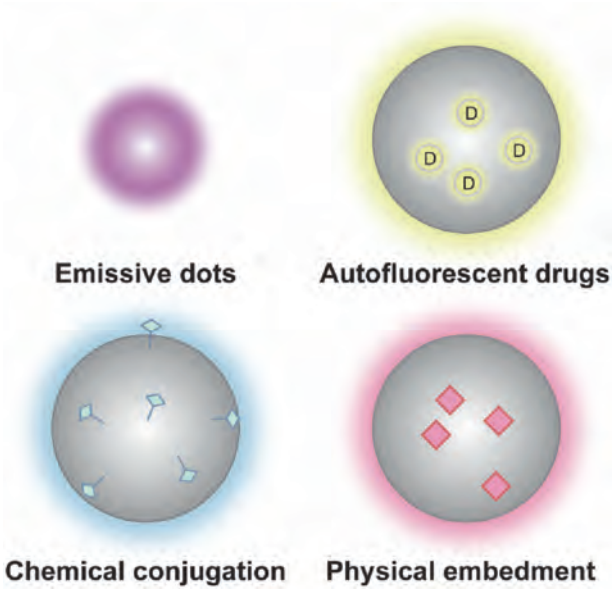

Figure 3 Labeling techniques for nanocarriers. This figure illustrates strategies used to label nanocarriers for imaging and tracking: emissive dots denote intrinsically fluorescent nanocarriers; autofluorescent drugs represent carriers incorporating naturally fluorescent therapeutics; chemical conjugation indicates covalent tagging with fluorescent dyes; and physical embedment shows nanocarriers with dyes physically encapsulated within their matrix.

nanocarriers *in vivo*, while the practical implementation of bioimaging for reliably deciphering nanocarrier fate remains fraught with substantial challenges. Merely attaching a detectable label to nanocarriers does not guarantee the acquisition of accurate physiologically relevant data. Crucially, the very act of labeling, the complex biological milieu encountered *in vivo*, and the intrinsic limitations of imaging technologies introduce a constellation of confounding factors that can profoundly compromise data interpretation. Therefore, the following section delves into some critical bioimaging challenges.

2.3. Challenges

The primary objective in FB tracking of drug nanocarriers is to elucidate their spatiotemporal behavior within biological environments. At its fundamental level, this involves visualizing the *in vivo* journey of nanocarriers, a concept encapsulated by the widely embraced paradigm "seeing is believing". In this qualitative phase, nanocarrier biodistribution can be "seen" through fluorescent visualization using sophisticated equipment like fluorescence microscopes and *in vivo* imaging systems (IVIS).

Building on this visual foundation, researchers often proceed to quantitative analysis[72], under the assumption that fluorescence intensity correlates proportionally with the quantity of nanocarriers[73]. Accordingly, profiling fluorescence over time has become a standard practice in FB, which is typically regarded as a semi-quantitative or quantitative analysis[52].

Recent advancements have enabled the use of fluorescence for PK analysis of nanocarriers. However, increasing scrutiny has highlighted the limitations of this approach, with concerns raised about the accuracy and interpretability of FB-derived data[8,16,30,50]. The reliability of fluorescence readouts can be undermined by several critical factors, notably the limited tissue penetration due to light absorption and scattering[74], and more problematically, the leakage or release of fluorescent probes from their nanocarrier matrices, which can significantly affect the accuracy of the imaging[75].

In the FB of nanocarriers, the observed fluorescence is typically interpreted as representing the nanocarriers themselves, without differentiating between the carriers and other sources. However, the accuracy of this bioimaging can be compromised if the probes detach from the nanocarriers. In cases where nanocarriers are nondegradable and the fluorophores are securely attached without leaking, the fluorescence signals can accurately represent the nanocarriers. This assumes that other biological factors, like tissue autofluorescence, are minimized, which can be achieved by optimizing probe structures, such as extending emission wavelengths into the NIR regions I and II. However, this scenario is relatively uncommon, as nondegradable nanocarriers are typically used as tools, while degradable nanocarriers are more favored in the development of nanocarrier drug delivery. With degradable nanocarriers, probe leakage is almost inevitable as the carrier degrades. The fluorescence from free or released probes then becomes a significant source of interference in FB.

Although the aforementioned labeling strategies offer researchers a wide range of tools for *in vivo* tracking, the practical challenge lies in achieving accurate and physiologically meaningful imaging. Simply tagging a nanocarrier with a fluorophore does not ensure reliable interpretation. The complex *in vivo* environment, inherent limitations of imaging modalities, and the physicochemical interactions between probes and nanocarriers collectively introduce substantial uncertainty. These confounding variables highlight a critical need for more refined imaging approaches that can distinguish between intact nanocarriers and dissociated probes.

To address these challenges, the development of ERFs offers a potential solution. These probes are responsive enough to exhibit markedly different fluorescence characteristics within the nanocarrier body compared to the surrounding environment, enabling differentiation between signals originating from intact nanocarriers and those from released or free probes. The subsequent sections will detail the operational principles of three types of ERFs based on FRET, AIE, and ACQ.

3. FRET

3.1. Rationale of FRET and FRET-based nanocarrier imaging

FRET is a nonradiative energy transfer process mediated by long-range dipole-dipole interactions between specific molecules, referred to as the donor and the acceptor, or the FRET pair[76]. This interaction occurs when the donor and acceptor, both in their ground states, are in close spatial proximity, typically within 1 to 10 nm[77]. FRET can be understood through the integration of quantum physics with the classical understanding of Coulombic dipole-dipole interactions. As depicted in Fig. 4A, energy transfer involves the acceptor receiving energy from the donor upon excitation, causing the acceptor to transition to the excited state without photon involvement[78]. If the acceptor possesses a negligible quantum yield, the resulting fluorescence will either diminish or disappear entirely. Alternatively, if the acceptor is also a fluorophore, its emission spectrum typically undergoes a redshift[79], a phenomenon widely exploited in practical applications.

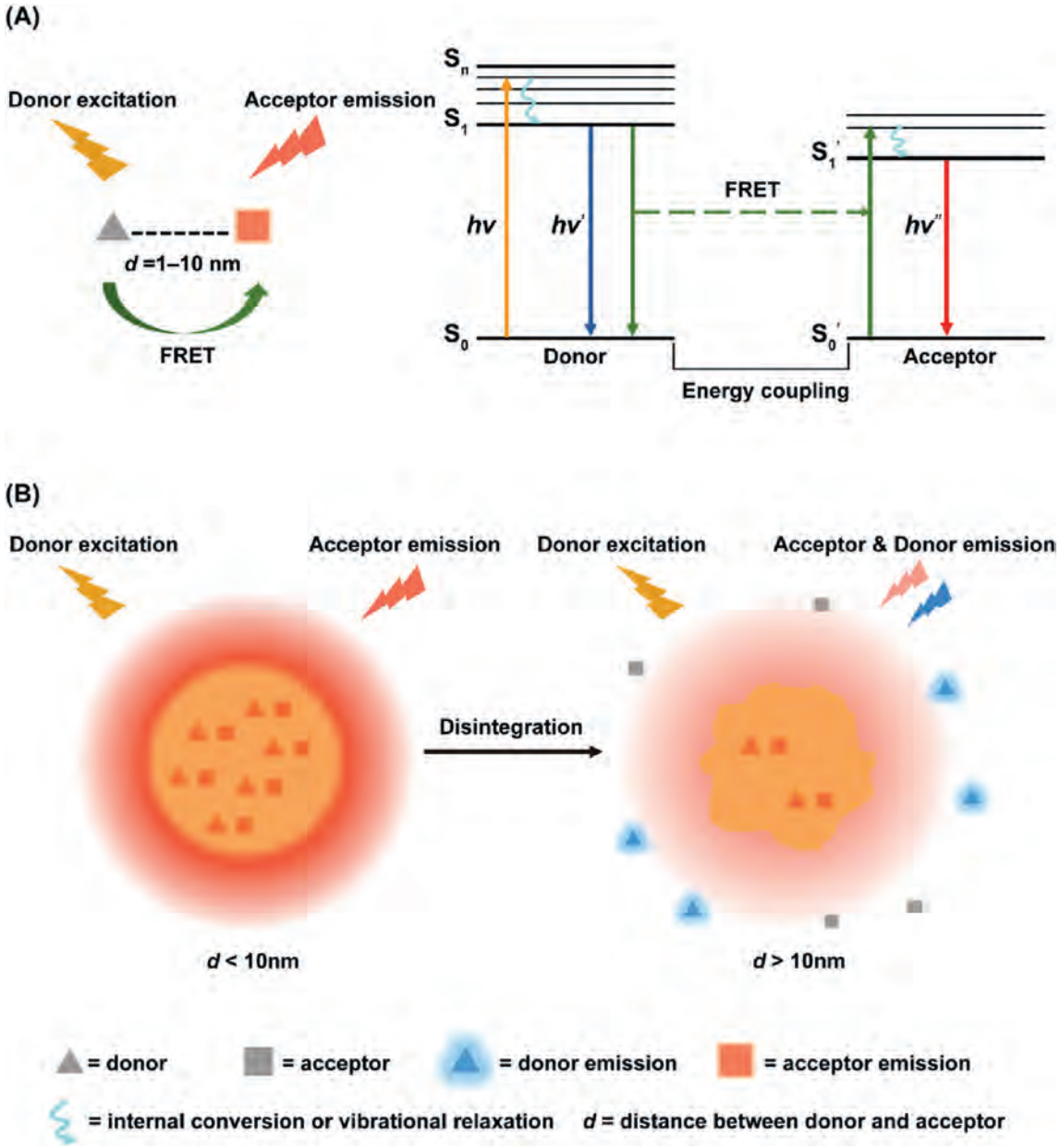

Figure 4 Fundamental principles of FRET-based bioimaging. (A) FRET mechanism illustrated *via* Jablonski diagram: electrons in the ground state (S_0) absorb energy and excite to higher states (S_n). Through non-radiative transitions (internal conversion and vibrational relaxation), they relax to the lowest singlet excited state (S_1). From S_1, electrons return to S_0 *via* either: (i) non-radiative FRET (quenching donor fluorescence), or (ii) radiative transition (producing fluorescence). (B) FRET-pair labeling strategy for nanocarriers: intact nanocarriers maintain proximity between FRET pairs, enabling energy transfer and acceptor fluorescence. Partial disassembly separates FRET pairs into the aqueous environment, halting energy transfer and ceasing acceptor emission.

To extend the effective range of FRET beyond its typical ~10 nm limit, researchers have developed systems involving triple or even multiple FRET probes[80,81]. In a triple FRET system, energy is first transferred between a donor-acceptor pair with short-wavelength absorption, and the first acceptor then serves as the donor for a second transfer[82]. However, such multi-step configurations significantly increase analytical complexity. As a result, dual FRET systems involving only two fluorophores remain the most commonly used in FB due to their simplicity and effectiveness[83].

FRET efficiency is influenced not only by the distance between donor and acceptor but also by their relative orientation, particularly the alignment of their absorption and emission dipole moments[84]. To minimize orientation effects, the fluorophores are often rigidly attached to target molecules[65]. Furthermore, flexible linkers are frequently employed in labeling strategies. These linkers help maintain a consistent donor-acceptor distance within a few nanometers and reduce the impact of unfavorable orientation, ensuring effective FRET for bioimaging applications[77].

FRET processes can be classified into two types: hetero-FRET, which occurs between different chromophores, and homo-FRET, which occurs between identical fluorophores. Although homo-FRET can be detected *via* changes in fluorescence anisotropy, it is less commonly used than hetero-FRET. Nevertheless, both types share similar mechanisms and applications[85]. This review focuses exclusively on hetero-FRET.

FRET was initially observed by Cario and Franck in 1922 when they noted the fluorescence emission of thallium at the excitation wavelength of mercury[86]. However, the term FRET is named after Theodor Förster, who, in 1948, derived the theoretical foundation and quantitative equation describing energy transfer efficiency as a function of distance between donor and acceptor[87]. Initially, FRET had limited impact in biology, but its potential was gradually recognized through the work of pioneers like Lubert Stryer[86]. He proposed using FRET as a molecular ruler and emphasized the importance of spectral overlap, which brought new dimensions to the study of biological macromolecules[88]. Stryer also highlighted several critical considerations for using FRET in studying biological macromolecules. These included the pre-calibration of donor and acceptor pairs, strategies for selectively attaching a single donor and a single acceptor to a molecule, and the assessment of the relative orientation information of the donor and acceptor pair[89]. In nanoparticle labeling, however, these considerations are often neglected. For example, the orientation information between the labeled donor and acceptor is frequently overlooked, and the focus is primarily on using FRET's molecular ruler capability to determine the integrity of nanocarriers.

FRET has been widely used to monitor biomolecular interactions, including protein-protein interactions[90], protein-DNA interactions[91], and protein conformational changes[92]. For instance, when analyzing biomacromolecules with varying chain lengths, employing amino acids as spacers can provide insights into the flexibility of different regions within the three-dimensional structure of a protein. This approach allows for a detailed examination of how various segments of the protein behave and interact, contributing to a deeper understanding of its overall structural dynamics[93]. Moreover, FRET is often combined with other optical techniques, such as fluorescence correlation spectroscopy[94], confocal fluorescence-lifetime single molecule localization microscopy[95], and two-photon microscopy[96], to reveal the dynamics and interaction of fluorescently labeled molecules more accurately. Furthermore, the distinct qualities of FRET make it an appropriate technique for a range of probes tailored to identify specific analytes. Its capability extends to the simultaneous detection of multiple analytes[87]. For example, FRET can be used to concurrently track the production of endogenous nitric oxide and hydrogen peroxide in macrophages, employing a sensing mechanism akin to a logic gate. This multi-analyte detection feature significantly broadens the applicability of FRET in various analytical contexts[97]. Indeed, assessing the integrity of nanocarriers represents a relatively recent and limited aspect of FRET's broader applications in the field of biology.

From the above description, we can perceive that the occurrence of FRET phenomenon needs to meet some conditions: 1) there should be a great overlap between the emission spectrum of the donor and the absorption of the acceptor; 2) donor and acceptor molecules must be arranged at a sufficiently close distance properly; and 3) an appropriate FRET pair should have sufficient quantum yield, extinction coefficient, and capacity to resist disturbance. Designing FRET systems that fulfill all these criteria is challenging and underscores the precision required in FRET-based studies.

FRET is a valuable tool in studying the integrity of nanocarriers due to its high sensitivity to changes in the distance between donors and acceptors (Fig. 4B)[98]. It has been used to study the *in vitro* integrity of nanocarriers in different solutions or *in vivo* integrity after different routes of administration, especially regarding nanocarrier stability in blood circulation[38,99], distribution in organs, and spatiotemporal degradation kinetics[65,71,100].

FRET efficiency is defined as the proportion of photons absorbed by the donor fluorophore that are subsequently transferred to the acceptor. This efficiency depends on several factors, including the spectral overlap between the donor's emission and the acceptor's absorption, the distance between the donor and acceptor, and their dipole-dipole interactions[101]. It can be calculated as shown in Eq. (1):

$$E_{\mathrm{FRET}} = \frac{R_0^6}{R_0^6 + R^6} \tag{1}$$

where R stands for the distance between the two molecules and R_0, known as the Förster distance or critical transfer distance.

To be specific, R_0 is a characteristic separation between a donor and acceptor fluorophores at which the efficiency of FRET is 50%. It is defined as the donor-acceptor separation distance at which the rate of energy transfer equals the rate of donor excited-state decay in the absence of acceptor. R_0 is an intrinsic property of the specific FRET pair and their local environment, determined by the spectroscopic properties of the donor-acceptor pair and their environment, as shown in Eq. (2) [102]:

$$R_0^6 = 8.785 \times 10^{-5} \frac{\kappa^2 \phi_{\mathrm{D}} J}{n^4} \tag{2}$$

(κ^2, the orientation factor between donor emission and acceptor absorption transition dipoles. ϕ_{D}: the quantum yield of the donor in the absence of acceptor. J, the spectral overlap integral, quantifying the degree of overlap between the donor's normalized fluorescence spectrum and the acceptor's molar absorption coefficient spectrum. n, the refractive index of the medium surrounding the chromophores.)

Crucially, R_0 serves as the fundamental reference scale for converting measured efficiencies into absolute distance estimates, governed by Eq. (1)[102]. Consequently, the sensitivity E_{FRET} to distance change is highest when R is near R_0. Distances significantly shorter or longer than R_0 yield E_{FRET} close to 100% or 0%, respectively, providing little precise distance information. Thus, selecting a FRET pair with an R_0 matching the desired distance range of the system under study is critical for obtaining meaningful and sensitive distance measurements *via* FRET efficiency[102].

In practical experiments, FRET efficiency can also be determined by the fluorescence intensity or lifetime of the donor molecule, and the equations are as shown in Eqs. (3) and (4):

$$E_{\mathrm{FRET}} = 1 - \left(\frac{I_{\mathrm{DA}}}{I_{\mathrm{D}}}\right) \tag{3}$$

$$E_{\mathrm{FRET}} = 1 - \left(\frac{\tau_{\mathrm{DA}}}{\tau_{\mathrm{D}}}\right) \tag{4}$$

(I_{DA}: intensity of donor in presence of acceptor; I_{D}: intensity of donor only; τ_{DA}: lifetime of donor in presence of acceptor; τ_{D}: lifetime of donor only)[77]. Therefore, the calculation formula of E_{FRET} can be flexibly selected according to the experimental needs and testing instruments.

The accuracy of FRET efficiency measurements can be influenced by various factors, including the molecular brightness of the fluorophore and the stoichiometry ratio between fluorophores[103]. Additionally, cross-talk or bleed-through, such as detecting donor signals in the acceptor channel, can significantly affect measurements. To refine FRET efficiency calculations, techniques like alternating laser excitation (ALEX) or pulsed interleaved excitation (PIE) are used to mitigate interference and enhance measurement precision[104]. These methods help address the challenges posed by the inherent complexities in FRET analysis.

Accurate measurement of FRET efficiency employs several methodologies. The most common approaches quantify changes in donor fluorescence[105] or lifetime upon the presence and absence of acceptors[106]. Alternatively, researchers can measure the donor fluorescence before and after acceptor photobleaching[93]. The three-cube method provides another route that can be calibrated by fluorescence lifetime imaging microscopy (FLIM)-FRET or acceptor bleaching[107,108]. More recently, photon-effective FRET techniques enable simultaneous monitoring of donors and acceptors' signals[109], facilitating concurrent quantification of FRET efficiency and the quantities of fluorophores. Integration with two-photon excitation further allows optimization of excitation wavelengths for improved signal-to-noise ratios (SNR)[110]. Additionally, fluorescence anisotropy measurements directly gauge energy transfer efficiency by observing alterations in anisotropy[111].

While the methodologies described above enable precise quantification of FRET efficiency, their application for routinely monitoring nanocarrier integrity is often impractical due to demanding instrumentation and sample requirements. Consequently, the FRET proximity ratio (PR), a semi-quantitative measure, as shown in Eq. (5), is often used to determine the integrity of nanocarriers[100]:

$$\mathrm{PR} = \frac{A}{(A+D)} \tag{5}$$

where A and D are the maximum fluorescence intensity of the FRET acceptor and donor signals, respectively[38,58,100]. This approach accounts for the critical limitation that direct excitation of the acceptor by the donor excitation wavelengths compromises the reliability of using the acceptor alone to assess FRET efficiency or nanocarrier integrity.

Although a stable PR is often interpreted as an indicator of intact nanocarriers, some researchers argue that using the FRET ratio for this purpose is overly simplistic and fails to consider factors like fluorescence self-quenching. To address this, some mathematical formulas were developed through simulation-based methods to quantify the integrity of nanocarrier[99]. The method involves combining empty, single-labeled, and FRET-labeled nanocarriers at a known ratio to construct calibration curves. These models help quantify the proportion of intact nanocarrier[99], and have been widely adopted[41,100]. However, their accuracy can be limited by differences between simulated and actual degradation behavior of nanocarriers and the sensitivity of regression models to data fluctuations. Moreover, recalibration is often necessary for different nanocarrier types or materials[41]. Currently, FRET-based methods remain the standard for assessing nanocarrier integrity, though a more universally accepted strategy is needed, one that more directly correlates FRET signals with nanocarrier stability under physiological conditions.

3.2. *Typical FRET pairs*

Table 1 ([38,41,58,65,99,100,112-118]) presents representative FRET pairs commonly employed in bioimaging studies, illustrating the diversity of fluorophore combinations used in different contexts. Considerable efforts have been dedicated to optimizing existing FRET systems and developing novel FRET pairs to improve sensitivity, specificity, and compatibility with biological environments. For example, Kilin and co-workers[119] substituted the bulky hydrophobic tetraphenylborate (TPB) for the perchlorate counterion to increase the loading effectiveness of carbocyanine dyes into the lipid core of nanodroplets and generate a noticeable FRET signal. Such substitution improves the solubility of dyes in oil and then increases the loading of dyes.

On the other hand, small-Stokes-shift (SSS) fluorophores, due to the considerable overlap between their absorption and emission spectra, can undergo reabsorption of emitted energy by nearby fluorophores, leading to self-quenching, redshifted emission spectra, and increased background interference during imaging. Therefore, to prevent self-quenching and light scattering during the process of biological imaging[120] fluorophores with a large Stokes shift (LSS, typically larger than 80 nm, while 55 to 80 nm is acceptable) are preferred[121,122]. In response, several FRET pairs with LSS have been developed to improve imaging fidelity[99].

Another consideration is concentration quenching, a common property of many fluorophores, which leads to nonlinear relationships between fluorophore concentration and fluorescence intensity. This phenomenon necessitates careful optimization of the probe loading ratio within nanocarriers to ensure accurate signal interpretation[123]. To increase the measurement range, new FRET pairs have been designed using fluorophores with AIE properties[124]. These fluorophores exhibit enhanced fluorescence upon aggregation, making them especially advantageous for applications where conventional dyes suffer from quenching at high local concentrations.

3.3. *Application of FRET in nanocarrier bioimaging*

FRET significantly advances our comprehension of nanocarrier dynamics in bioimaging. A deep exploration into FRET's role reveals its effectiveness in a spectrum of nanocarrier types, including lipid nanocapsules (LNCs), micelles, and others. The focus here is on how FRET contributes to a deeper understanding of the molecular interactions and complexities in varied biological settings, showcasing its pivotal role in nanocarrier bioimaging.

3.3.1. *LNCs*

This section presents a comprehensive analysis of the pivotal role that FRET technology plays in deepening our understanding of LNCs, with a particular focus on their PK, stability, and biodistribution.

In a landmark study, FRET probes 1,1′-dioctadecyl-3,3,3′,3′-tetramethylindocarbocyanine perchlorate (DiI)-TPB and 1,1′-dioctadecyl-3,3,3′,3′-tetramethylindodicarbocyanine perchlorate (DiD)-TPB were utilized to investigate the PK of intact LNCs differing in size (50 *vs.* 85 nm) and surface coatings (uncoated, DSPE-mPEG 2000, and stearylamine) following intravenous administration in rats[38]. By defining intact LNCs through a *PR* ratio ranging from 0.86 to 0.93, as established in previous work[36], the researchers developed a robust method for tracking LNCs using FRET combined with nanoparticle tracking analysis (NTA) to measure intact LNC concentration. They also developed a new

Table 1 Typical FRET pairs utilized in bioimaging investigations.

Donor ($\lambda_{ex}/\lambda_{em}$) (nm/nm)	Acceptor ($\lambda_{ex}/\lambda_{em}$) (nm/nm)	Ref.
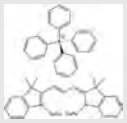 DiI-TPB (548/569)	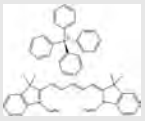 DiD-TPB (644/675)	38
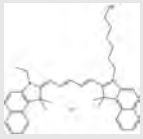 Cy 5.5 (640/710)	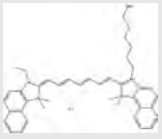 Cy7.5 (788/815)	41
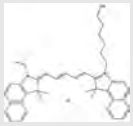 Cy 5.5 (640/660)	 Cy7 (660/750)	58
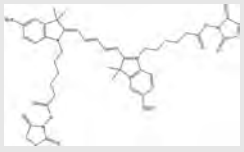 Cy5 (640/680)	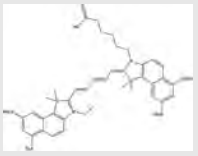 Cy5.5 (680/720)	65
 NBD-X (475/535)	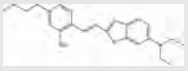 MS735 (545/735)	99
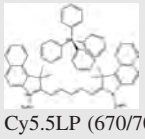 Cy5.5LP (670/700)	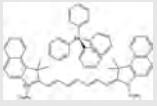 Cy7.5Lp (760/840)	100
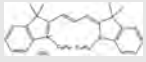 DiI (550/570)	 DiD (650/670)	112
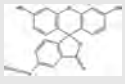 FITC (488/520)	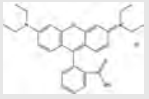 Rhod B (555/585)	113
 DiO (484/501)	 DiI (549/565)	114
 DiD (644/665)	 DiR (748/780)	115
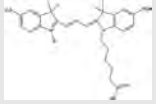 Cy3 (550/568)	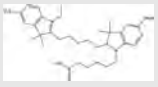 Cy5 (646/667)	116
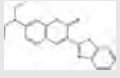 C6 (452/566)	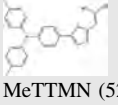 MeTTMN (520/664)	117
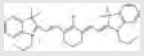 IR-780-PDMS (627/750)	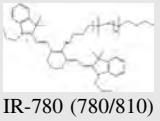 IR-780 (780/810)	118

C6, coumarin 6; Cy 3, cyanine dye 3; Cy 5, cyanine dye 5; Cy 5.5, cyanine dye 5.5; Cy5.5 LP, lipophilic Cy5.5; Cy7, cyanine dye 7; Cy7.5, cyanine dye 7.5; Cy7.5 LP, lipophilic Cy7.5; DiD, 1,1′-dioctadecyl-3,3,3′,3′-tetramethylindodicarbocyanine perchlorate; DiI, 1,1′-dioctadecyl-3,3,3′,3′-tetramethylindocarbocyanine perchlorate; DiO, 3,3′-dioctadecyloxacarbocyanine perchlorate; DiR, 1,1′-dioctadecyl-3,3,3′,3′-tetramethylindotricarbocyaine iodide; FITC,

method using sucrose density gradient centrifugation for extracting LNCs from blood, avoiding biological matrix interference[38]. PK data underwent noncompartmental analysis, followed by creation of a population PK model. Importantly, the study revealed that LNC elimination is nonlinear and influenced by both size and surface chemistry, with particle size primarily governing biodistribution[38]. These findings underscore the critical influence of physicochemical parameters on nanocarrier fate, reinforcing the need for tailored designs to optimize therapeutic delivery.

Another key investigation applied a FRET pair (DiI and DiD) to examine LNC stability within the gastrointestinal tract (GIT) mucus layer, a known barrier to oral drug delivery[112]. The experimental FRET efficiency is calculated as shown in Eq. (6):

$$E\,(\%) = \left(1 - \frac{y_D}{X_D}\right) \times 100\% \tag{6}$$

where y_D and x_D are the fitting terms associated with donor emission spectra and absorbance spectra, and a major loss of FRET efficiency suggests the destruction of nanocarriers ($E < 25\%$). The study demonstrated that Taxol®-loaded intact LNCs stability and diffusion in mucus are not size-dependent[112]. This challenges conventional assumptions about size-governed transport and highlights the unique interplay between mucus and nanocarrier surface characteristics. The results provide essential guidance for designing LNCs intended for oral administration by prioritizing mucus-interaction over mere size reduction.

Expanding on FRET's quantitative potential, subsequent research refined methods for estimating the proportion of intact FRET nanocarriers by generating calibration curves from mixtures of FRET-, DiI-, and DiD-loaded LNCs[125]. This approach enabled accurate *in vitro* and *in vivo* analysis of FRET nanocarriers' behavior as well as their encapsulation stability[125]. The data revealed that serum exerts a particularly disruptive effect on LNC stability, whereas LNCs can maintain integrity for a longer time after being internalized in cells or injected intravenously than lipid nanoemulsions[125]. These insights provide a nuanced understanding of nanocarrier-environment interactions and support the design of delivery systems that can withstand systemic and intracellular conditions.

In conclusion, this section presents the role of FRET in understanding the dynamics of LNCs, emphasizing their PK properties and interaction with various environments. This analysis illustrates the importance of advanced research in nanocarrier design for improved medical applications.

3.3.2. Micelles

The stability of micelles in the bloodstream is critical for effective drug delivery, as premature disintegration results in uncontrolled release of therapeutics, undermining the precision and efficacy of micelles[126,127]. To address such challenges, researchers have employed FRET as a powerful tool to probe micellar integrity across various biological contexts.

One significant advancement involves the use of LSS fluorophores such as succinimidyl 6-(*N*-(7-nitrobenz-2-oxa-1,3-diazol-4-yl) amino)hexanoate (NBD-X) and 1-(3-azidopropyl)-4-{2-[6-(diethylamino)-2-benzofuranyl]ethenyl}-3-sulfopyridinium inner salt (MS735), conjugated to polyethylene glycol-*block*-poly(ε-caprolactone) (PEG-PCL), serving as donor and acceptor, respectively, to more effectively assess the integrity of PEG-PCL micelles[99]. By optimizing donor-to-acceptor ratios to avoid self-quenching, researchers achieved more reliable measurements of micellar integrity, as shown in Eq. (7):

$$\text{Integrity}\,(\%) = \left[150 \times \left(\frac{F_{475/735}}{F_{545/735}}\right) - 81\right] \times 100\% \tag{7}$$

It was developed through a process that involved mixing Micelle_{D+A} (8% donor and 5% acceptor), micelle_D, and micelle_A in various ratios. The *in vivo* data showed that about 60% of the micelles administered intravenously remained intact during blood circulation[99]. These findings not only validate the probe design but also reinforce the importance of minimizing self-quenching for accurate tracking of nanocarriers.

In another study, FRET molecules, 3,3′-dioctadecyloxacarbocyanine perchlorate (DiO) and DiI, were encapsulated to investigate the stability of self-assembled polymeric micelles (PMs) made from poly(D,L-lactide-*co*-2-methyl-2-carboxytrimethylenecarbonate)-*g*-poly(ethylene glycol) (P(LA-*co*-TMCC)-*g*-PEG)[114]. Stability was analyzed in fetal bovine serum, globulins, and albumin using the FRET ratio $I_{565}/(I_{565}+I_{501})$, which correlates to the extent of PM decomposition[114]. The results demonstrated that FRET is a convenient tool for assessing the stability of micelles in biologically relevant environments when coupled with chromatography and light scattering technology[114].

Further, FRET dyes cyanine dye 5 (Cy5) and cyanine dye 5.5 (Cy5.5) were covalently linked to a limited number of PEG-PCL and PEG-*block*-poly(D,L-lactide) (PEG-PDLLA) polymer chains, forming FRET micelles, thereby enabling the assessment of micellar structural stability[65]. The study proposed a direct proportionality between the micelle content in the solution (micelle %) and the FRET efficiency, allowing for the deduction of micelle integrity from FRET efficiency[65]. These FRET micelles were instrumental in showing that micelle integrity is influenced not only by serum proteins and mechanical forces like shear stress, but also by polymer composition and fluorophore distribution[65].

Studies comparing self-assembled mPEG-PDLLA with disulfide (DS) bonded methoxypoly(ethylene glycol)-(cysteine)4-poly(D,L-lactic acid) (mPEG-(Cys)4-PDLLA) micelles by FRET probes (DiO and DiI) revealed that DS micelles exhibit enhanced stability in reductive intracellular environments, highlighting how responsive crosslinking strategies can improve intracellular delivery precision[128].

Similarly, the use of DS-crosslinked Pluronic polymeric micelles using the zebrafish larval model underscored the role of crosslinking in maintaining micellar integrity during systemic circulation, as indicated by FRET[129]. The FRET ratio was calculated to report the integrity of PMs *in vitro* and *in vivo*. These PMs exhibited higher FRET ratios compared to their non-crosslinked counterparts, demonstrating that covalent stabilization strategies can meaningfully enhance structural robustness and, consequently, delivery performance[129]. Moreover, their results showed that intact micelles were mainly excreted through bile after breaking down into polymers in zebrafish[129].

The integration of a newly synthesized triblock amphiphilic copolymer was used to create micelles, which were then modified with piperazine[118]. The micelles were labeled with IR-780 and

fluorescein isothiocyanate; MeTTMN, 2-((5-(4-(dip-tolylamino)phenyl)thiophen-2-yl)methylene)malononitrile; MS735, 1-(3-azidopropyl)-4-{2-[6-(diethylamino)-2-benzofuranyl]ethenyl}-3-sulfopyridinium inner salt; NBD-X, succinimidyl 6-(*N*-(7-nitrobenz-2-oxa-1,3-diazol-4-yl) amino)hexanoate; PDMS, poly-dimethylsiloxane; Rhod B, rhodamine B; TPB, tetraphenylborate.

newly synthesized IR-780-poly-dimethylsiloxane (PDMS) as a FRET pair. The intracellular fate of micelles in HeLa cells was analyzed using fluorescence imaging combined with FLIM. Such methodologies offer high-resolution insights into the intracellular processing of nanocarriers, informing the design of materials with optimal biocompatibility and degradation profiles.

In the work by Guo et al.[130], the use of FRET pairs (Cy5/Cy5.5) further revealed that polymer composition, particularly the length of hydrophobic blocks, and the method of micelle preparation significantly influence micelles' stability during circulation and tumor accumulation. These observations suggest that micelle design parameters can be fine-tuned for enhanced therapeutic targeting and retention in disease sites.

The diverse array of studies reviewed here underscores the versatility and significance of FRET in assessing the stability and intracellular destiny of micelles. This comprehensive analysis highlights the pivotal role of FRET in advancing our understanding of micelle behavior in varied biological environments and therapeutic contexts.

3.3.3. NCs

NCs represent a transformative advancement in drug delivery, particularly for oral administration, where stability through the GIT tract and efficient absorption remain key challenges. FRET technology has emerged as a crucial tool for probing the stability and distribution of NCs in biological systems. The following studies collectively deepen our understanding of how NC morphology, integrity, and cellular interactions impact therapeutic outcomes.

In one study investigating the oral delivery potential of puerarin (PU) NCs for Parkinson's disease, FRET-loaded DiO/DiI/PU-NCs were utilized to track NC integrity post-gavage in zebrafish. The effectiveness of this FRET system was then quantified by calculating the FRET ratio. The marked difference in FRET ratios, 0.85 for intact *vs.* 0.25 for disintegrated NCs, enabled real-time visualization of NC transit and accumulation in both the intestine and brain of the fish[131]. This study demonstrates the feasibility of using FRET to evaluate oral NC stability and CNS targeting, a significant step forward for treating neurodegenerative diseases *via* non-invasive routes.

Another study focused on paclitaxel (PTX) hybrid NCs, which used FRET (DiO and DiI) efficiency changes before and after acceptor photobleaching to confirm intact NC transport through Madin-Darby canine kidney cells monolayer[132]. FRET efficiency was calculated as shown in Eq. (8):

$$\mathrm{FRET}_{\mathrm{efficiency}} = \frac{\left(D_{\mathrm{post}} - D_{\mathrm{pre}}\right)}{D_{\mathrm{post}}} \tag{8}$$

where D_{post} is the fluorescence intensity of the donor after the acceptor was bleached, and D_{pre} is the fluorescence intensity of the donor before bleaching. The change in FRET efficiency is indicative of the distance between two fluorophores. The stable FRET signal post-internalization indicated that NCs were absorbed in an intact state[132]. This supports the notion that well-designed NCs can maintain structural integrity during transcellular transport, enhancing their bioavailability and therapeutic precision.

The influence of NC morphology on oral delivery efficiency was investigated using FRET (DiO and DiI)-labeled lovastatin NCs of varying shapes: spherical (SNC), rod-shaped (RNC), and flaky (FNC)[133]. RNCs exhibited superior mucus permeability and transepithelial transport, correlating with enhanced cellular uptake[133]. These findings highlight the significance of particle geometry in optimizing NC interaction with biological barriers. Extending this work, biodistribution studies demonstrated that RNCs exhibited prolonged GIT retention and preferential accumulation in the liver[115]. This morphology-driven biodistribution not only improved antihyperlipidemic efficacy but also emphasized how tailored NC shapes can modulate organ-specific delivery, offering a promising strategy for site-targeted therapeutics.

In a complementary approach, researchers combined coumarin 6 (C6) with 2-((5-(4-(dip-tolylamino)phenyl)thiophen-2-yl)methylene)malononitrile (MeTTMN) to form a FRET pair capable of simultaneously tracking drug dissolution and NC integrity[117]. Their optimized FRET system allowed distinction between intact NCs and released drug, revealing that oral absorption of C6 NCs predominantly occurs *via* the dissolved form of the drug. And the method for calculating FRET efficiency was detailed in a previous publication[134]. This underscores the importance of distinguishing between particle-mediated and solution-mediated absorption, which is critical when designing NCs for controlled release or targeting specific absorption sites.

Thus, FRET emerges as a vital tool in elucidating the mechanisms of NC drug delivery, shedding light on the interactions of NCs within biological systems. The research underscores the importance of particle design and morphology in drug efficacy, emphasizing the need for continued advancement in NC research to enhance drug delivery systems.

3.3.4. Nanoparticles

To deepen our understanding of nanoparticle behavior in biomedical applications, this section reviews a series of studies using FRET technology. These investigations reveal critical insights into the dynamics, stability, and functional efficacy of different nanoparticle formulations.

One study employed FRET to evaluate the real-time dissociation and biodistribution of self-assembled lipidic nanoparticles (SALNPs) composed of CdTe/CdSe/CdS/ZnS quantum dot cores and Cy7[71]. The observed FRET signal changes revealed rapid detachment of Cy7-lipid from the nanoparticles upon tumor accumulation, while NIR fluorescence imaging demonstrated distinct spatial distribution patterns between the quantum dot core and Cy7-lipid component in organs such as the liver and spleen[71]. This study highlighted the *in vivo* instability of SALNPs and emphasized the importance of designing nanocarriers that preserve structural integrity at the target site to improve therapeutic delivery.

Another study used FRET to investigate the intracellular hydrolysis process of ketal-crosslinked nanoparticles under varying pH environments[116]. By separately labeling batches of block copolymers with cyanine dye 3 (Cy3) and Cy5, researchers monitored the degradation of nanoparticles in acidic environments[116]. The FRET ratio was calculated by dividing the fluorescence intensity of the acceptor Cy5 at 667 nm by the emission intensity of the donor Cy3 at 568 nm and plotted with time to visualize the gradual decrease in ketal-crosslinked particles in different pH environments. The pH-responsive degradation, confirmed through both FRET and dynamic light scattering (DLS) measurements, provided evidence for selective disassembly under pathological conditions[116]. These results reinforce the value of pH-sensitive

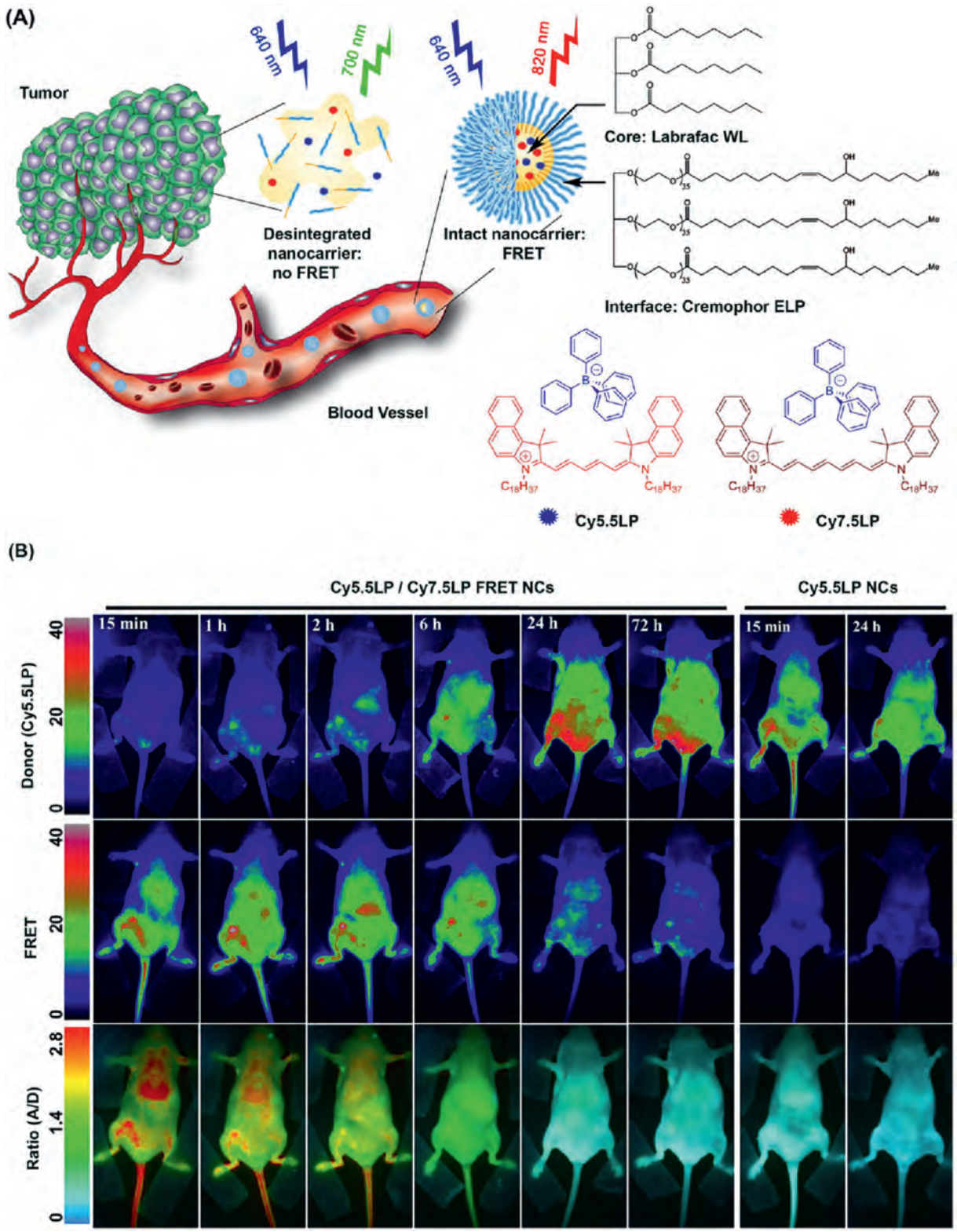

Figure 5 FRET nanocarriers for emission color-based integrity reporting. (A) Design concept: schematic of FRET-based nanocarriers that signal structural integrity *via* emission color change. Key components: medium-chain triglyceride oil Labrafac WL (core), PEGylated surfactant Cremophor ELP (interface), and lipophilic cyanine dyes Cy5.5LP and Cy7.5LP (including bulky hydrophobic counterions). These dyes enable FRET for real-time monitoring of nanocarrier integrity in biological environments. (B) *In vivo* disintegration tracking: NIR fluorescence imaging of healthy nude mice after injection of NIR-FRET lipid NCs (1% Cy5.5LP + 1% Cy7.5LP) *versus* control NCs (1% Cy5.5LP only). Panels show (top) Cy5.5LP channel (700 nm), (middle) Cy7.5LP channel (820 nm), and (bottom) ratiometric (acceptor/donor) images ($\lambda_{ex} = 630$ nm). Time-lapse imaging reveals: 1) increasing Cy5.5LP intensity (peaking at 24 h) and declining FRET signals in FRET NCs, indicating disintegration; 2)

crosslinkers in developing smart delivery vehicles that disassemble at disease sites for controlled drug release.

In the context of prodrug-based systems, FRET was instrumental in monitoring the stability of squalene-linked gemcitabine (SQGem) nanoparticles after systemic administration[41]. Using Cy5.5 and cyanine dye 7.5 (Cy7.5) attached to squalene, researchers quantified nanoparticle integrity *via* a calibration curve derived from the FRET PR. The rapid decline in FRET signal within 2 h post-injection revealed the transient nature of SQGem stability in circulation[41]. This underscores the challenge of ensuring nanoparticle stability while achieving timely prodrug activation, which is crucial for effective therapeutic outcomes.

Expanding the scope to drug release kinetics, a novel J-aggregate-based FRET[135] approach was used to compare polymeric nanoparticles with high (50%, *w*/*w*; $W_{dye}/W_{dye\ +\ polymer}$) and low (0.5%, *w*/*w*; $W_{dye}/W_{dye\ +\ polymer}$) drug-loading capacities. The appearance of a distinct red-shifted FRET peak in high-loading formulations, coupled with DMSO dissolution studies, uncovered a two-step release process in both cellular and serum environments, involving dye aggregates dissolved within the polymer shell, followed by the breakdown of the shell, releasing dye molecules[135]. This dual-phase release mechanism explains the slower drug release observed in high-loaded nanoparticles and provides insight into how drug loading modulates release profiles, an important consideration for dose optimization and sustained delivery[135].

In another key advancement, FRET analysis was applied to pH-responsive nanoparticles designed for protein delivery across cellular barriers[113]. Using fluorescein isothiocyanate (FITC) and rhodamine B (Rhod B) as the FRET pair, researchers tracked the conformational shifts and dissociation of pH-responsive CS-N-Arg/γ-PGA-Tau nanoparticles in response to pH changes, revealing efficient protein transport under intestinal conditions[113]. This study demonstrates the utility of FRET in visualizing macromolecule transport mechanisms and supports the development of pH-sensitive carriers tailored for oral protein delivery.

Collectively, these studies enhance our understanding of nanoparticles, from their structural integrity in biological systems to their potential in targeted drug delivery. The diverse applications of FRET technology in these investigations offer invaluable insights, paving the way for future advancements in nanoparticle-based therapies and diagnostics.

3.3.5. Nanoemulsions

The field of nanoemulsions is increasingly recognized for its potential in drug delivery and cancer targeting. Their biocompatibility, biodegradability, and ability to encapsulate various therapeutic agents make them a key area of study. However, understanding their *in vivo* integrity remains a major challenge for their biomedical application.

One of the significant contributions to this field was conducted by Bouchaala and co-workers[100], who conducted and published the first report on the direct quantitative analysis of intact nanocarriers in living mice by FRET. They have explored the use of fluorescent nanoemulsion droplets, around 100 nm in size, which encapsulate lipophilic Cy5.5 (Cy5.5LP) and Cy7.5 (Cy7.5LP). These probes are stabilized with a bulky hydrophobic counterion, TPB, to enhance brightness and enable efficient FRET within the lipid nanocarriers (Fig. 5A). This approach has allowed for quantitative fluorescence ratiometric imaging to monitor nanocarrier integrity directly in the blood circulation, liver, and tumor xenografts of living mice. Remarkably, these studies revealed that the integrity of FRET-enabled nanocarriers in the bloodstream of healthy mice remained at 93% up to 6 h post-administration (Fig. 5B), decreasing to 66% in the liver with a half-life of 8.2 h. Furthermore, these nanocarriers showed efficient tumor accumulation, maintaining 77% integrity at 2 h before reducing to 40% at 6 h. This methodology offers a robust way to evaluate nanocarrier integrity *in vivo*, demonstrating that nanoemulsion droplets are stable nano-objects, mainly releasing their contents after entering tumor sites. In summary, this research underscores the importance of understanding nanocarrier integrity for effective drug delivery. The use of FRET in nanoemulsions offers a powerful tool for assessing their stability and functional efficacy in real biological systems, thereby contributing significantly to the advancement of nanomedicine.

3.3.6. Others

This section expands the exploration of FRET applications by focusing on a diverse array of other nanocarrier systems, each revealing specific aspects of carrier behavior in biological environments.

The first study on C6-loaded nanostructured lipid carriers (NLCs) of varying sizes (100, 200, 300 nm) utilized the FRET pair DiO/DiI to evaluate how particle size affects nanocarrier integrity across different biological media[136]. The change in the FRET ratio represents the change in NLC integrity, which is calculated as in equation (9):

$$\mathrm{FR}\ (\%) = \frac{F_i}{(F_0 + F_i)} \times 100\% \tag{9}$$

where F_i and F_0 are the fluorescence intensities at 564 and 504 nm, respectively. While all formulations remained stable in simulated buffer solutions, only the 100 nm NLCs displayed the most stable FRET signal in blood, suggesting that smaller particles may better resist physiological shear stress and protein interactions[136]. These findings support prioritizing size-optimized NLCs for oral drug delivery, where systemic stability is essential.

Moving into stimulus-responsive systems, the development of self-sensing porphysomes provided a powerful example of using FRET signal shifts to monitor nanocarrier structural changes for photothermal therapy (PTT). This system used bacteriopheophorbide a-lipid and pyropheophorbide-lipid as a FRET pair to enable real-time structural assessment. When intact, the nanocarrier exhibits a specific fluorescence ratio ($F_{790\ nm}/F_{720\ nm} = 4$), which shifts towards 0.25 upon destruction[137]. In the experimental part involving KB tumor xenograft model mice, the dynamic FRET ratio changes were tracked for 48 h post-intravenous injection, revealing the accumulation of intact nanocarriers in the tumor[137]. This illustrates the potential of embedding diagnostic functionality within therapeutic carriers, which is a strategy central to the development of theranostic nanomedicines.

In ocular drug delivery, dual-carrier systems, such as the dexamethasone-loaded hydroxypropyl-β-cyclodextrin complex@liposome nanocomposites, demonstrated how FRET (Cy5.5 and Cy7) can simulate different states of carrier integrity through

approximately 30-fold decrease in acceptor/donor ratio, visualized as a ratiometric color shift (red→blue); 3) control NCs showed no FRET activity, enabling vascular imaging shortly post-injection (though with reduced detail *versus* FRET NCs). Results from three independent mice confirm diagnostic potential for real-time *in vivo* tracking. Reprinted with the permission from Ref. 100.

ratiometric analysis[58]. By mixing different proportions of FRET carriers, the study simulates various levels of carrier integrity, creating a calibration curve for FRET efficiency[58]. The results indicated that the intact cyclodextrin complexes can pass through the human conjunctival epithelial cell well, and the dual-carrier system showed enhanced effectiveness in delivering drugs to the eye's posterior segment in rabbit models[58]. This paves the way for more effective treatments of posterior eye diseases that currently lack efficient drug delivery systems.

Further reinforcing this concept, Zhu et al.[79] developed a novel FRET quantification method linking FRET fluorescence signal intensity to Cy7 content to overcome the limitations of static ratio-based analyses, enabling dynamic assessment of liposomes and cyclodextrin@liposome nanocomposites integrity in ocular drug delivery. Their findings revealed that PEGylation and glycine sarcosine modification enhanced conjunctival-scleral penetration while preserving liposome integrity. FRET further demonstrated dual-carrier nanocomposites' unique advantages: outer liposomes shielded inner cyclodextrin complexes, enabling sustained choroid-retina drug delivery. By bridging real-time structural monitoring with therapeutic outcomes, FRET emerged as an indispensable tool for rational ocular drug nanocarrier design.

Su and colleagues[98] employed FRET (C6 and Rhodamine 123) to distinguish between the transcytosis and degradation phases of a hypoxia-inducible factor-1 inhibitor (BAY 87-2243)-loaded liposomal system with hyaluronic acid (HA) crosslinking and low molecular weight protamine modification. FRET analysis revealed sustained energy transfer signals during endothelial transcytosis, confirming structural integrity preservation. Conversely, HAase-triggered degradation in tumor cells disrupted the energy transfer process, correlating with the cargo release. This dual-phase monitoring approach enables a precise evaluation of tumor-specific degradation mechanisms, informing the rational design of environment-responsive carriers.

In an intracellular context, FRET imaging (DiI and DiD) was leveraged to investigate the intracellular fate of calcium alginate-based nanocarriers in keratinocytes[138]. A marked change in fluorescence ratios indicated whether the carriers remained intact or had disintegrated. The results demonstrated that while only a minor portion of the intact nanocarriers could penetrate the cell, they rapidly disassembled upon internalization to release their contents[138]. This illustrates FRET's utility at the cellular level and informs future efforts to engineer nanocarriers for efficient intracellular drug release.

Lastly, studies evaluating the brain targeting capability of liposomes and lipid disks modified with ligands employed multi-dye FRET labeling (DiO, DiI, and DiD) to track the interaction with the blood-brain barrier (BBB) and blood−brain tumor barrier (BBTB)[139]. The characteristic emission of DiD after DiO excitation serves as an indicator of the integrity of nanocarriers. Fluorescence detection in *in vitro* models of BBB and BBTB, as well as in mouse brains, demonstrated the ability of these nanocarriers to penetrate these barriers while maintaining their integrity[139]. These results guide the engineering of lipid-based platforms for effective CNS drug delivery.

Each of these studies presents a unique application of FRET in nanocarrier research. From assessing the stability of nanoemulsions in living mice to exploring the integrity of lipid disks across the BBB, the range of applications illustrates the breadth of possibilities in nanocarrier research. An ideal nanocarrier should possess high structural integrity after crossing the existing tissue barriers so as to improve the efficiency of the drug delivery system. Conclusively, this section underscores the adaptability and effectiveness of FRET in advancing our understanding of nanocarriers.

4. AIE

4.1. Rationale of AIE and AIE-based nanocarrier imaging

Conventional NIR fluorophores often suffer from ACQ, exhibiting weak or no emission at high concentrations or in aggregated states[140]. This quenching arises primarily from $\pi-\pi$ stacking and other nonradiative pathways. As these molecules have highly hydrophobic emitting centers, they are prone to aggregation in biological media, compromising imaging clarity and efficacy[141]. In 2001, Tang and colleagues introduced the concept of AIE[142], which fundamentally contrasts with ACQ. Unlike ACQ fluorophores, AIEgens exhibit minimal to no emission in their dissolved state; however, in their aggregated state, AIEgens emit strong fluorescence. This abnormal fluorescence emission of AIEgens in their solid state is due to the nonplanar structure of AIEgens, which helps prevent $\pi-\pi$ stacking interactions between molecules, thereby enhancing the fluorescence performance of these molecules[143]. To be specific, bulky and twisted structures are a common feature of dyes that display AIE[144].

Beyond fluorescence imaging, many AIEgens also function as photosensitizers (PSs) with photodynamic or photothermal properties. A crucial feature contributing to these properties is their low energy gap between the lowest singlet state (S_1) and the lowest triplet state (T_1), known as ΔEst. This feature promotes the intersystem crossing (ISC) process, which, especially in their aggregated state, is likely to efficiently generate singlet oxygen ($^1O_2$) upon exposure to light (Fig. 6A) and can be used for image-guided photodynamic therapy (PDT). Additionally, because photothermal materials often possess the ability of photoacoustic imaging (PAI)[145], AIEgens with twisted intramolecular charge transfer (TICT) phenomena can be used in PAI-guided PTT[146,147]. While AIE molecules have also been designed to effectively combine NIR-II FLIM, PAI, and photothermal imaging (PTI) for trimodal imaging, alongside synergistic PDT and PTT[148], the primary focus of this review is on the precise tracing of nanocarriers, acknowledging these broader diagnostic and therapeutic applications.

Understanding the AIE mechanism is critical for the rational design of next-generation AIEgens (Fig. 6B). The prevailing explanation, restriction of intramolecular motion (RIM), encompassing both rotation and vibration, has been recognized as the general working mechanism of AIE (Fig. 6B). For example, Tetraphenylethene (TPE), a classic AIEgen, dissipates excited-state energy nonradiatively through phenyl ring rotations in solution. Upon aggregation, these motions are restricted, resulting in fluorescence *via* radiative decay, a process known as restricted intramolecular rotation (RIR) (Fig. 6B). For AIEgens lacking freely rotatable rotors, such as 10,10′,11,11′-tetrahydro-5,5′-bidibenzo[*a*,*d*] annulenylidene and 5,5′-bidibenzo[*a*,*d*] annulenylidene, restriction of intramolecular vibration (RIV) accounts for the fluorescence enhancement with the help of quantum mechanics and molecular mechanics calculations (Fig. 6B)[149]. According to the RIM mechanism, it can be inferred that not only aggregation but also structural rigidification in high-viscosity media, low-temperature environments, and embedding of chromophores in rigid matrices can lead to significant emission[150]. Hence, the term

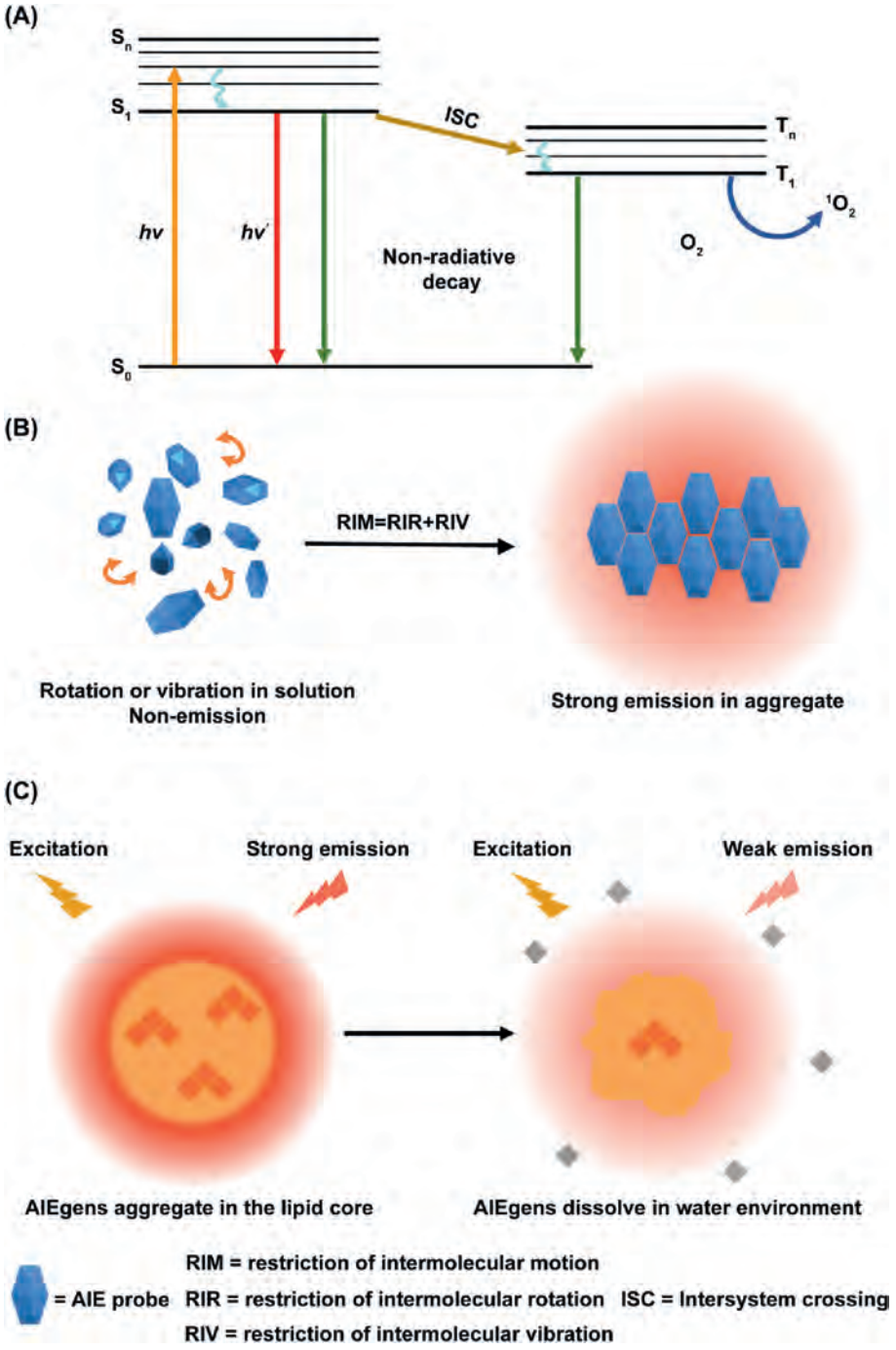

Figure 6 AIEgens for photodynamic therapy and nanocarrier labeling. (A) Photophysics of AIEgens for PDT: Jablonski diagram illustrating the photophysical behavior of AIEgens. Aggregation reduces the S_1-T_1 energy gap (ΔE_{ST}), enhancing intersystem crossing (ISC) and enabling efficient $^1O_2$ generation upon light irradiation. This facilitates their use as precise, image-guided PDT agents. (B) AIE mechanism: schematic contrasting molecular motion in solution (causing non-radiative decay and emission quenching) with restricted intramolecular motion (RIM) in the aggregated state (resulting in strong fluorescence). (C) AIEgen-labeled nanocarrier integrity sensing: partial degradation releases AIEgens into the aqueous environment, where dissolution quenches their fluorescence. Intact nanocarriers retain aggregated AIEgens, maintaining strong emission.

"AIE" does not imply that aggregation is the only pathway to emission.

Both experimental data and theoretical simulations, including quantum chemical calculations, support the RIM mechanism. These studies show that the nonradiative decay rate (k_{nr}) of an AIEgen drastically decreases, by up to four orders of magnitude, in an aggregated state. Meanwhile, the radiative decay rate (k_r) remains relatively unchanged, regardless of whether the AIEgen is

in a molecular or aggregated state[151,152]. While RIM is the predominant mechanism, several other explanations have been proposed for the notable k_n of the AIEgens in solution, including E/Z isomerization, photocyclization, rotation of phenyl rings, rotation of double bonds, easy access of conical intersection, and so on[153-156]. Additionally, phenomena such as the formation of J-aggregates, conformational planarization, and excited-state intramolecular proton transfer can also partially explain the AIE phenomenon[157,158].

While many AIE mechanisms are well established, emerging systems still require further investigation. For example, some electron-rich nonconjugated polymers with AIE properties exhibit clustering-triggered emission or intramolecular through-space conjugation, offering new mechanistic insights[159,160]. Certain AIEgens also display crystallization-induced emission[161,162], where strong emission only occurs in crystalline states due to tighter intermolecular interactions[163,164]. Furthermore, some novel AIE systems demonstrate exceptionally high excited-state emission levels[165], the origins of which still await further theoretical and experimental elucidation.

Building on the understanding of AIE mechanisms, particularly RIM, these principles have been exploited to design advanced nanocarrier imaging systems. In the context of nanocarrier imaging, AIEgens are valuable due to their environment-responsive fluorescence. When encapsulated within nanoparticles, they emit fluorescence upon aggregation (Fig. 6C), and this emission is closely linked to nanocarrier integrity[143]. AIEgens can be incorporated into various nanocarriers either through covalent or noncovalent bonds[166,167]. Key design considerations for AIEgen-based nanocarriers include ensuring a uniform distribution of AIEgens within the nanocarriers and maintaining a low background signal. In this context, a polymer matrix is often employed as a protective layer, minimizing the exposure of the AIEgen core to aqueous media and encapsulating the molecule to form nanoparticles.

Water-soluble AIEgens are particularly advantageous for biological research, as they emit within lipophilic nanocarrier interiors and are quenched upon release into aqueous environments[168]. This reaction leverages the environment-responsive nature of AIEgens, providing a method to monitor the fate of intact nanocarriers[46]. In contrast, hydrophobic AIEgens may retain some fluorescence post-release by forming aggregates[169]. Nevertheless, several studies have utilized hydrophobic AIEgens to track nanocarriers[170,171]. The rationale is that AIEgens released into the ambient environment may be diluted, and the probe concentration is too low to cause aggregation-induced fluorescence, so the leaked probes may not cause much substantial interference.

Beyond acting as external labels, some AIEgens can be directly integrated into nanocarrier backbones, eliminating the need for additional encapsulation or conjugation steps[172]. These self-indicating nanocarriers emit fluorescence only when intramolecular motion is restricted by the nanostructure[173].

Furthermore, FRET interactions between AIEgens and therapeutic agents, such as doxorubicin (DOX) and TPE[174,175], enable simultaneous monitoring of drug release and nanocarrier behavior. However, the complexity of such systems demands careful analysis to accurately interpret fluorescence origins and dynamics. Altogether, these diverse strategies demonstrate the versatility of AIEgens in designing multifunctional, responsive nanocarrier systems that combine imaging precision with therapeutic functionality.

4.2. Structural engineering of AIEgens for NIR imaging

Optimizing the photophysical properties of AIEgens is essential to expanding their utility in biomedical imaging. One major limitation of commonly used AIEgens is that their excitation and emission wavelengths mostly fall within the visible spectrum. This restricts tissue penetration and results in interference from tissue autofluorescence, thereby confining most applications to intracellular observations. Since cells are the ultimate destinations for nanocarriers, understanding intracellular behaviors such as drug release dynamics, cellular uptake, intracellular distribution, metabolism, and efflux is critical[176]. Nevertheless, *in vivo* imaging is ultimately more desirable for elucidating the complete biological fate of nanocarriers.

To overcome this limited optical window, extensive efforts have focused on engineering AIEgens that absorb and emit in the NIR region. A widely adopted strategy involves tuning the molecular structure based on the intramolecular charge transfer (ICT) principle. This typically includes reshaping the molecular structure to make it more planar, enhancing the level of conjugation, or doping the compound with other atoms. Collectively, these changes aim to endow the compound with a structure that facilitates electron push-pull dynamics, effectively red-shifting the emission wavelength[177].

For instance, Wang and co-workers[178] combined a strong electron donor−acceptor interaction with extended $\pi-\pi$ conjugation to facilitate the ICT of AIEgen TTVP; additionally, the twisted conformation of its triphenylamine fragment further increases the intermolecular distance, suppressing $\pi-\pi$ interactions-induced quenching between molecules, which results in longer absorption and emission wavelengths.

Similarly, incorporating certain molecular structures can aid in developing AIEgens that emit at longer wavelengths. TPE, known for its propensity to form helical structures and strong electron-donating capabilities, can serve as such a functional fragment. The fluorescence properties of these molecules can be modulated by attaching them to electron-withdrawing groups and controlling the intramolecular push-pull electron interactions[179-181]. TCAQ is famous for its special aromatic structure and strong electron-withdrawing effect[182]. In the AIE photosensitizer TPETCAQ, TCAQ modification leads to a pronounced ICT from the two methoxy groups to TCAQ. This strong electron-withdrawing capability of TCAQ imparts TPETCAQ with the ability to emit in the NIR spectrum[183].

Moreover, structure-activity relationships reveal that site-specific modifications can exert differential effects on the photophysical properties of AIEgens. Importantly, many AIEgens summarized in Table 2[44,46,73,173,178,183-190] are derivatives of archetypal fluorophores like TPE[191,192], underscoring the importance of rational molecular design in tailoring functional imaging agents.

In terms of wavelength-dependent trade-offs, visible-range probes exhibit high quantum yields (QYs, >20%) and biocompatibility, yet are restricted to superficial imaging due to strong scattering and autofluorescence (<1 nm depth)[193]. NIR-I probes extend imaging depth to moderate penetration (5−10 mm) with reduced scattering and acceptable QYs (4%−8%), but often suffer from lower signal-to-background ratios (SBR ∼ 3−5) and limited resolution in dense tissues[194]. In contrast, NIR-II AIEgens offer deep tissue (*e.g.*, cerebral vasculature, tumors) penetration (>3 cm, up to 11 cm for NIR-IIb) and exceptional spatial resolution due to minimal autofluorescence and photon

Table 2 Typical AIE probes utilized in bioimaging investigations.

Name	Chemical structure	$\lambda_{ex}/\lambda_{em}$ (nm/nm)	Ref.
TPE		350/450	44
THPE		350/450	46
DPA-SCP	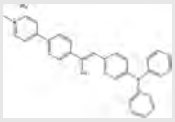	460/620	73
TPECM	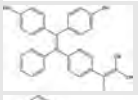	410/615	173
TTVP	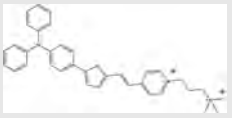	480/708	178
TPETCAQ	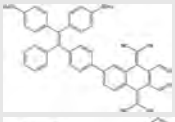	Broad absorption from 300 to 700, with two peaks centered at 360 and 520/820	183
QM-2	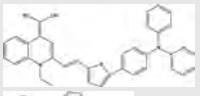	488/657	184
TPS-NCS		405/505−525	185
TPETP	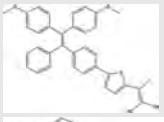	440/650	186
TPE-TPA-DCM	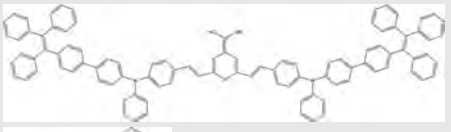	502/660	187
NPAPF	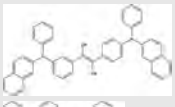	500/640	188
Compound 4	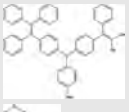	460/645	189
PBPTV		700/960	190

DPA-SCP, diphenylamino-salt α-cyanostilbene pyridinium; PBPTV, pyridal[2,1,3]thiadiazole-based semiconducting polymer; QM-2, quinoline-malononitrile-2; THPE, tetrakis(4-hydroxyphenyl) ethylene; TPE, tetraphenylethene; TPE-TPA-DCM, 2-(2,6-bis((*E*)-4-(phenyl(4′-(1,2,2-triphenylvinyl)-[1,1-biphenyl]-4-yl)amino)styryl)-4*H*-pyran-4-ylidene)malononitrile; TPS-NCS, isothiocyanate-functionalized tetraphenylsilole.

scattering[195]. Although they exhibit lower QYs (0.1%−11.5%) due to non-radiative decay dominance, their high SBR (>30) and depth performance justify this trade-off. Notably, NIR-II AIEgen like BPBBT@human serum albumin combine high brightness and photothermal efficiency for image-guided therapy in deep tissues[196]. Thus, visible/NIR-I probes excel in high-sensitivity superficial diagnostics, while NIR-II AIEgens are indispensable for precision theranostics and deep-tissue nanocarrier tracking[194].

4.3. AI-driven design of AIEgens

Beyond empirically optimizing traditional AIE molecules, artificial intelligence (AI), including machine learning (ML), computational modeling, etc., accelerates the discovery and optimization of new AIEgens with tailored functionalities[197]. For instance, ML models trained on molecular descriptors from 1245 reported AIEgens successfully predicted three new structures AIEgens with customized spectral properties; these were synthesized and validated for

cellular and biomedical deep fluorescence imaging[198]. Similarly, automated combinatorial workflows driven by AI predictions have streamlined the synthesis of AIEgens for stabilizing hydrophobic nanoparticles[199]. Crucially, AI synergizes with AIEgens to enable advanced applications. Hua et al.[200] developed AIEgen-Deep, an integrated platform combining AIEgens, deep learning, and the Segment Anything Model, achieving high-accuracy discrimination between healthy and malignant cells for early cancer detection.

Returning to AI-driven design of AIEgens, AI has shown promise in predicting the interaction between molecules and biological targets such as proteins[201] and cells[202], potentially guiding the design of receptor-specific AIEgens for targeted delivery. Concurrently, AI's capacity to decode complex datasets could possibly facilitate multiplexed sensing by engineering AIEgens that simultaneously detect multiple analytes (*e.g.*, ions, disease biomarkers), enhancing diagnostic efficiency[203].

Despite these advances, significant challenges persist: (1) data scarcity-limited experimental data on AIE-biological interaction constrains prediction accuracy[204]; (2) translational gaps-AI-designed molecules may exhibit unforeseen *in vivo* toxicity or instability, requiring extensive validation[205]; (3) interdisciplinary barriers-effective implementation requires close collaboration among computational scientists, chemists, and biologists. Addressing these limitations is essential to fully harness AI-AIEgen synergy for precision biomedicine, while there is no doubt that the future of AI-driven AIEgen design is bright.

4.4. Challenges in AIEgen-based nanocarrier imaging

Despite the structural and spectral advances discussed, several challenges persist in the application of AIEgens for precise nanocarrier tracking. A fundamental limitation is the absence of internal calibration standards for absolute nanocarrier concentration quantification *in vivo*, compounded by poorly defined correlations between AIEgen fluorescence intensity and intact nanocarrier concentration. This quantification uncertainty is exacerbated by unpredictable biological interference, particularly protein adsorption-induced fluorescence enhancement that generates false-positive signals. To overcome these barriers, experimental approaches that simulate the physiological degradation of nanocarriers and systematically correlate fluorescence changes with particle integrity should be prioritized. Furthermore, computational methods, particularly AI-assisted molecular design, offer promising avenues for developing next-generation AIEgens with minimized nonspecific interactions and improved signal fidelity. These optimized probes would allow for more accurate interpretation of fluorescence signals about nanocarrier degradation, ultimately advancing the precision of *in vivo* tracking applications.

False positives also arise from AIEgens' intrinsic hydrophobicity, which may lead to reaggregation and fluorescence emission after release from nanocarriers. One solution involves the development of water-soluble NIR AIEgens through integrating high donor-acceptor strength with hydrophilic units into a propeller-shaped molecular structure[178]. However, even with improved solubility, AIEgens might still non-covalently bind to biomacromolecules, which can restrict intramolecular motion, reactivating fluorescence even in the absence of intact carriers. Consequently, additional strategies are required to eliminate such false-positive signals from released AIE agents.

Moreover, preventing off-target aggregation or fluorophore leaching to ensure *in vivo* stability and accuracy of AIEgen-labeled nanocarriers requires deliberate engineering. Key strategies include: firstly, covalently conjugating AIE probes to nanocarriers[206] or using tight encapsulation[207] to prevent leaching and enable quantifiable, high-fidelity tracking of nanocarrier biodistribution. Secondly, surface engineering with targeting ligands minimizes off-target effects[208]. Incorporating stimuli-responsive linkers in the AIE nanocarrier's design is also beneficial for controlled release[209]. Thirdly, enhancing structural rigidity *via* crosslinking AIE nanoparticles or optimizing particle size can effectively help particles resist dissociation in biological fluids[210].

Feasibility verification methods include calculation of SNR, tumor-to-background ratio (TBR), fluorescence retention, and co-localization coefficients. Additionally, *in vivo* and *ex vivo* (organs) biodistribution studies provided direct evidence of minimized off-target aggregation and probe leaching. These quantitative parameters are discussed further in the application section.

Another underexplored but critical issue is the biocompatibility, clearance, and immunogenicity of AIEgens[143]. This is particularly important for AIE molecules capable of generating reactive oxygen species (ROS), which may interfere with biological processes or compromise nanocarrier functionality. Table 2 serves as a comprehensive summary of AIEgens as referenced in various literature sources, aiming to offer a useful reference for researchers selecting probes suited to their specific research objectives.

Like any other probe-labeled nanocarriers, the *in vivo* stability and biodegradation of AIE-labeled nanocarriers are critical factors affecting imaging performance. The physicochemical properties of the carrier materials, such as polymer composition, surface chemistry, and degradation rate, govern the nanocarrier's structural integrity and its ability to retain the AIEgens over time. Similarly, the encapsulation strategy (*e.g.*, physical encapsulation *vs.* covalent conjugation) plays a pivotal role in preventing premature leakage or degradation of the AIEgen. Furthermore, biological factors such as pH variations, enzymatic activity, and the formation of protein corona can alter the carrier's behavior, potentially leading to signal loss or misinterpretation in imaging. Critically, gradual degradation might cause a mismatch between the fluorescence signal and actual nanocarrier presence, complicating biodistribution analysis. To address these issues, recent studies have focused on engineering AIEgens with enhanced photostability and designing stimuli-responsive carriers that synchronize degradation with signal deactivation; specific examples are described in the application part.

Collectively, resolving quantification challenges while strategically leveraging wavelength-dependent advantages will accelerate the translational impact of AIE technology in nanomedicine. All these studies underscore the broad applicability and transformative potential of AIE technology in nanomedicine. By addressing distinct biomedical challenges, from gene therapy to stem cell tracking and drug delivery, AIEgens demonstrate their crucial role in advancing medical research and therapy, offering innovative solutions that could redefine future approaches in healthcare.

4.5. Application of AIE in nanocarrier bioimaging

4.5.1. EVs

For the effective application of EVs as diagnostic or therapeutic tools, it is essential to have noninvasive, continuous, and precise methods for tracking their fate within the body. This level of monitoring is crucial to understand and optimize their performance and safety *in vivo*. In a study, Cao and co-workers[211]

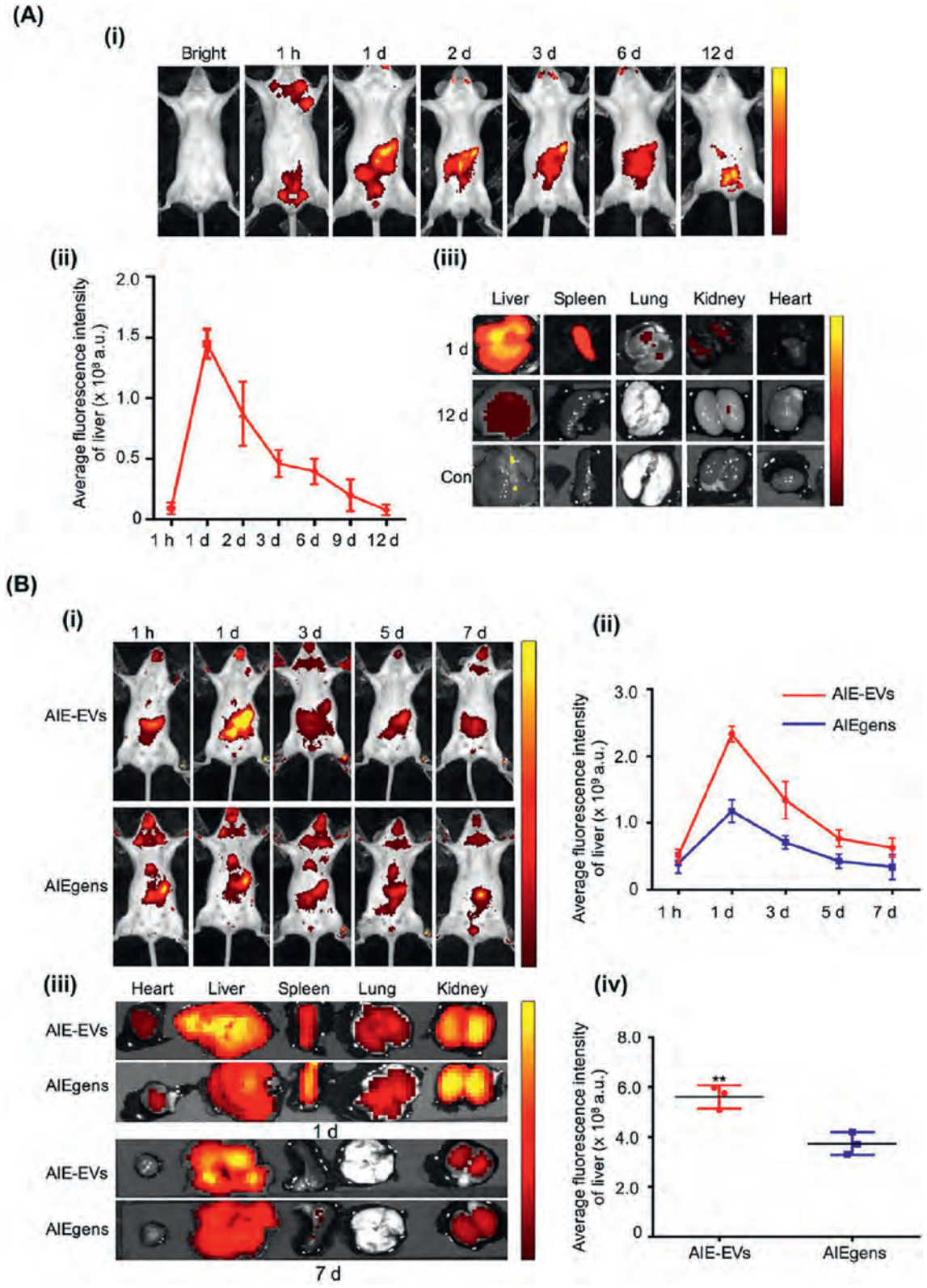

Figure 7 Comparative biodistribution analysis of AIE-EVs in healthy and ALI mice models. (A) *In vivo* and *ex vivo* tracking of AIE-EVs in healthy mice (i) shows predominant liver accumulation with peak fluorescence at 1-day post-injection, persisting up to 6 days, and decreasing by Day 12, indicating organ-specific clearance patterns (ii). The highest uptake is confirmed in the liver, followed by spleen, lungs, kidneys, and heart (iii). (B) In ALI mice, AIE-EVs demonstrate enhanced liver affinity with more intense fluorescence signals compared to AIEgens (i), with quantitative analysis revealing a 2.5-fold increase in liver fluorescence for AIE-EVs on Day 1, and a 1.5-fold increase on Day 7 (ii, iv). *Ex vivo* imaging aligns with *in vivo* results, confirming the highest signals in the AIE-EV group (iii). These data underscore AIE-EVs' potential for targeted liver therapeutics. Reprinted with the permission from Ref. 211. Copyright © 2020 ACS.

achieved reliable EV labeling by attaching the positively charged diphenylamino-salt α-cyanostilbene pyridinium (DPA-SCP) to the negatively charged EV membrane. The results show that DPA-SCP has better photostability and higher labeling efficiency than the commercial EV tracker PKH26 and DiI. At the *in vitro* level, AIEgens could track EVs, and the intensity of the fluorescence signals was dependent on the concentration of the AIEgens[211]. Moreover, the team used DPA-SCP to track EVs in healthy mice and acute liver injury (ALI) models (Fig. 7)[211], revealing AIE-EV accumulation predominantly in the liver (peaking on Day 1, persisting 6 days) with significantly decreased levels by Day 12, while the kidneys maintained these signals, indicating renal clearance (Fig. 7A (i, ii)). *Ex vivo* analysis, as illustrated in Fig. 7A (iii), is consistent with *in vivo* imaging results. In ALI mice, AIE-EVs also showed a pronounced affinity for the liver (Fig. 7B (i))[211], since AIE-EVs exhibited 2.5-fold stronger liver fluorescence than free AIEgens, confirming targeted hepatic affinity (Fig. 7B (ii)), and *ex vivo* imaging corroborated these results (Fig. 7B (iii−iv)). This work demonstrates EVs' (derived from mesenchymal stem cells) intrinsic liver-targeting capability, suggesting utility for hepatoprotective therapies with minimized off-target effects. The clearance kinetics further informed dosing schedules for chronic liver therapies[211]. Similarly, in ischemia-reperfusion acute kidney injury mice, DPA-SCP-tracked MSC-EVs accumulated specifically in damaged kidneys over 72 h[73], revealing innate tropism for injured tissues. Collectively, these studies highlight AIE technology's role in decoding organ-specific EV biodistribution, enabling high-sensitivity tracking to advance next-generation EV-based delivery systems.

4.5.2. NCs

The propeller-shaped TPE is a prototypical AIE molecule valued for its photostability and high photoluminescent efficiency. Gao et al.[212] formulated hybrid PTX NCs integrated with TPE, monitoring fluorescence changes to track intracellular NC dissolution dynamics and cellular uptake kinetics.

While TPE enabled real-time dissolution monitoring to visualize nanocarrier disintegration in live cells, its low solubility and recrystallization limit practical utility, which underscores the need for molecular engineering to improve tracking capability. The derivative, tetrakis(4-hydroxyphenyl) ethylene (THPE), with 80 times greater water solubility, overcame these limitations[46]. Confocal microscopy and flow cytometry of THPE NCs in KB cells exploited THPE's AIE property for tracking, while integration with high-performance liquid chromatography (HPLC) enabled PK modeling of cellular uptake[46]. Overall, THPE's enhanced solubility permits reliable quantification of NC behavior in biological environments[46]. These studies demonstrate how AIEgen evolution (TPE→THPE) resolves solubility constraints while enabling unprecedented correlation between fluorescence tracking and pharmacological modeling. This synergy provides a template for rationally engineering nanocarriers with optimized dissolution-uptake properties for precision drug delivery.

4.5.3. Micelles

Micelles combined with AIE technology represent a frontier in nanocarriers, enabling advanced tumor targeting, drug release control, and real-time fate tracking. In a research study, Li and colleagues[184] encapsulated micro-sized AIEgen, quinolinemalononitrile-2 (QM-2) molecules through adjusting the shape and size, within spherical nano-sized micelles made from the amphiphilic block copolymer polystyrene-*b*-poly(acrylic acid), which enhanced tumor-targeted imaging capabilities. This demonstrates that the optimization of the AIEgen structure can directly enhance its usability. Such insights could guide the design of morphology-optimized AIEgens for hard-to-reach tumors.

On the other hand, most AIEgens are typically utilized as the hydrophobic component in the formation of amphiphilic PMs, rather than just being encapsulated within micelles for labeling purposes. In the process of micelle formation by amphiphilic polymers, AIEgens are usually located at the core of the micelles, where they aggregate and emit fluorescence. When the micelle structure disintegrates, the fluorescence energy is transformed into non-radiative energy and dissipated. Yuan et al.[186] designed a novel formulation by conjugating PEG with the AIEgen PS TPETP *via* a ROS-cleavable thioketal (TK) linker, resulting in TPETP-TK-PEG. This compound was used to form PMs encapsulating the drug DOX, referred to as AIE-NPs/DOX. Fluorescence confirmed micelle accumulation and retention in drug-resistant cells, while these micelles could control the intracellular release of DOX in a photo-responsive manner. The ROS-triggered fluorescence-drug decoupling provides a real-time "map" of carrier *vs.* drug location. This strategy could overcome cancer resistance by ensuring precise intracellular drug activation while minimizing off-target toxicity.

Further exploration of micelles leads us to amphiphilic copolymers like TPE-conjugated poly(aspartic acid)-*block*-poly(2-methacryloyloxyethylphosphorylcholine). These micelles, designed with DS bonds for redox responsiveness, efficiently encapsulate drugs such as DOX and provide insights into their release dynamics[170]. These micelles disintegrate in glutathione-rich environments, with fading fluorescence signaling micelle breakdown and drug release. This fluorescence decay and drug release correlation offers a noninvasive tool to monitor carrier stability. Such systems could be adapted to target tumor microenvironments or inflammatory sites with inherent redox imbalances. TPE can also be grafted to hydrophilic dextran through acid-labile hydrazone bond to obtain materials that can self-assemble to form drug-loaded micelles, which play a similar role[213].

The narrative continues with micelles composed of materials boasting AIE characteristics. Zhuang et al.[214] developed micelles using mPEG-P (TPE-*co*-AEMA) copolymer. Similarly, a study[174] used a mPEG-NH_2-grafted TPE−COOH conjugate to create AIE micelles loaded with DOX for tracing anticancer drug delivery. The release of DOX from these micelles into cell nuclei was tracked, while TPE-mPEG remained in the cytoplasm, observable through fluorescence intensity changes. Another research[172] involved conjugating polyethyleneimine (PEI) with TPE−COOH and palmitic acid to form TPEI micelle-like nanoparticles, enhancing gene delivery performance and tracking capability. Additionally, Zhang et al.[215] fabricated a unique nanoprobe (M-Bis(4-(*N*-(2-naphthyl) phenylamino) phenyl)-fumaronitrile combining AIE dye NPAPF and gold nanoparticles in micelles for fluorescence/CT dual imaging. Semi-quantitative biodistribution (fluorescence + Inductively Coupled Plasma Mass Spectrometry, ICP−MS) confirmed enhanced tumor accumulation in mice *via* EPR effect[215]. Combining AIE with metallic probes enables multimodal validation of targeting efficiency. This approach bridges imaging and therapy, accelerating clinical translation of nanocarriers.

To investigate micelle stability, a self-indicating micelle loaded with DOX was developed using AIE-functionalized polymers (D-α-tocopheryl PEG 1000 succinate (TPGS)-TPE)[51]. TPGS-TPE micelles exhibited "seesaw-like" fluorescence: intact micelles (blue TPE emission) *vs.* disintegrated micelles (recovered red

DOX emission). Ratios of DOX/TPE (590 nm/460 nm), <4, 4−40, or >40, were used to quantitatively indicate micelle stability. This self-reporting metric allows dynamic assessment of carrier integrity in complex biological media. Future formulations could use such feedback loops to auto-monitor drug release rates based on microenvironmental conditions.

In the realm of micelles and AIE technology, innovation knows no bounds. From targeted imaging to controlled drug release and micelle stability, these studies pave the way for novel approaches in nanocarrier research.

4.5.4. Nanoparticles

Innovations in AIE-based nanoparticles emphasize real-time tracking and stimuli-responsive functionality for cancer theranostics. The research by Wang et al.[216] presented pH-responsive, AIE-active nanoparticles fabricated by incorporating rigid, cage-shaped polyhedral oligomeric silsesquioxane with TPE, demonstrating enhanced photostability for prolonged live cell imaging. Similarly, THyD nanoparticles[175] combined TPE and DOX *via* a pH-responsive hydrazone bond, where initial FRET/ACQ quenching is reversed in lysosomes to indicate prodrug activation. Expanding on AIEgen integration, another pH-responsive polymeric nanoparticle was developed[185], combining an AIEgen, Isothiocyanate-functionalized tetraphenylsilole (TPS-NCS), and an ACQ PS, pheophorbide A, to trace the entire cancer therapy process. At physiological pH, green AIE fluorescence enables nanoparticle self-tracking; in acidic lysosomal environment of cancer cells, nanoparticles disassemble and restore pheophorbide A's red fluorescence and phototoxicity. Light exposure then triggers ROS generation and lysosomal membrane damage, causing nanoparticles reassembly, indicated by the resurgence of aggregated AIEgens' fluorescence[185]. These studies establish pH as a switchable reporter for nanocarrier disassembly and drug activation. The real-time spatial resolution of fluorescence changing provides a blueprint for designing tumor-acidity-targeted systems that minimize off-target toxicity.

For gene delivery, Yuan and co-workers[173] developed a ROS-responsive polymer by conjugating an AIE PS with oligoethylenimine, an effective DNA-binding fragment, using an aminoacrylate linker. This polymer can self-assemble to form nanoparticles in aqueous media, exhibiting bright red fluorescence due to the presence of the AIEgen TPECM. Their findings indicated that in the absence of light exposure, the intracellular nanoparticles colocalize with DNA within lysosomes. However, upon light irradiation, the fluorescence colocalization ratios decreased, signifying light-induced DNA release[173]. Additionally, an AIE dye (2-(2,6-bis((*E*)-4-(phenyl(4′-(1,2,2-triphenylvinyl)-[1,1-biphenyl]-4-yl)amino)styryl)-4*H*-pyran-4-ylidene)malononitrile, TPE-TPA-DCM) was encapsulated in surfactant polymers to form polymeric nanoparticles for siRNA delivery[217]. The colocalization of TPE and FAM signals near the cell nucleus indicated successful siRNA delivery to cancer cells. This real-time visualization of gene vector trafficking addresses a critical bottleneck in nucleic acid delivery, potentially enabling rational design of non-viral carriers with enhanced nuclear translocation efficiency.

Morphological control was achieved in NCssG nanoparticles[188], formed by co-assembling AIEgens (NPAPF) with a redox-responsive camptothecin-gemcitabine amphiphilic prodrug (CPT-ss-GEM), where the AIEgen transformed the morphology of CPT-ss-GEM from nanowires to spherical nanoparticles. The study showed that spherical NCssG nanoparticles have stronger penetration ability than fibrous nanoparticles, and after administration in tumor-bearing mice, the liver and tumor were the primary targets[188]. This demonstrates how AIE-guided nanocarrier geometry optimization can overcome biological barriers in tumors, informing future material design principles.

Prodrug activation monitoring was realized with TPE-Pt(IV)(linker)-DOX conjugates[218]. TPE fluorescence was initially quenched by FRET, allowing only DOX fluorescence to be detected. While the initial quenching was reversed upon intracellular Pt(IV) reduction to Pt(II), the signaling drug activation process was affected. Such "fluorescence-on" activation reporting provides direct validation of prodrug conversion.

Biomimetic strategies yielded breakthroughs like natural killer (NK) cell-mimicking nanoparticles encapsulating an NK cell membrane around a highly bright NIR-II AIE-active conjugated polymer, pyridal[2,1,3]thiadiazole-based semiconducting polymer (PBPTV)[190]. These nanoparticles not only serve as photothermal agents for brain tumor therapy but also enable enhanced imaging and targeted delivery. These nanoparticles achieved longer circulation and brain-tumor-specific accumulation, enabling through-skull-scalp fluorescence imaging and PTT[190]. Another biomimetic nanoparticle, red blood cell (RBC)-O_2/(TQ)@ PB, combines an NIR-II AIE PS (PEG_{250}-TQ), a Prussian blue (PB) photothermal agent, and self-oxygenation perfluorocarbon within an erythrocyte membrane for PTT and PDT combined granuloma-targeted tuberculosis therapy[219]. The AIEgen enables real-time fluorescence tracking of nanoparticles to monitor their granuloma accumulation. Coated with an erythrocyte membrane, the nanoparticles exhibit prolonged circulation and selective retention in TB granulomas, as demonstrated in a tail granuloma model: AIE-guided imaging revealed peak accumulation at 24 h and sustained retention for 48 h. The study establishes a quantitative biodistribution model for chronic infectious disease targeting, proving that erythrocyte membranes reprogram nanoparticle PK to enhance lesion-specific accumulation. Overall, the fusion of cellular homing mechanisms with AIE tracking exemplifies a paradigm shift toward immune-evasive, tumor-homing "stealth" carriers.

Lipoprotein-mimicking nanoparticles also belong to a common biomimetic nanoplatform. By covalently decorating cyanine dyes with bulky AIE motifs, the authors suppressed $\pi-\pi$ stacking-induced fluorescence quenching, presenting a series of novel NIR-II emissive AIE cyanine dyes[220]. These probes have been encapsulated for fluorescence imaging-guided PTT therapy of glioblastoma.

For targeting delivery and multi-scale imaging, Li and colleagues[221] developed a targeted AIE dot (T-TTD dot) for image-guided PDT to treat cholangiocarcinoma (CC). These nanoparticles exhibited more intense red fluorescence in the human CC cell line compared to other cell lines, and noninvasive fluorescence imaging post-tail vein injection in tumor-bearing mice showed time-dependent biodistribution and tumor-preferential aggregation of T-TTD dots[221]. Another study introduced BETT-2, which, when formulated into nanoparticles, serves as a multifunctional theranostic platform for NIR-II fluorescence-photoacoustic-photothermal trimodal imaging-guided PDT-PTT synergistic therapy in orthotopic breast cancers[222]. Under 1064 nm excitation with a 1250 nm long pass (LP) filter, negligible background interference was observed in untreated mice. Notably, within 3 h post-injection, BETT-2 nanoparticles exhibited pronounced tumor accumulation *via* the EPR effect, as evidenced by spatially resolved NIR-II fluorescence signal. Maximum intratumoral enrichment occurred at 12 h, correlating

with peak fluorescence intensity, which underscores the AIE probe's capacity to dynamically track nanocarrier localization and retention. Remarkably, all tumors were completely eradicated by Day 3 in the BETT-2 nanoparticles with NIR-II laser irradiation group, demonstrating the synergistic efficiency of AIE-guided PDT-PTT. These platforms validate AIE's capacity to unify precision targeting, multi-scale imaging, and combination therapies, which can accelerate clinical translation of nanotheranostics.

4.5.5. Others

This section focuses on the application of AIEgen in other nanocarriers, in addition to the above-mentioned kinds. To track the gene transfer process, Zhang et al.[223] developed a TPE-derived small-molecule gene vector, which can form brightly fluorescent nanofiber complexes (pDNA@TR4) with plasmid DNA (pDNA). After labeling pDNA with Cy5, distinct colors were observed under CLSM for pDNA, TR4, and pDNA@TR4. The study revealed sequential cellular interactions: membrane attachment, internalization, and lysosome-escaping. Building upon this, transferrin (Tf) coated TR4 mimicked viral envelopes for targeted siRNA delivery (TR4@siRNA@Tf)[224], where AIE fluorescence enabled real-time transfection monitoring while Tf coating enhanced gene silencing efficiency. These works elucidate AIE-enabled non-lysosomal gene delivery mechanisms, providing paradigms for designing nucleic acid carriers that bypass enzymatic degradation.

Liow and team[171] prepared a thermogelling copolymer, poly (PEG/poly(propylene glycol)/TPE urethane), capable of self-assembling into micelles or hydrogels in aqueous solution, depending on its concentration, which shows strong emission due to TPE aggregation. Hence, the AIE thermogel can be traced within human epithelial cells and found to be taken up *via* energy-dependent endocytosis. *In vivo*, after injection of DOX-containing AIE thermogelling solutions into tumor-bearing mice, the formed gel depot was also traceable *via* fluorescence changes, allowing drug release monitoring. This pioneering system visualizes nanocarrier phase-transition dynamics, revealing correlations between supramolecular organization and drug release profiles.

Wang and coworkers[225] formulated tumor-mitochondria-dual-targeted nanocage by genetically fusing the tumor-penetrating peptide (linear TT1 peptide) with human H-chain ferritin, confining AIEgens (*e.g.*, MeTTMN) to enhance fluorescence intensity and ROS generation. Leveraging the inherent NIR emission of AIEgens, the AIEgen-protein nanoparticles enabled real-time tracking of tumor accumulation *in vivo*, validating their dual targeting capability toward liver cancer cells and mitochondria. This strategy successfully achieved imaging-guided photodynamic cancer therapy, demonstrating synergistic integration of diagnosis and treatment through AIEgen-mediated fluorescence visualization and ROS-triggered tumor ablation.

Zhang et al.[226] engineered a biomimetic nanoplatform by encapsulating an AIE photothermic agent and Dox into thermo-/pH-responsive nanogels (poly(*N*-isopropylacrylamide-*co*-acrylic acid, PNA), cloaked with 4T1 mammary tumor cell membranes for active targeting. Using a full-spectrum fluorescence imaging system, TN revealed the dynamic biodistribution of the nanocarrier in 4T1 tumor-bearing mice, showing progressive tumor accumulation peaking at 24 h post-injection—a critical window for initiating PTT. This AIE-guided spatiotemporal precision confirmed that tumor membrane camouflage enhanced intertumoral retention by 3.27-fold compared to non-targeted counterparts, directly correlating with therapeutic outcomes. Subsequent *in vivo* antitumor studies demonstrated superior tumor suppression (Tumor Growth Inhibition = 92.9%) in the nanoplatform plus laser irradiation group, highlighting AIE's dual role in optimizing treatment timing and realizing synergistic efficacy.

In regenerative medicine, AIE dots enabled longitudinal tracking of adipose-derived stem cells over 18 days post-transplantation in a skin injury model, revealing cell migration dynamics[189]. This breakthrough overcomes limitations of conventional cell trackers, providing unprecedented insights into stem cell engraftment kinetics to accelerate translational applications.

Lastly, Wang et al.[44] formulated AIE nanoliposomes TR4@Lipo to decode protein corona effects on liposome transportation in cells, enabling the visualization of liposomes through TPE fluorescence. Findings indicated that corona formation alters TR4@Lipo's cellular delivery mechanism, shifting from energy-independent membrane fusion to energy-dependent caveola-mediated endocytosis. Additionally, using DOX as a model drug revealed that protein corona formation did influence the intracellular distribution of the cargo. The direct visualization of corona-induced delivery pathway switching reveals a dynamic bio-nano interface, informing future designs of "stealth" carriers through intentional corona engineering.

5. ACQ

5.1. Rationale of ACQ and ACQ-based nanocarrier imaging

ACQ refers to a unique phenomenon of self-aggregation of lipophilic fluorophore molecules through intermolecular $\pi-\pi$ stacking in an aqueous solution, leading to energy dissipation from the excited state *via* non-photon emitting pathways[227]. This quenching effect significantly diminishes fluorescence output and is generally regarded as unfavorable in the context of bioimaging applications[228]. To overcome the limitations imposed by ACQ, several strategies have been developed. Among these, the most prominent are the engineering of AIEgens[229], and the integration of small-molecule ionic isolation lattices into traditional probes. The incorporation of this serves to spatially and electronically separate dyes, thereby mitigating the effects of concentration quenching[230].

The mechanisms of ACQ (Fig. 8A) could be understood by analyzing the energy transfer process of aggregation and disaggregation of fluorophores[231,232]. Once an electron is excited, there are many ways to dissipate energy, namely, radiation and non-radiation. The ACQ phenomenon mainly involves non-radiative pathways. Numerous processes contribute to the reduction of energy in molecules, with vibrational relaxation and internal conversion being commonly observed due to their quick occurrence (Fig. 8A). However, these processes typically do not play a major role in the specific quenching observed in ACQ, which is often dominated by intermolecular interactions that lead to rapid non-radiative deactivation of the excited state. Beyond these mechanisms, the ACQ phenomenon might also involve the formation of H-aggregates (Fig. 8A)[233-240]. Additionally, excimer theory, which includes the creation of non-fluorescent dimers and the transfer of energy to these dimers[241,242], and the collisions between excited fluorophores, is also relevant (Fig. 8A).

A variety of analytical tools are available to study the aggregates. Techniques such as atomic force microscopy, field emission scanning electron microscopy, and DLS allow for the direct visualization of aggregate morphology and size. Spectroscopic analysis of absorption and emission spectra provides insight into

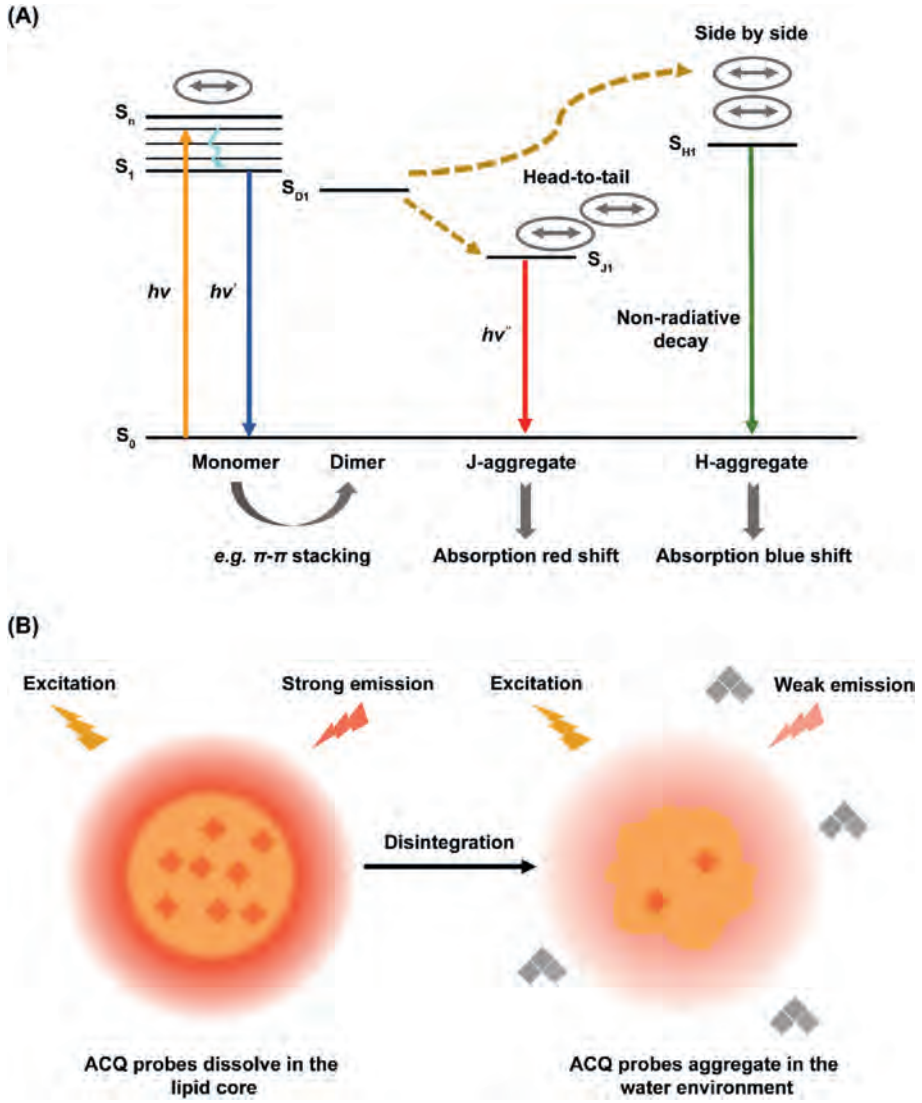

Figure 8 (A). The possible mechanism of ACQ probes. In this diagram, we see how fluorescent molecules behave differently based on their aggregation state. In isolation, monomers absorb light and re-emit it efficiently, showing strong fluorescence. When they pair up to form dimers or organize into head-to-tail J-aggregates through $\pi-\pi$ stacking, the absorbed light shifts to a longer wavelength, a process known as red shift, which typically results in enhanced fluorescence due to the aligned energy states. In stark contrast, molecules that aggregate side-by-side form H-aggregates, leading to a blue shift in absorption and significant fluorescence quenching. Here, the energy absorbed from light is not re-emitted but instead released as heat through non-radiative decay pathways, a hallmark of the ACQ phenomenon. (B) ACQ probe dynamics in nanocarrier systems: This illustration captures the fundamental principle of ACQ probe behavior in nanocarrier applications. Initially, ACQ probes are encapsulated within nanocarriers, where they remain isolated and fluorescent upon excitation. As the nanocarriers partially degrade, some ACQ probes are released into the aqueous environment, leading to their aggregation. This aggregation results in the quenching of fluorescence, a distinct shift from the bright emission seen when encapsulated. The contrast between the bright fluorescence of probes within intact nanocarriers and the quenched fluorescence of the released, aggregated probes, serves as a critical indicator of nanocarrier disintegration and release dynamics in biological environments.

how the aggregation state correlates with spectral shifts. For predicting the formation and dissociation mechanisms of aggregates, approaches like density functional theory, computational chemistry, and molecular dynamics (MD) simulations offer predictive insight. For instance, MD simulations have been employed to probe the underlying mechanisms of ACQ probes[43].

In one such study, the addition of 30% acetonitrile was used to simulate hydrophobic microenvironments, revealing that aggregation behavior varied markedly across different probe designs. Researchers found that the positioning of functional groups and intrinsic binding poses were key factors influencing the reillumination of ACQ probes[43]. These mechanism-oriented investigations are critical for guiding the rational design and high-throughput screening of next-generation ACQ probes, thereby enhancing the reliability of nanocarrier-tracking data derived from such systems.

When applying ACQ probes to monitor the *in vivo* fate of nanocarriers[243], it is important to acknowledge that not all nanocarriers are suitable for such use. The ACQ probe is best suited to trace nanocarriers that meet specific requirements, such as uniform distribution of probes within carrier materials, proportional release of probes upon degradation, and a slower water diffusion rate into the carrier than carrier degradation[9]. By fulfilling these prerequisites, premature quenching of the ACQ probe before carrier destruction due to water soaking can be avoided, enabling the establishment of a reliable relationship between fluorescence intensity and carrier quality to facilitate quantitative analysis of the intact nanocarrier (Fig. 8B).

For example, solid lipid nanoparticles (SLNs) are an ideal model due to their ability to gradually release the drug in a degradation-triggered manner and the strong encapsulation competency of their hydrophobic lipid core toward ACQ probes[70,244]. Additionally, for lipid nanocarriers, conducting *in vitro* lipolysis experiments is essential[245]. These experiments verify if the nanocarriers follow the expected degradation-triggered release pattern and ensure that the ACQ probes do not leak prematurely, maintaining the integrity of the fluorescence signal until nanocarrier degradation[245]. NCs, though not lipid carriers, also fulfill these criteria[246]. Moreover, the simultaneous measurement of both released drugs and NCs is possible when integrating free drug analysis methods like HPLC, providing a deeper understanding of the drug release mechanism from nanocarriers.

In summary, understanding the molecular basis of ACQ and implementing strategic probe-carrier pairings are essential for leveraging ACQ-based imaging as a reliable tool in nanomedicine. Rational probe design, supported by mechanistic studies and advanced imaging validation, can unlock the full potential of ACQ fluorophores in tracking nanocarrier behavior with both spatial and quantitative precision.

5.2. Structural insights into ACQ probes and their optimization for bioimaging applications

ACQ is prominently observed in planar, hydrophobic fluorophores such as coumarins, cyanine dyes, rhodamines, and related derivatives[247]. These molecules tend to aggregate in aqueous environments due to strong $\pi-\pi$ interactions, leading to fluorescence loss *via* non-radiative decay pathways. However, the extent of fluorescence quenching varies across different molecular structures; in many cases, residual fluorescence persists, and complete quenching is not achieved. However, fluorophores with a core structure of boron-dipyrromethene (BODIPY) or aza-BODIPY exhibit a more pronounced sensitivity to water[247]. The most distinct feature of this type of fluorophore is the instantaneous and absolute fluorescence quenching upon contact with water. Table 3[43,248,249] lists typical ACQ probes utilized in bioimaging investigations.

Despite their potential, ACQ probes present inherent limitations. A critical concern is fluorescence reillumination, where quenched dyes regain fluorescence upon redistribution into endogenous hydrophobic compartments, such as micelles formed during lipid digestion, or within hydrophobic domains of proteins and biomembranes. This phenomenon can confound the interpretation of nanocarrier fate by introducing false-positive signals. Therefore, it becomes necessary to distinguish intact nanocarrier-derived signals from those associated with metabolic byproducts or physiological environments. Additionally, enhancing the cohesion of probe aggregates through structural modification is required to address this reillumination challenge.

A notable study analyzed the phenomenon of fluorescence reillumination in various organic solvents and aqueous environments[245]. The findings of the study indicate that P4 exhibits a greater degree of rekindling in all systems compared to P2. This can be attributed to the weaker hydrophobic forces of P4, which allow for easier redissolving or solubilization[245].

While most previous findings suggest a mild degree of reillumination, often managed by using prequenched dyes as controls or by increasing the fluorescence detection limit to reduce autofluorescence and reillumination interference, the possible influence of reillumination and autofluorescence should not be neglected in the elucidation of *in vivo* results[43,247]. Therefore, Cai and colleagues[43] implemented strategic modifications to improve the physicochemical robustness of ACQ probes. The methods utilized for modification were based on previous findings that enhancing the hydrophobic and planar characteristics of fluorophore molecules can promote $\pi-\pi$ stacking. These modifications aimed to heighten the probe's water sensitivity and the stability of the quenched aggregates. They rigidified and/or augmented the aza-BODIPY parent structure with methoxy or acetoxy groups. The optimized structures displayed improved quantum yields, heightened photostability, rapid quenching kinetics, and minimal reillumination in complex biological media (*e.g.*, blood, plasma, and surfactant solutions like 1% Tween-80)[43]. These results reinforce the importance of planarity and hydrophobicity in designing high-performance ACQ fluorophores.

While imaging in the NIR II range (700−1100 nm) offers numerous advantages, including significantly reduced background absorption, light scattering, and autofluorescence, as well as improved tissue penetration[250], the emission wavelength of current ACQ probes is not sufficiently long to eliminate autofluorescence interference. *In vivo* imaging, despite being a relatively straightforward method, is limited by the challenge of

Table 3 Typical ACQ probes utilized in bioimaging investigations.

Name	Chemical structure	$\lambda_{ex}/\lambda_{em}$ (nm)	Ref.
Aza-BODIPYs	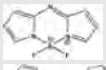	731/752	43
FD-C7		705/737	43
FD-B21	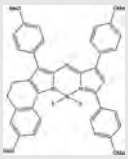	708/732	248
P2		651/662	249
P4			

BODIPY, boron-dipyrromethene.

light penetration through biological tissues. Consequently, researchers often must rely on directly observing dissected internal organs and tissues to study nanocarrier distribution, and the precision of these observations can be affected by the methodologies used in the treatment process. Newer ACQ probes are being developed with a more redshifted emission wavelength (>1000 nm), which will further minimize interference from tissue autofluorescence[251], and these are expected to exhibit even lower fluorescence reillumination[252,253].

Encouragingly, traditional fluorophores such as 1,1′-dioctadecyl-3,3,3′,3′-tetramethylindotricarbocyaine iodide (DiR) have shown potential in transforming into ACQ probes, particularly in water sensitivity screening tests[43,247]. FITC, Rhod B, and cyanine dyes have also been reported to have the ACQ effect[254,255]. However, it is critical to distinguish genuine ACQ probes from general water-sensitive fluorophores. True ACQ systems should meet four key criteria: (1) excellent water sensitivity; (2) complete fluorescence quenching; (3) absence or negligible reillumination; and (4) fast quenching[33].

Interestingly, these features are often co-dependent, emerging synergistically from optimized molecular architecture. Structural optimization reveals that enhanced hydrophobicity and planarity of the fluorophore molecules strengthen the cohesion of the aggregates formed, thus resulting in enhanced water sensitivity, complete quenching, and minimized reillumination. Although not all water-responsive dyes qualify as ACQ probes, the rediscovery and structural refinement of classical fluorophores offer a promising path for the development of novel, high-performance ACQ systems.

5.3. Application of ACQ in nanocarrier bioimaging

The ACQ probe currently serves as a valuable tool in conducting semiquantitative assessments of nanoparticle behavior *in vivo* and at the cellular level. However, it is anticipated that the probe will ultimately shift toward a more quantitative approach soon. Our group has utilized the environment-responsive ACQ to investigate the fate of different kinds of nanocarriers *in vivo* after being administered *via* various routes[39,256-259]. This review paper showcases a selection of recent and significant advancements in the field, including research findings from other groups that have utilized ACQ probes in their studies.

However, the PK analysis methods of nanocarriers presented in the literature primarily adhere to traditional PK theories and models. Given the relatively large size of nanocarriers, their *in vivo* disposal mechanisms differ significantly from those of molecular drugs. Therefore, analyses based on conventional PK models may not accurately reflect the true behavior of these nanocarriers. This discrepancy emphasizes the necessity of developing a kinetic theory specifically tailored to particulate systems.

5.3.1. Nanoparticles

This section explores key applications of ACQ probes in nanoparticle (PCL nanoparticles and SLN) research, advancing our understanding of nanocarrier biodistribution and kinetics[260].

As amphiphilic block copolymer-based carriers, mPEG-PCL nanoparticles featuring a hydrophobic PCL core for drug encapsulation and hydrophilic PEG corona for stealth properties enable prolonged circulation and reduced opsonization. When combined with ACQ probes, they can serve as indispensable platforms for decoding nanocarrier PK and biodistribution dynamics.

The fate and *trans*-epithelial transport of orally administered PCL nanoparticles of various sizes (50, 200, 600, and 2000 nm) were studied using P2 or P4 probes[261]. The stability assessment showed that the hydrophobic nature of both PCL and the probes effectively hindered probe leakage and water infiltration. Live imaging in rats that received P2 quenched solution showed limited fluorescence, addressing reillumination interference concerns. The qualitative analysis indicated that larger particles had shorter gastrointestinal retention time, while smaller ones were more likely to be absorbed and reach mesenteric capillaries or lymphatic vessels[261]. Cellular uptake and *trans*-monolayer transport studies using P4-labeled nanoparticles revealed that only 50 nm-sized nanoparticles could undergo both enterocyte and M cell-mediated transcytosis[261]. These findings establish particle size as a master regulator of oral absorption pathways, guiding rational design of gut-targeted carriers.

Li and co-workers[262] developed a physiologically based pharmacokinetic (PBPK) model using P2-tracked mPEG-PCL nanoparticles, by fitting organ-level concentration data in mice. This model provides a computational blueprint for predicting nanocarrier biodistribution, enabling *in silico* screening of formulation variables before costly *in vivo* trials[262].

Research on drug-loaded nanoparticles is often more complicated. Fan and coworkers[40] used the P2 probe to label mPEG-PCL nanoparticles loaded with DOX, aiming to revalidate their prolonged circulation effects. They established a linear relationship between fluorescence intensity and nanocarrier concentration, revealing nanoparticle rapid elimination and L-type biphasic kinetics. On the other hand, the study also noted a faster clearance rate of DOX compared to the nanocarriers, indicating potential DOX leakage post-administration[40]. This quantification framework provides a standardized method for tracking intact nanoparticle PK, highlighting drug leakage as a critical unsolved flaw. Future nanocarriers could incorporate leakage-monitoring mechanisms to optimize drug retention. Another study on curcumin-loaded PCL nanoparticles[249], researchers investigated their intranasal fate using P2 and P4 probes. It was found that these nanoparticles, whether PEGylated or not, permeated into the mucosa and trigeminal nerves but did not reach the olfactory bulb. Notably, the absence of fluorescence in major organs suggested minimal absorption through the nasal vascular pathway. Curcumin and P4 signals detected in the brainstem and midbrain 2 h post-administration indicated the trigeminal nerve's importance in nose-to-brain delivery of intact nanoparticles[249]. This clarifies neural pathways for intranasal delivery, directing future neurological nanotherapeutics toward trigeminal-optimized formulations rather than olfactory targeting.

Due to its inherent imaging advantages, NIR-II probes have always been a hot spot for researchers to synthesize. ACQ984 was introduced to address the imaging advantages of the NIR-II ACQ probe in tracking nanocarriers *in vivo*[252]. Compared to conventional probes (*e.g.*, ICG, IR-1061), ACQ984 exhibits minimal fluorescence reillumination (<1%) in complex biological media, ensuring reliable correlation between fluorescence signals and intact nanocarriers. The probe's label stability across diverse nanocarriers (PM, PCL nanoparticles) and its ability to establish strong *in vivo*−*ex vivo* correlations for PK analysis highlight its utility in real-time, non-invasive monitoring of nanocarrier biodistribution and clearance. Its minimal signal reillumination sets a new standard for quantification fidelity, making it indispensable for clinical translation studies that require absolute nanocarrier tracking accuracy.

The work of Liu et al.[253] shows the synthesis and screening process of the NIR-II ACQ probe. By rotation restriction of aryl substituents and introduction of electron-donating moieties, ACQ1−ACQ14 were synthesized. Theoretical calculations and experiments verified that molecular planarity is more important than hydrophobicity for ACQ properties. Based on water sensitivity and quenching stability, ACQ1 was selected as the best NIR-II ACQ probe with fluorescence reillumination *in vivo* of less than 2.5%, which was far less than that of the commonly used NIR-I ACQ probe P2 (15%). Therefore, NIR-II ACQ probes, with their superior tissue penetration and reduced autofluorescence, enable non-invasive, high-resolution tracking of intact nanoparticles' biodistribution. This molecular design principle revolutionizes ACQ probe development, prioritizing rigid planar structures over traditional lipophilic motifs.

Building on these findings, intraperitoneal PCL nanoparticle tracking using ACQ1 revealed size-dependent fates[260]. Key findings reveal that smaller particles (<30 nm) rapidly enter systemic circulation, achieving the highest blood concentrations, while larger particles (>1000 nm) exhibit prolonged peritoneal retention, making them ideal for intraperitoneal disease treatment. Notably, 200 nm particles demonstrate significant lymph node accumulation, highlighting their potential for lymphatic disease targeting. These discrete size thresholds provide a roadmap for precision intraperitoneal therapy: sub-30 nm for systemic exposure, 200 nm for lymphatic diseases, and micron-scale for localized peritoneal treatment.

SLNs, composed of biocompatible lipid matrices, excel in overcoming biological barriers to targeted therapeutic delivery by oral or pulmonary administration. Their high lipid content enables efficient ACQ probe encapsulation, minimizing leakage and ensuring reliable tracking of intact particle fate. Thus, the fate of SLN can be well studied with ACQ probes.

A study investigated the influence of surface charge on the *in vivo* transport of orally delivered intact SLNs[244]. Three types of SLNs were assessed: anionic (with sodium dodecyl sulfate), cationic, and neutral (a mix of unmodified and anionic SLNs with bile salt). The fluorescence intensity of these SLNs was quantified using total radiant efficiency (TRE) through the Region of Interest (ROI) method. The study results redefine oral nanocarrier optimization priorities, suggesting that hydrophilicity may outperform surface charge modification strategies for enhancing intact SLNs' oral absorption[244].

Another study focused on improving the oral absorption of lipid-based carriers, often hindered by lipolysis in the GIT[70]. The study compared the effects of incorporating the lipase inhibitor orlistat and PEG modification on particle absorption. SLNs were labeled with P2 or P4 probes to track their *in vivo* behavior. The study concluded that inhibiting lipolysis, particularly with orlistat, is more effective than PEG modification in enhancing particle absorption. It also revealed a "high absorption and low penetration" transport mode for nanoparticles in cells, based on the disparity between cell uptake and particle transport through the cell monolayer[70]. The results advocate for enzymatic barrier disruption over steric stabilization in oral delivery. Further research[263] employed P4 to investigate how particle size affects the cellular uptake, accumulation, and distribution of SLNs. This study found that larger SLNs were more likely to be taken up by A549 cells and less likely to be cleared by macrophages, providing valuable insights for designing macrophage-escape systems based on particle size.

Furthermore, the application of ACQ probes extends beyond solely nanoparticle analysis to evaluating medical instruments[264,265]. SLN suspensions encapsulating ACQ probes or conventional probes and varying in size were used to assess the performance of the endotracheal aerosolizer device HRH MAG-4[245]. A positive correlation was found between particle size and lung retention time for P2-SLNs and DiR-SLNs in the 120−480 nm range, indicating that SLNs primarily remain intact in the lungs with little degradation within 12 h of administration[245]. Comparing the fluorescence intensity of P2-SLNs and DiR-SLNs in primary organs, P2-labeled groups showed considerably lower intensity, attributed to significant SLN degradation during transportation, leading to P2 quenching[245]. These findings establish particle size as a key determinant of pulmonary residence time, informing inhalable nanocarrier design for controlled drug release in respiratory diseases. For pressurized metered-dose inhalers (pMDIs)[265], P4-labeled SLN-based pMDI (P4-SLN-pMDI) was optimized for studying their *in vivo* fate under adult breathing simulation conditions. The amount of P4 on the filter membrane was measured by its fluorescence intensity, and then further converted into the amount of nanoparticles. The study revealed that about 6.87 ± 2.66% of the total particles per bottle were inhaled into the simulated larynx[265]. The calculation of particle exhalation efficiency can reflect the advantages and limitations of key equipment and can promote the redesign of nanoparticle engineering inhalers to improve lung deposition.

In conclusion, the studies discussed in this section collectively underscore the critical role of ACQ probes in nanoparticle research. From analyzing blood kinetics to investigating nanoparticle distribution and absorption in various biological systems, these probes offer essential insights, significantly contributing to the advancement of nanomedicine.

5.3.2. NCs

This section explores pivotal advancements in understanding the *in vivo* fate of NCs, historically hindered by measurement limitations. The incorporation of ERFs into NC lattices enables precise tracking without altering intrinsic properties[266].

Xie and colleagues[248] utilized P2-embedded cyclosporin A (CsA) ultrafine amorphous particles for IVIS observation and P4-embedded particles for CLSM measurements. This approach traced the NCs *via* fluorescence imaging, establishing the feasibility of incorporating ACQ dyes into NCs to monitor their fate. Furthering this approach, self-discriminating hybrid NCs of curcumin[61,246], CsA[267], and quercetin[268] were also developed by embedding traces of P2 or P4 dyes into the crystalline lattices of NCs. These studies investigated the NCs' *in vivo* fate after various administration methods, including intravenous injection, transdermal, ocular, and oral, without interference from free probes. A 2021 study validated the use of an ACQ probe in quantifying and tracing fenofibrate hybrid NCs, establishing a strong *in vitro/in vivo* correlation and marking a significant advancement in the field[269].

Shen and colleagues[270] investigated the biological fate of quercetin hybrid NCs (QT-HNCs) of approximately 280 and 550 nm diameters following oral and intravenous administration. They estimated the contribution of integral NCs to QT's oral bioavailability, finding significant absorption of intact QT-HNCs, thus enhancing QT's absorption. Another study[271] focused on the fate of herpetrione amorphous nanoparticles (HPE-ANPs) post-oral administration, adding either P2 or P4 during the solvent-antisolvent precipitation process. Live imaging indicated significant fluorescence in the rat abdomen for 8 h, with *ex vivo* imaging of the GIT corroborating these findings[271]. The TRE measurements suggested that ANPs primarily either degrade or

are absorbed in the small intestine. Assessments of particle size impact on distribution in key organs indicated that integral HPE-ANPs played a minor role in overall bioavailability. The *in situ* perfusion model results showed HPE-ANP absorption mainly in the ileum, and subsequent cellular uptake studies using Caco-2 cell models revealed that enterocytes could internalize intact ANP, but only a few ANP could penetrate the monolayer cells[271]. The same methodologies were applied to explore the *in vivo* fate of these preparations following intravenous administration[272]. Following intravenous administration, blood fluorescence rapidly decreased, indicating the swift clearance of intact particles from circulation. *In vivo* imaging revealed that larger particles are more readily captured by the reticuloendothelial system (RES) organs. For a comprehensive understanding of the biological and intracellular fates of drug NCs *via* various delivery routes, readers are encouraged to refer to the 2022 review on this topic[266].

In summary, the studies in this section collectively illustrate the significant progress in the field of NC research. Through the innovative use of ACQ probes, researchers have gained unprecedented insights into the *in vivo* behavior, distribution, and fate of NCs, enhancing our understanding of drug delivery mechanisms and nanomedicine.

5.3.3. Micelles

In the exploration of PMs as drug delivery systems, ACQ probes have emerged as a powerful tool for elucidating the *in vivo* behavior and functionality of these nanocarriers. A growing body of research has utilized ACQ probes to uncover the distribution patterns and cellular uptake mechanisms of PMs, offering transformative insights that are reshaping drug delivery strategies.

One pivotal study employed carboxymethyl chitosan-rhein (CR) PMs labeled with P4 to investigate their absorption by MCF-7 cells, revealing that the intact CR PM could effectively penetrate MCF-7 tumor cells rather than relying solely on diffusion of free drugs[273]. This demonstrated the importance of micelle integrity in enhancing cellular uptake efficiency. Further, in an *in situ* intestinal absorption model, ACQ probes confirmed that CR PMs could be internalized by Caco-2 cells and bypass P-glycoprotein (P-gp) mediated efflux, suggesting a dual role for the CR conjugates as both a carrier and a potential P-gp inhibitor, which is critical for improving oral drug bioavailability[274]. Building on this, researchers developed P2-labeled TPGS-modified CR PMs for oral PTX delivery[275]. Fluorescence tracking indicated that intact PMs could cross the gastrointestinal barrier and distribute systemically. Interestingly, discrepancies between fluorescence intensity and drug concentration in tumors revealed premature drug release in circulation, underscoring the need to optimize micelle stability for targeted delivery.

To enhance tumor specificity, glycyrrhetinic acid-modified carboxymethyl chitosan-TK-rhein (GCTR) was designed to form hepatoma-targeting and ROS-responsive celastrol/GCTR PMs[276]. The fluorescence intensity indicated by P2 shows strong liver-targeting capacity due to glycyrrhetinic acid receptor-mediated uptake. Cellular imaging employing P4 revealed significantly higher uptake of (P4 + celastrol)/GCTR PMs by HepG2 hepatic tumor cells compared to normal hepatocytes, highlighting the potential of receptor-targeted micelle design[276].

Additional investigations into jejunum absorption demonstrated that (PTX + P4) PMs formulated with TPGS exhibited superior transport efficiency, with M cells playing a more prominent role in the *trans*-monolayer transport of intact micelles compared to enterocytes[42]. These findings emphasize the importance of material composition and cellular pathways in designing effective oral nanocarriers.

In studies of polymeric mixed micelles (PMMs), combining Pluronic F127 and Solutol HS15 in different ratios, ACQ-labeled PMMs revealed that polymer composition profoundly influences uptake behavior and internalization pathways[277]. System I (1:4 ratio) exhibited greater uptake *via* energy-dependent mechanisms, pointing to the significance of micelle surface properties and polymer interactions in fine-tuning delivery efficiency[277].

Nasal-brain delivery research employing HIV-1 *trans*-activator of transcription (TAT)-modified mPEG-PDLLA PMs showed that ACQ probes like P2 enabled real-time tracking of intact micelle migration along the trigeminal nerve[278]. The enhanced uptake with higher TAT densities demonstrated how surface functionalization can dramatically improve *trans*-epithelial transport, offering new strategies for central nervous system (CNS) drug delivery. However, the encapsulated C6 signal was more dominant than the probe signal, suggesting that most of the drug diffused into the brain after release from the PMs[278].

In biodistribution studies, newly developed absolute ACQ (aACQ) probes such as FD-B21 and FD-C7 offered improved imaging fidelity compared to traditional probes, with reduced background fluorescence and minimal signal reillumination in organs (Fig. 9A)[43].

Fig. 9B demonstrates the *in vivo* imaging of PEG-PDLLA PMs labeled with aACQ probes compared against classical ACQ probe P2 and conventional probe DiR. The biodistribution patterns suggest that FD-B21 and FD-C7 have similar biodistribution to P2 but with reduced re-illumination in the liver and spleen[43]. In Fig. 9C−F, the normalized ARE is calculated to account for the varying fluorescence intensities of the administered PMs and quenched dyes. Fig. 9E underscores that, in contrast to the biodegradable nature of PEG-PDLLA PMs, DiR showed continuous fluorescence increase over 24 h within these organs. This counterintuitive result is attributed to DiR's pronounced re-illumination in the hydrophobic biological components, as further elaborated in (Fig. 9F)[43]. The findings suggest that aACQ fluorophores exhibit remarkable sensitivity to aqueous environments and minimal re-illumination of fluorescence, establishing their utility as precise bioimaging agents for nanocarriers.

Moreover, comparative analyses between the ACQ probe (FD-B21) and the FRET system (DiD/DiR) revealed that ACQ probes provide a more stable and accurate representation of micelle integrity, with lower rates of dye leakage and nonspecific accumulation, which benefits reliable PK evaluation[279].

Lastly, studies examining P2 or P4-labeled PM behavior in simulated gastrointestinal environment fluids revealed that bile salt-rich conditions can destabilize ACQ-labeled PMs, suggesting the need for testing PM stability under physiologically relevant fasted-state conditions[52]. This process partially elucidated the biological fate of PMs made from mPEG-PDLLA copolymers or DSPE-PEG. Results from the cell model indicated that the mucus layer impedes the absorption of larger PMs, particularly those with longer PEG chain lengths, highlighting the vital role of M cells in transporting intact PMs[52].

_under1Collectively, these studies illustrate how ACQ probes have revolutionized our ability to probe the fate of PM in biological environments. By revealing mechanisms of uptake, transport, distribution, and drug release of PM, ACQ-based tracking has laid a robust foundation for the rational design of next-

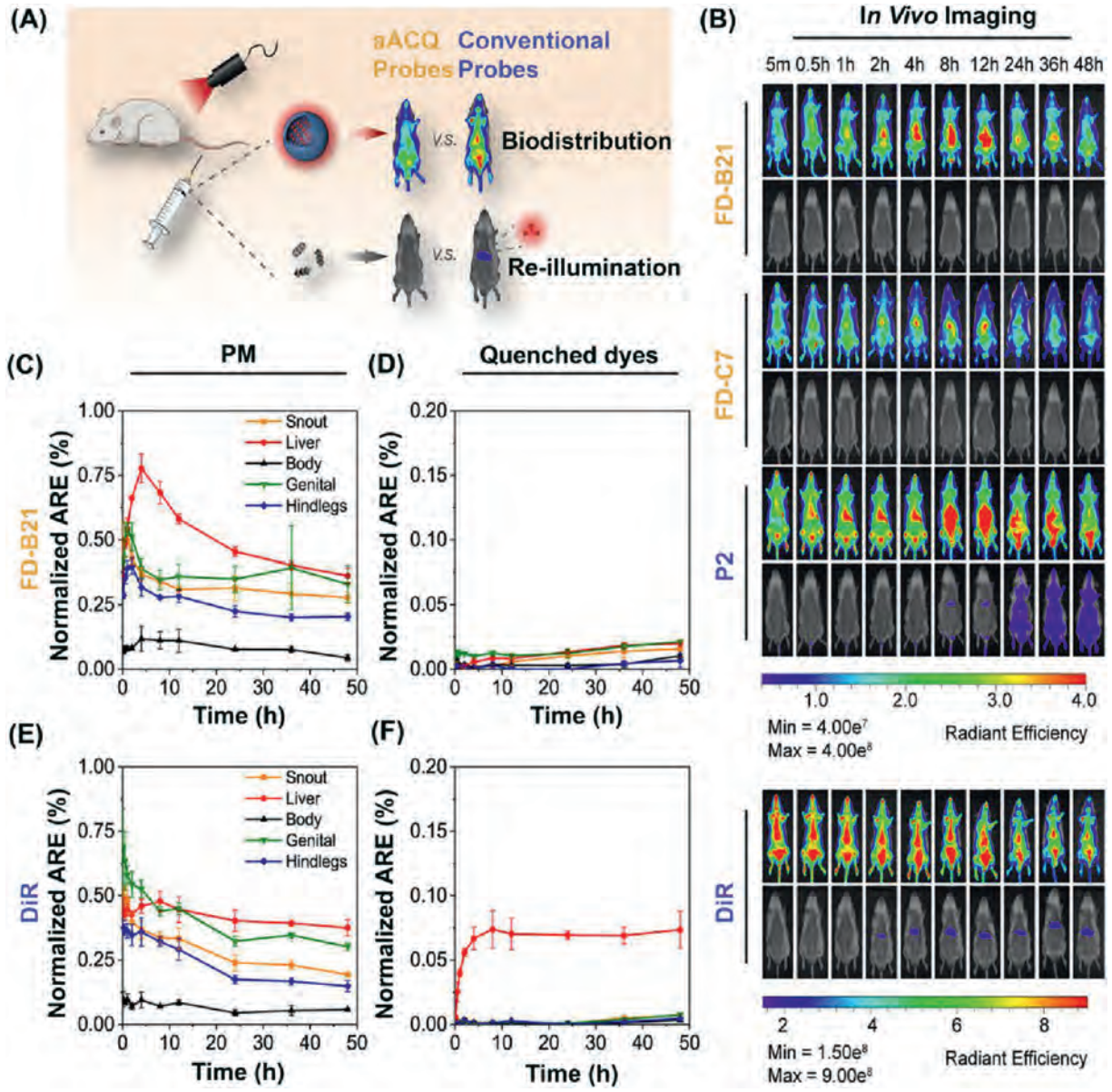

Figure 9 The *in vivo* tracking of biodegradable PEG-PDLLA PMs using novel aACQ probes. (A) Depicts the biodistribution of fluorescently labeled PMs post intravenous injection, monitored through an IVIS, alongside prequenched fluorophores to evaluate fluorescence re-illumination (B). FD-B21-labeled PMs peaked in fluorescence in peripheral organs at about 1 h, with liver fluorescence peaking at 4 h post intravenous administration (C). Intravenous administration of quenched FD-B21 fluorophore dispersions resulted in minimal fluorescent re-illumination within 48 h, indicating minimal pseudo-positive effects from aACQ probe labeling *in vivo* (D). The DiR-labeled group differed, showing maximum peripheral tissue signals at 5 min and a peak in hepatic fluorescence at 8 h post-administration (E). Moreover, DiR dispersions showed noticeable fluorescence re-illumination, suggesting a more pronounced effect from released dye aggregates (F). To summarize, normalized ARE reveals significant PM accumulation in the liver due to uptake by the MPS. Peripheral regions exhibited 3.6−5.8 times higher fluorescence intensity compared to trunk regions, with the highest intensity observed in the order of genital > snout > hindlegs > trunk, as shown by normalized ARE. It's important to note that while normalization of *in vivo* fluorescence allows for comparison between probes, these normalized percentages are not a quantitative measure of *in vivo* re-illumination due to the dynamic nature of *in vivo* processes and fluorescence attenuation by tissues. Reprinted with the permission from Ref. 43. Copyright © 2022 John Wiley and Sons.

generation PM systems with improved targeting, stability, and therapeutic efficacy.

5.3.4. Nanoemulsions

Recent research employing ACQ probes has significantly deepened our understanding of how nanoemulsions behave in biological environments, with critical implications for the design of more effective drug delivery platforms.

A noteworthy example is the work by Jiang and colleagues[280], who developed a lactoferrin (Lf)-modified Huperzine A (HupA) nanoemulsion for intranasal administration aimed at treating Alzheimer's disease. By incorporating the ACQ probe P2, they

traced the "nose-to-brain" pathway and PK of these formulations[281]. Remarkably, even after olfactory bulb ablation in rats, the fluorescence signal was detectable in brain areas after intranasal administration, suggesting that Lf-HupA-nanoemulsions could enter systemic circulation and reach the brain *via* the indirect nose-to-brain pathway. The stronger fluorescence signals in the Lf-modified group highlighted the contribution of ligand-mediated targeting in enhancing brain delivery[281]. This study underscores how targeted surface modifications can significantly impact therapeutic distribution, guiding future developments in non-invasive neurotherapeutic strategies.

Another critical study employed P2-labeled nanoemulsions of varying particle sizes (70, 200, 500, and 900 nm) to assess how size affects systemic behavior[282]. The findings demonstrated clear size-dependent biodistribution: smaller particles exhibited prolonged blood retention and gradual hepatic uptake, while larger particles were more rapidly sequestered by the spleen and lungs[282]. This size-dependent uptake pattern reveals how nanoemulsion design can be optimized to modulate organ-specific delivery or avoid MPS clearance, which is an essential consideration in tailoring drug carriers for specific therapeutic targets.

Furthermore, the application of ACQ probes to differentiate nutritional fat emulsions from various manufacturers provided key insights into how formulation variables influence biodistribution and PK[283]. Despite similar circulation profiles, organ-level differences were observed, reinforcing the importance of manufacturing consistency[283]. The ability of ACQ probes to detect subtle variations in organ accumulation emphasizes their value in quality control and comparative analysis of clinically used nanoemulsions.

Together, these studies demonstrate how ACQ probes enable real-time, non-invasive tracking of nanoemulsion behavior *in vivo*, offering critical insights into factors such as targeting efficacy, size-dependent distribution, and manufacturing impact. These findings not only refine our understanding of nanoemulsion pharmacology but also guide the rational design of next-generation nanoemulsions with improved utility.

5.3.5. Others

This section highlights the significant role ACQ probes play in uncovering the dynamic behavior of a wide variety of nanocarrier systems beyond the types mentioned above.

In the study of self-microemulsifying drug delivery systems (SMEDDSs), ACQ probes P2 and P4 were employed to investigate gastrointestinal lipolysis and transepithelial transport[284]. By evaluating fluorescence stability in various pH buffers and tracking relative fluorescence changes using semiquantitative ROI-based analysis, researchers were able to map *in vivo* lipolysis profiles, which followed first-order kinetics after oral administration. These findings revealed how SMEDDSs maintain their structural integrity during early digestion, while simultaneously enabling tracking of their *in vivo* distribution, PK, lymphatic transport, and cellular uptake[284]. This deepened our understanding of how SMEDDSs behave under physiological stress and demonstrated the potential of ACQ probes for monitoring the fate of intact formulations within complex biological environments.

Further extending this line of inquiry, studies on ionic coaggregates (ICA), formed by choline cations and fatty acids, shed light on novel nanocarriers designed for poorly soluble drugs[285]. P2 and P4 were used to track the *in vivo* transport of intact PTX-loaded ICAs and choline oleate in comparison to conventional cremophor EL-based micelles[285]. Interestingly, the early release of PTX was attributed not to structural dissociation of ICAs but to plasma protein extraction, highlighting a non-disruptive release mechanism. P2 fluorescence revealed that ICAs had longer intestinal residence times than micelles, correlating with their enhanced solubility and stability *in vivo*. Additionally, the increased cellular uptake of intact (PTX + ACQ) ICAs indicated that ICAs significantly increased PTX uptake in comparison to micelles, which could be attributed to their structure's similarity to the intermediate of lipid metabolism[285]. This work successfully presents structural biomimicry as a strategic direction for improving drug solubilization and uptake.

In the field of transdermal delivery, the integration of dissolving microneedles (DMNs) with nanocarriers like SLNs was explored

Table 4 The advantages and disadvantages of FRET, AIE, and ACQ techniques in the application of tracing nanocarriers' *in vivo* fate.

Technology	Advantage	Disadvantage
FRET	(1) High sensitivity to distance changes for monitoring nanocarrier integrity. (2) Quantitative capability *via* ratiometric measurements. (3) Widely applicable to diverse nanocarriers. (4) Enables real-time tracking of disintegration kinetics of nanocarriers.	(1) Complex calibration required (prone to errors from spectral crosstalk, orientation effects, etc.). (2) Probe leakage risk (physical encapsulation) or false signals (covalent conjugation). (3) Reduced accuracy in indicating intact nanocarriers due to probe detachment.
AIE	(1) "Turn-on" fluorescence in aggregated state (intact nanocarriers); quenched upon release. (2) Self-indicating nanocarriers possible (AIEgens as structural components). (3) Multifunctionality: can integrate therapy (PDT/PTT) with imaging.	(1) False positives: hydrophobic AIEgens may re-aggregate or bind biomolecules after release. (2) Quantification challenges: semi-quantitative correlation between fluorescence and carrier concentration. (3) Biocompatibility concerns: the universal pharmacological activity of AIEgens may alter nanocarrier function and fate.
ACQ	(1) "Turn-off" signal upon nanocarrier disintegration (quenching in aqueous milieu). (2) Simplified quantification: fluorescence intensity directly correlates with the intact nanocarrier concentration. (3) Minimal reillumination with optimized probes.	(1) Incomplete quenching: reillumination in hydrophobic biological environments (*e.g.*, lipid membranes). (2) Restricted applicability: mostly used in nanocarriers composed of materials with slow water diffusion rate and degradation-triggered release.

using the P4-labeled strategy[286]. Fluorescence imaging across different skin sites (ear, back, abdomen) revealed that site-specific factors influence the diffusion rate of SLNs, following the order: ear > abdomen > back. This suggests transdermal delivery efficiency can be optimized based on the site of application and specific disease requirements[286]. Furthermore, varying the length of DMNs (DMN-1200, DMN-800, DMN-400) demonstrated that while longer DMNs were observed to reach deeper skin layers and facilitated more rapid microneedle dissolution, they did not significantly affect the diffusion rate of SLNs[287]. These results suggest that optimizing nanocarrier delivery through the skin will require balancing microneedle design with site-specific physiological factors.

In conclusion, these studies collectively underscore the powerful role of ACQ probes in elucidating the complex behaviors of various nanocarrier systems. From self-microemulsifying systems to ICA and DMNs, ACQ probes provide invaluable insights into the behavior, distribution, and effectiveness of these novel drug delivery platforms, paving the way for more targeted and efficient therapeutic interventions.

6. Conclusions and future perspectives

The integration of FB in nanomedicine, particularly with the advent of ERFs based on FRET, AIE, and ACQ mechanisms, has significantly advanced our ability to monitor and understand drug nanocarrier systems *in vivo*. Their application has unraveled the complexities of drug release mechanisms and the intricate interactions of nanocarriers within biological environments, offering a clearer understanding of their behaviors and potential.

This review has outlined the distinct advantages and limitations of each ERF modality, which are summarized in Table 4. In summary, FRET systems offer high sensitivity and the ability to monitor dynamic molecular interactions in real time, but they suffer from spectral overlap, limited distance range, and potential donor-acceptor detachment. AIE-based probes overcome traditional ACQ limitations by exhibiting enhanced fluorescence upon aggregation, allowing high SNR in intact nanocarriers. However, their fluorescence correlation with nanocarrier concentration can be unpredictable, and post-release reaggregation may cause false-positive signals. ACQ fluorophores, in contrast, enable simple "turn-off" signal tracking upon nanocarrier degradation, offering intuitive readouts. Yet their susceptibility to reillumination and signal persistence in biological environments limits quantification accuracy.

Looking forward, significant progress is anticipated through the development of novel ERFs featuring enhanced chemical and photochemical stability, higher quantum yields, larger Stokes shift, and superior responsiveness to environmental changes. These improvements, combined with computational modeling and AI, will enable more precise prediction and monitoring of nanocarrier behaviors. Such advancements are not just incremental improvements; rather, they represent a paradigm shift towards the realization of personalized medicine. Enhanced bioimaging techniques are poised to enable the creation of highly targeted drug delivery systems, meticulously tailored to individual patient profiles, and optimized for maximum therapeutic efficacy.

Quantification of nanocarriers using fluorescence-based methods represents the forefront of current techniques, and strategies to reduce false-positive signals are critical. To overcome limitations in false-positive signals during nanocarrier tracking, technology-specific mitigation strategies are paramount. For FRET systems, covalent conjugation of donor-acceptor pairs to nanocarriers' material or utilizing improved techniques (*e.g.*, ALEX/PIE) minimizes spectral crosstalk and probe detachment artifacts. AIE systems require engineered water-soluble fluorophores to prevent post-release reaggregation and to validate the correlation between fluorescence and nanocarrier integrity. ACQ-based quantification demands the development of probes with a stronger fluorescence correlation with nanocarriers, supported by rigorous pre-quenching validation to suppress reillumination in physiological conditions.

In parallel, advances in nanocarrier material design, such as enzyme-resistant lipids and crosslinker-tuned polymers, can stabilize probe label stability, ensuring fluorescence signal transitions accurately reflect biological degradation. Computational models, including MD simulations, can guide the rational pairing of probes and nanocarriers. Hybrid systems like lipid-polymer capsules may offer an optimal balance of drug loading efficiency and environmental resilience.

In conclusion, the continued evolution of FB technologies, particularly through the sophisticated application of ERFs, will be instrumental in advancing drug delivery and diagnostics. As these imaging tools converge with nanotechnology and computational sciences, they are expected to drive the development of highly targeted, efficient, and personalized therapeutic strategies. This integration heralds a new era in precision medicine, where nanocarrier systems can be finely tuned to individual patient needs, improving both therapeutic outcomes and clinical care.

Acknowledgments

This work was financially supported by the National Natural Science Foundation of China (Nos. 82273867 and 82030107) and the Science and Technology Commission of Shanghai Municipality (No. 21430760800, China).

Author contributions

Wei Wu conceived and designed this project. Runtong Zhang wrote the manuscript. Runtong Zhang, Haisheng He and Aun Raza revised the manuscript. Wei Wu and Aun Raza supervised this study. Wei Wu obtained financial supports. Wei Wu edited the manuscript. All of the authors have read and approved the final manuscript.

Conflicts of interest

The authors have no conflicts of interest to declare.

References

1. Liu Q, Zou J, Chen Z, He W, Wu W. Current research trends of nanomedicines. *Acta Pharm Sin B* 2023;**13**:4391−416.
2. Wu W, Li T. Unraveling the *in vivo* fate and cellular pharmacokinetics of drug nanocarriers. *Adv Drug Deliv Rev* 2019;**143**:1−2.
3. Shan X, Gong X, Li J, Wen J, Li Y, Zhang Z. Current approaches of nanomedicines in the market and various stage of clinical translation. *Acta Pharm Sin B* 2022;**12**:3028−48.

4. Germain M, Caputo F, Metcalfe S, Tosi G, Spring K, Åslund AKO, et al. Delivering the power of nanomedicine to patients today. *J Control Release* 2020;**326**:164−71.
5. Wu W, Li T. Deepening the understanding of the *in vivo* and cellular fate of nanocarriers. *Adv Drug Deliv Rev* 2022;**189**:114529.
6. Wilhelm S, Tavares AJ, Dai Q, Ohta S, Audet J, Dvorak HF, et al. Analysis of nanoparticle delivery to tumours. *Nat Rev Mater* 2016;**1**: 16014.
7. Cao M, Zhang K, Zhang S, Wang Y, Chen C. Advanced light source analytical techniques for fxploring the biological behavior and fate of nanomedicines. *ACS Cent Sci* 2022;**8**:1063−80.
8. Hu X, Dong X, Lu Y, Qi J, Zhao W, Wu W. Bioimaging of nanoparticles: the crucial role of discriminating nanoparticles from free probes. *Drug Discov Today* 2017;**22**:382−7.
9. Qi J, Hu X, Dong X, Lu Y, Lu H, Zhao W, et al. Towards more accurate bioimaging of drug nanocarriers: turning aggregation-caused quenching into a useful tool. *Adv Drug Deliv Rev* 2019; **143**:206−25.
10. Nagachinta S, Becker G, Dammicco S, Serrano ME, Leroi N, Bahri MA, et al. Radiolabelling of lipid-based nanocarriers with fluorine-18 for *in vivo* tracking by PET. *Colloids Surf B Biointerfaces* 2020;**188**:110793.
11. Sobhanan J, Rival JV, Anas A, Sidharth Shibu E, Takano Y, Biju V. Luminescent quantum dots: synthesis, optical properties, bioimaging and toxicity. *Adv Drug Deliv Rev* 2023;**197**:114830.
12. Huang Y, Liang J, Fan Z. A review: small organic molecule dual/multi-organelle-targeted fluorescent probes. *Talanta* 2023;**259**: 124529.
13. Sobhanan J, Anas A, Biju V. Nanomaterials for fluorescence and multimodal bioimaging. *Chem Rec* 2023;**23**:e202200253.
14. Yang Y, Xie Y, Zhang F. Second near-infrared window fluorescence nanoprobes for deep-tissue *in vivo* multiplexed bioimaging. *Adv Drug Deliv Rev* 2023;**193**:114697.
15. Olesińska-Mönch M, Deo C. Small-molecule photoswitches for fluorescence bioimaging: engineering and applications. *Chem Commun* 2023;**59**:660−9.
16. Lebreton V, Legeay S, Saulnier P, Lagarce F. Specificity of pharmacokinetic modeling of nanomedicines. *Drug Discov Today* 2021; **26**:2259−68.
17. Klymchenko AS, Liu F, Collot M, Anton N. Dye-loaded nanoemulsions: biomimetic fluorescent nanocarriers for bioimaging and nanomedicine. *Adv Healthc Mater* 2021;**10**:e2001289.
18. Huang H, Ali A, Liu Y, Xie H, Ullah S, Roy S, et al. Advances in image-guided drug delivery for antibacterial therapy. *Adv Drug Deliv Rev* 2023;**192**:114634.
19. Priem B, Tian C, Tang J, Zhao Y, Mulder WJ. Fluorescent nanoparticles for the accurate detection of drug delivery. *Expert Opin Drug Deliv* 2015;**12**:1881−94.
20. Bonnet S, Elfatairi R, Franconi F, Roger E, Legeay S. Organic nanoparticle tracking during pharmacokinetic studies. *Nanomedicine (Lond)* 2021;**16**. 2539-6.
21. Hu H, Yu L, Ding Z, Ding J, Hu Y, Yin Z. Chemo-immunotherapy for chemo-resistance and metastasis of triple-negative breast cancer by combination of iron-oxide nanoparticles and dual-targeting doxorubicin liposomes. *Chin Chem Lett* 2023;**34**:108592.
22. Lin H, Tong Q, Xu J, Li T, Yang A, Sun J, et al. An "IgG-hitchhiking" approach for rapid tumor accumulation and clearance of photosensitizers. *J Control Release* 2023;**356**:242−55.
23. Li P, Wang D, Hu J, Yang X. The role of imaging in targeted delivery of nanomedicine for cancer therapy. *Adv Drug Deliv Rev* 2022;**189**: 114447.
24. Skotland T, Iversen TG, Llorente A, Sandvig K. Biodistribution, pharmacokinetics and excretion studies of intravenously injected nanoparticles and extracellular vesicles: possibilities and challenges. *Adv Drug Deliv Rev* 2022;**186**:114326.
25. Perrigue PM, Murray RA, Mielcarek A, Henschke A, Moya SE. Degradation of drug delivery nanocarriers and payload release: a review of physical methods for tracing nanocarrier biological fate. *Pharmaceutics* 2021;**13**:770.
26. Kush P, Kumar P, Singh R, Kaushik A. Aspects of high-performance and bio-acceptable magnetic nanoparticles for biomedical application. *Asian J Pharm Sci* 2021;**16**:704−37.
27. Ding H, Wu F. Image guided biodistribution and pharmacokinetic studies of theranostics. *Theranostics* 2012;**2**:1040−53.
28. Priester MI, Ten Hagen TLM. Image-guided drug delivery in nanosystem-based cancer therapies. *Adv Drug Deliv Rev* 2023;**192**: 114621.
29. Cai Y, Qi J, Lu Y, He H, Wu W. The *in vivo* fate of polymeric micelles. *Adv Drug Deliv Rev* 2022;**188**:114463.
30. Feliu N, Docter D, Heine M, del Pino P, Ashraf S, Kolosnjaj-Tabi J, et al. *In vivo* degeneration and the fate of inorganic nanoparticles. *Chem Soc Rev* 2016;**45**:2440−57.
31. Pratiwi FW, Kuo CW, Chen BC, Chen P. Recent advances in the use of fluorescent nanoparticles for bioimaging. *Nanomedicine (Lond)* 2019;**14**:1759−69.
32. Qi JP, Hu XW, Dong XC, Lu Y, Lu HP, Zhao WL, et al. Towards more accurate bioimaging of drug nanocarriers: turning aggregation-caused quenching into a useful tool. *Adv Drug Deliv Rev* 2019;**143**: 206−25.
33. Hu X, Zhang J, Yu Z, Xie Y, He H, Qi J, et al. Environment-responsive aza-BODIPY dyes quenching in water as potential probes to visualize the *in vivo* fate of lipid-based nanocarriers. *Nanomedicine* 2015;**11**:1939−48.
34. Fang Z, Zhu Z, Zhuang Z, Li Z, Yan C, Yang M, et al. Cascade biomimetic intelligent nanotheranostic agents for imaging-guided tumor synergistic therapy. *Nanomedicine (Lond)* 2023;**18**: 35−52.
35. Hu X, Zhang M, Xue Q, Cai T. ATP aptamer-modified quantum dots with reduced glutathione/adenosine triphosphate dual response features as a potential probe for intracellular drug delivery monitoring of vesicular nanocarriers. *J Biomed Nanotechnol* 2019;**15**:319−28.
36. Lainé AL, Gravier J, Henry M, Sancey L, Béjaud J, Pancani E, et al. Conventional *versus* stealth lipid nanoparticles: formulation and *in vivo* fate prediction through FRET monitoring. *J Control Release* 2014;**188**:1−8.
37. Lacroix A, Vengut-Climent E, de Rochambeau D, Sleiman HF. Uptake and fate of fluorescently labeled DNA nanostructures in cellular environments: a cautionary tale. *ACS Cent Sci* 2019;**5**:882−91.
38. Lebreton V, Kaeokhamloed N, Vasylaki A, Hilairet G, Mellinger A, Béjaud J, et al. Pharmacokinetics of intact lipid nanocapsules using new quantitative FRET technique. *J Control Release* 2022;**351**: 681−91.
39. He HS, Zhang J, Xie YC, Lu Y, Qi JP, Ahmad E, et al. Bioimaging of intravenous polymeric micelles based on discrimination of integral particles using an environment-responsive probe. *Mol Pharm* 2016; **13**:4013−9.
40. Fan W, Peng H, Yu Z, Wang L, He H, Ma Y, et al. The long-circulating effect of pegylated nanoparticles revisited *via* simultaneous monitoring of both the drug payloads and nanocarriers. *Acta Pharm Sin B* 2022;**12**:2479−93.
41. Cayre F, Mura S, Andreiuk B, Sobot D, Gouazou S, Desmaële D, et al. *In vivo* FRET imaging to predict the risk associated with hepatic accumulation of squalene-based prodrug nanoparticles. *Adv Healthc Mater* 2018;**7**:1700830.
42. Zoya I, He H, Wang L, Qi J, Lu Y, Wu W. The intragastrointestinal fate of paclitaxel-loaded micelles: implications on oral drug delivery. *Chin Chem Lett* 2021;**32**:1545−9.
43. Cai Y, Ji X, Zhang Y, Liu C, Zhang Z, Lv Y, et al. Near-infrared fluorophores with absolute aggregation-caused quenching and negligible fluorescence re-illumination for *in vivo* bioimaging of nanocarriers. *Aggregate* 2023;**4**:e277.
44. Wang YF, Zhang C, Yang K, Wang Y, Shan S, Yan Y, et al. Transportation of AIE-visualized nanoliposomes is dominated by the protein corona. *Natl Sci Rev* 2021;**8**:nwab068.

45. Wang Y, Zhang Y, Wang J, Liang XJ. Aggregation-induced emission (AIE) fluorophores as imaging tools to trace the biological fate of nano-based drug delivery systems. *Adv Drug Deliv Rev* 2019;**143**: 161−76.
46. Zhang J, Corpstein CD, Li T. Intracellular uptake of nanocrystals: probing with aggregation-induced emission of fluorescence and kinetic modeling. *Acta Pharm Sin B* 2021;**11**:1021−9.
47. Yin X, Cheng Y, Feng Y, Stiles WR, Park SH, Kang H, et al. Phototheranostics for multifunctional treatment of cancer with fluorescence imaging. *Adv Drug Deliv Rev* 2022;**189**:114483.
48. Haroon HB, Hunter AC, Farhangrazi ZS, Moghimi SM. A brief history of long circulating nanoparticles. *Adv Drug Deliv Rev* 2022; **188**:114396.
49. Wei M, Bai J, Shen X, Lou K, Gao Y, Lv R, et al. Glutathione-exhausting nanoprobes for NIR-II fluorescence imaging-guided surgery and boosting radiation therapy efficacy *via* ferroptosis in breast cancer. *ACS Nano* 2023;**17**:11345−61.
50. Hollis CP, Weiss HL, Leggas M, Evers BM, Gemeinhart RA, Li T. Biodistribution and bioimaging studies of hybrid paclitaxel nanocrystals: lessons learned of the EPR effect and image-guided drug delivery. *J Control Release* 2013;**172**:12−21.
51. Wang X, Chen S, Jia Y, Zhang K, Ma L, Li L, et al. Construction of AIEgen functionalized nanomicelles and their stability study through 'seesaw-like' fluorescence changes. *Chin Chem Lett* 2023;**34**: 107866.
52. He H, Wang L, Ma Y, Yang Y, Lv Y, Zhang Z, et al. The biological fate of orally administered mPEG-PDLLA polymeric micelles. *J Control Release* 2020;**327**:725−36.
53. Guimarães D, Cavaco-Paulo A, Nogueira E. Design of liposomes as drug delivery system for therapeutic applications. *Int J Pharm* 2021; **601**:120571.
54. He Y, Zhang W, Xiao Q, Fan L, Huang D, Chen W, et al. Liposomes and liposome-like nanoparticles: from anti-fungal infection to the COVID-19 pandemic treatment. *Asian J Pharm Sci* 2022; **17**:817−37.
55. Kalhapure RS, Palekar S, Patel K, Monpara J. Nanocrystals for controlled delivery: state of the art and approved drug products. *Expert Opin Drug Deliv* 2022;**19**:1303−16.
56. Huang Y, Hsu JC, Koo H, Cormode DP. Repurposing ferumoxytol: diagnostic and therapeutic applications of an FDA-approved nanoparticle. *Theranostics* 2022;**12**:796−816.
57. Cortajarena AL, Ortega D, Ocampo SM, Gonzalez-García A, Couleaud P, Miranda R, et al. Engineering iron oxide nanoparticles for clinical settings. *Nanobiomedicine (Rij)* 2014;**1**:2.
58. Lu J, Zhu X, Zhang M, Jiang X, Guo W, Jiang F, et al. *In vitro* and *in vivo* assessment of structural integrity for HPCD complex@ Liposome nanocomposites from ocular surface to the posterior segment of the eye. *Carbohydr Polym* 2023;**315**:120960.
59. Li C, Huang J, Yuan L, Xie W, Ying Y, Li C, et al. Recent progress of emitting long-wavelength carbon dots and their merits for visualization tracking, target delivery and theranostics. *Theranostics* 2023; **13**:3064−102.
60. Luo H, Lu L, Liu N, Li Q, Yang X, Zhang Z. Curcumin loaded sub-30 nm targeting therapeutic lipid nanoparticles for synergistically blocking nasopharyngeal cancer growth and metastasis. *J Nanobiotechnol* 2021;**19**:224.
61. Shi T, Lv Y, Huang W, Fang Z, Qi J, Chen Z, et al. Enhanced transdermal delivery of curcumin nanosuspensions: a mechanistic study based on co-localization of particle and drug signals. *Int J Pharm* 2020;**588**:119737.
62. Zhen S, Xu Z, Suo M, Zhang T, Lyu M, Li T, et al. NIR-II AIE liposomes for boosting type-I photodynamic and mild-temperature photothermal therapy in breast cancer treatment. *Adv Mater* 2025; **37**:e2411133.
63. Zhan Y, Chang Z, Liu C, Zhang Z, Zhang R, Lu Y, et al. Tracking *in vivo* lipolysis of lipid nanocarriers using NIR-II polarity-sensitive fluorescent probes. *Small Methods* 2025;**9**:e2402249.
64. Bastiat G, Pritz CO, Roider C, Fouchet F, Lignières E, Jesacher A, et al. A new tool to ensure the fluorescent dye labeling stability of nanocarriers: a real challenge for fluorescence imaging. *J Control Release* 2013;**170**:334−42.
65. Sun X, Wang G, Zhang H, Hu S, Liu X, Tang J, et al. The blood clearance kinetics and pathway of polymeric micelles in cancer drug delivery. *ACS Nano* 2018;**12**:6179−92.
66. Yuan YR, Liu Q, Wang D, Deng YD, Du TT, Yi WJ, et al. GSH-activatable aggregation-induced emission cationic lipid for efficient gene delivery. *Molecules* 2023;**28**:1645.
67. Liu W, Li D, Dong Z, Liu K, He H, Lu Y, et al. Insight into the *in vivo* translocation of oral liposomes by fluorescence resonance energy transfer effect. *Int J Pharm* 2020;**587**:119682.
68. Wang W, Shao A, Feng S, Ding M, Luo G. Physicochemical characterization and gastrointestinal adhesion of *S*-layer proteins-coating liposomes. *Int J Pharm* 2017;**529**:227−37.
69. Chen J, Zhang B, Xia F, Xie Y, Jiang S, Su R, et al. Transmembrane delivery of anticancer drugs through self-assembly of cyclic peptide nanotubes. *Nanoscale* 2016;**8**:7127−36.
70. Yu Z, Fan W, Wang L, He H, Lv Y, Qi J, et al. Slowing down lipolysis significantly enhances the oral absorption of intact solid lipid nanoparticles. *Biomater Sci* 2019;**7**:4273−82.
71. Zhao Y, van Rooy I, Hak S, Fay F, Tang J, Davies CdL, et al. Near-infrared fluorescence energy transfer imaging of nanoparticle accumulation and dissociation kinetics in tumor-bearing mice. *ACS Nano* 2013;**7**:10362−70.
72. Mata Corral MY, Alvarez DE, Poon W. Quantifying nanoparticle delivery: challenges, tools, and advances. *Curr Opin Biotechnol* 2023;**85**:103042.
73. Cao H, Cheng Y, Gao H, Zhuang J, Zhang W, Bian Q, et al. *In vivo* tracking of mesenchymal stem cell-derived extracellular vesicles improving mitochondrial function in renal ischemia-reperfusion injury. *ACS Nano* 2020;**14**:4014−26.
74. Chu B, Chen Z, Shi H, Wu X, Wang H, Dong F, et al. Fluorescence, ultrasonic and photoacoustic imaging for analysis and diagnosis of diseases. *Chem Commun* 2023;**59**:2399−412.
75. Zhou Y, Dong H, Gu Z, Yang S, Ouyang M, Qing Z, et al. Self-immolative dye-doped polymeric probe for precisely imaging hydroxyl radicals by avoiding leakage. *Anal Chem* 2021;**93**: 12944−53.
76. Khalin I, Adarsh N, Schifferer M, Wehn A, Boide-Trujillo VJ, Mamrak U, et al. Nanocarrier drug release and blood−brain barrier penetration at post-stroke microthrombi monitored by real-time förster resonance energy transfer. *ACS Nano* 2025;**19**:14780−94.
77. Sahoo H. Förster resonance energy transfer—a spectroscopic nanoruler: principle and applications. *J Photochem Photobiol C Photochem Rev* 2011;**12**:20−30.
78. Sekatskii SK. Fluorescence resonance energy transfer scanning near-field optical microscopy. *Philos Trans A Math Phys Eng Sci* 2004; **362**:901−19.
79. Zhu X, Li S, Huang J, Yin C, Li Y, Guo W, et al. FRET-based analysis on the fate of liposome and cyclodextrin@liposome nanocomposites from ocular surface to the posterior segment of the eye. *J Control Release* 2025;**377**:794−809.
80. Haustein E, Jahnz M, Schwille P. Triple FRET: a tool for studying long-range molecular interactions. *ChemPhysChem* 2003;**4**:745−8.
81. Aneja A, Mathur N, Bhatnagar PK, Mathur PC. Triple-FRET technique for energy transfer between conjugated polymer and TAMRA Dye with possible applications in medical diagnostics. *J Biol Phys* 2008;**34**:487−93.
82. Wagh A, Jyoti F, Mallik S, Qian S, Leclerc E, Law B. Polymeric nanoparticles with sequential and multiple FRET cascade mechanisms for multicolor and multiplexed imaging. *Small* 2013;**9**:2129−39.
83. Chen T, He B, Tao J, He Y, Deng H, Wang X, et al. Application of förster Resonance energy transfer (FRET) technique to elucidate intracellular and *in vivo* biofate of nanomedicines. *Adv Drug Deliv Rev* 2019;**143**:177−205.

84. Fujimoto KJ, Miyashita T, Dewa T, Yanai T. Determination of FRET orientation factor between artificial fluorophore and photosynthetic light-harvesting 2 complex (LH2). *Sci Rep* 2022;**12**:15091.
85. Bader AN, Hoetzl S, Hofman EG, Voortman J, van Bergen en Henegouwen PM, van Meer G, et al. Homo-FRET imaging as a tool to quantify protein and lipid clustering. *ChemPhysChem* 2011;**12**: 475−83.
86. Deal J, Pleshinger DJ, Johnson SC, Leavesley SJ, Rich TC. Milestones in the development and implementation of FRET-based sensors of intracellular signals: a biological perspective of the history of FRET. *Cell Signal* 2020;**75**:109769.
87. Wu L, Huang C, Emery BP, Sedgwick AC, Bull SD, He XP, et al. Förster resonance energy transfer (FRET)-based small-molecule sensors and imaging agents. *Chem Soc Rev* 2020;**49**:5110−39.
88. Haugland RP, Yguerabide J, Stryer L. Dependence of the kinetics of singlet-singlet energy transfer on spectral overlap. *Proc Natl Acad Sci U S A* 1969;**63**:23−30.
89. Stryer L. Fluorescence energy transfer as a spectroscopic ruler. *Annu Rev Biochem* 1978;**47**:819−46.
90. Mokaberi P, Babayan-Mashhadi F, Zadeh ZAT, Saberi MR, Chamani J. Analysis of the interaction behavior between nanocurcumin and two human serum proteins: combining spectroscopy and molecular stimulation to understand protein−protein interaction. *J Biomol Struct Dyn* 2021;**39**:3358−77.
91. Murade CU, Shubeita GT. A fluorescent reporter on electrostatic DNA−ligand interactions. *Biomed Opt Express* 2022;**13**: 159−67.
92. Agam G, Gebhardt C, Popara M, Mschtel R, Folz J, Ambrose B, et al. Reliability and accuracy of single-molecule FRET studies for characterization of structural dynamics and distances in proteins. *Nat Methods* 2023;**20**:523−35.
93. Sahoo H, Roccatano D, Zacharias M, Nau WM. Distance distributions of short polypeptides recovered by fluorescence resonance energy transfer in the 10 A domain. *J Am Chem Soc* 2006;**128**:8118−9.
94. Sahoo H, Schwille P. FRET and FCS—friends or foes?. *ChemPhysChem* 2011;**12**:532−41.
95. Zaza C, Chiarelli G, Zweifel LP, Pilo-Pais M, Sisamakis E, Barachati F, et al. Super-resolved FRET imaging by confocal fluorescence-lifetime single-molecule localization microscopy. *Small Methods* 2023;**7**:e2201565.
96. Liu L, Shao M, Dong X, Yu X, Liu Z, He Z, et al. Homogeneous immunoassay based on two-photon excitation fluorescence resonance energy transfer. *Anal Chem* 2008;**80**:7735−41.
97. Yuan L, Lin W, Xie Y, Chen B, Zhu S. Single fluorescent probe responds to H_2O_2, NO, and H_2O_2/NO with three different sets of fluorescence signals. *J Am Chem Soc* 2012;**134**:1305−15.
98. Su J, Wu C, Zou J, Wang X, Yang K, Liu J, et al. Fine-tuning of liposome integrity for differentiated transcytosis and enhanced antitumor efficacy. *J Control Release* 2024;**372**:69−84.
99. Zhang H, Li H, Cao Z, Du J, Yan L, Wang J. Investigation of the *in vivo* integrity of polymeric micelles *via* large stokes shift fluorophore-based FRET. *J Control Release* 2020;**324**:47−54.
100. Bouchaala R, Mercier L, Andreiuk B, Mély Y, Vandamme T, Anton N, et al. Integrity of lipid nanocarriers in bloodstream and tumor quantified by near-infrared ratiometric FRET imaging in living mice. *J Control Release* 2016;**236**:57−67.
101. Förster T. Energy migration and fluorescence. 1946. *J Biomed Opt* 2012;**17**:011002.
102. Wu PG, Brand L. Resonance energy transfer: methods and applications. *Anal Biochem* 1994;**218**:1−13.
103. Chen H, Puhl 3rd HL, Koushik SV, Vogel SS, Ikeda SR. Measurement of FRET efficiency and ratio of donor to acceptor concentration in living cells. *Biophys J* 2006;**91**:L39−41.
104. Müller BK, Zaychikov E, Bräuchle C, Lamb DC. Pulsed interleaved excitation. *Biophys J* 2005;**89**:3508−22.
105. Sekar RB, Periasamy A. Fluorescence resonance energy transfer (FRET) microscopy imaging of live cell protein localizations. *J Cell Biol* 2003;**160**:629−33.
106. Bastiaens PI, Squire A. Fluorescence lifetime imaging microscopy: spatial resolution of biochemical processes in the cell. *Trends Cell Biol* 1999;**9**:48−52.
107. Zal T, Gascoigne NR. Photobleaching-corrected FRET efficiency imaging of live cells. *Biophys J* 2004;**86**:3923−39.
108. Hoppe A, Christensen K, Swanson JA. Fluorescence resonance energy transfer-based stoichiometry in living cells. *Biophys J* 2002;**83**: 3652−64.
109. Zimmermann T, Rietdorf J, Pepperkok R. Spectral imaging and its applications in live cell microscopy. *FEBS Lett* 2003;**546**:87−92.
110. Thaler C, Koushik SV, Blank PS, Vogel SS. Quantitative multiphoton spectral imaging and its use for measuring resonance energy transfer. *Biophys J* 2005;**89**:2736−49.
111. Runnels LW, Scarlata SF. Theory and application of fluorescence homotransfer to melittin oligomerization. *Biophys J* 1995;**69**: 1569−83.
112. Groo AC, Saulnier P, Gimel JC, Gravier J, Ailhas C, Benoit JP, et al. Fate of paclitaxel lipid nanocapsules in intestinal mucus in view of their oral delivery. *Int J Nanomed* 2013;**8**:4291−302.
113. Lu KY, Lin CW, Hsu CH, Ho YC, Chuang EY, Sung HW, et al. FRET-based dual-emission and pH-responsive nanocarriers for enhanced delivery of potein across intestinal epithelial cell barrier. *ACS Appl Mater Interfaces* 2014;**6**:18275−89.
114. Lu J, Owen SC, Shoichet MS. Stability of self-assembled polymeric micelles in serum. *Macromolecules* 2011;**44**:6002−8.
115. Guo MR, Chen HN, Zhang C, Zhang GS, Wang YZ, Li PC, et al. Probing the particle shape effects on the biodistribution and antihyperlipidemic efficiency for oral lovastatin nanocrystals. *J Mol Liq* 2021;**324**:114700.
116. Nuhn L, Van Herck S, Best A, Deswarte K, Kokkinopoulou M, Lieberwirth I, et al. FRET Monitoring of intracellular ketal hydrolysis in synthetic nanoparticles. *Angew Chem Int Ed Engl* 2018;**57**: 10760−4.
117. Zhang G, Wang Y, Zhang Z, He Z, Liu Y, Fu Q. FRET imaging revealed that nanocrystals enhanced drug oral absorption by dissolution rather than endocytosis: a case study of coumarin 6. *J Control Release* 2021;**332**:225−32.
118. Wolf MP, Liu KG, Horn TFW, Hunziker P. FRET in a polymeric nanocarrier: IR-780 and IR-780-PDMS. *Biomacromolecules* 2019; **20**:4065−74.
119. Kilin VN, Anton H, Anton N, Steed E, Vermot J, Vandamme TF, et al. Counterion-enhanced cyanine dye loading into lipid nano-droplets for single-particle tracking in zebrafish. *Biomaterials* 2014;**35**: 4950−7.
120. Zhang D, Wen Y, Xiao Y, Yu G, Liu Y, Qian X. Bulky 4-tritylphenylethynyl substituted boradiazaindacene: pure red emission, relatively large stokes shift and inhibition of self-quenching. *Chem Commun* 2008;**39**:4777−9.
121. Sednev MV, Belov VN, Hell SW. Fluorescent dyes with large stokes shifts for super-resolution optical microscopy of biological objects: a review. *Methods Appl Fluoresc* 2015;**3**:042004.
122. Yang L, Liu Y, Ma C, Liu W, Li Y, Li L. Naphthalene-fused BODIPY with large stokes shift as saturated-red fluorescent dye for living cell imaging. *Dyes Pigments* 2015;**122**:1−5.
123. Berlier JE, Rothe A, Buller G, Bradford J, Gray DR, Filanoski BJ, et al. Quantitative comparison of long-wavelength Alexa Fluor dyes to Cy dyes: fluorescence of the dyes and their bioconjugates. *J Histochem Cytochem* 2003;**51**:1699−712.
124. Wu CH, Nhien PQ, Cuc TTK, Hue BTB, Lin HC. Designs and applications of multi-stimuli responsive FRET processes in AIEgen-functionalized and bi-fluorophoric supramolecular materials. *Top Curr Chem* 2022;**381**:2.
125. Gravier J, Sancey L, Hirsjärvi S, Rustique E, Passirani C, Benoît JP, et al. FRET imaging approaches for *in vitro* and *in vivo* characterization of synthetic lipid nanoparticles. *Mol Pharm* 2014;**11**: 3133−44.
126. Garg SM, Paiva IM, Vakili MR, Soudy R, Agopsowicz K, Soleimani AH, et al. Traceable PEO-poly(ester) micelles for breast

cancer targeting: the effect of core structure and targeting peptide on micellar tumor accumulation. *Biomaterials* 2017;**144**:17−29.
127. Fang Y, Jiang Y, Zou Y, Meng F, Zhang J, Deng C, et al. Targeted glioma chemotherapy by cyclic RGD peptide-functionalized reversibly core-crosslinked multifunctional poly(ethylene glycol)-*b*-poly (*ε*-caprolactone) micelles. *Acta Biomater* 2017;**50**:396−406.
128. Lee SY, Tyler JY, Kim S, Park K, Cheng JX. FRET imaging reveals different cellular entry routes of self-assembled and disulfide bonded polymeric micelles. *Mol Pharm* 2013;**10**:3497−506.
129. Tao J, Wei Z, He Y, Yan X, Ming-Yuen Lee S, Wang X, et al. Toward understanding the prolonged circulation and elimination mechanism of crosslinked polymeric micelles in zebrafish model. *Biomaterials* 2020;**256**:120180.
130. Guo C, Yuan H, Yu Y, Gao Z, Zhang Y, Yin T, et al. FRET-based analysis on the structural stability of polymeric micelles: another key attribute beyond PEG coverage and particle size affecting the blood clearance. *J Control Release* 2023;**360**:734−46.
131. Xiong S, Liu W, Li D, Chen X, Liu F, Yuan D, et al. Oral delivery of puerarin nanocrystals to improve brain accumulation and anti-parkinsonian efficacy. *Mol Pharm* 2019;**16**:1444−55.
132. Deng F, Zhang H, Wang X, Zhang Y, Hu H, Song S, et al. Transmembrane pathways and mechanisms of rod-like paclitaxel nanocrystals through MDCK polarized monolayer. *ACS Appl Mater Interfaces* 2017;**9**:5803−16.
133. Guo M, Wei M, Li W, Guo M, Guo C, Ma M, et al. Impacts of particle shapes on the oral delivery of drug nanocrystals: mucus permeation, transepithelial transport and bioavailability. *J Control Release* 2019;**307**:64−75.
134. Lee KR, Kang IJ. Effects of dopamine concentration on energy transfer between dendrimer-QD and dye-labeled antibody. *Ultramicroscopy* 2009;**109**:894−8.
135. Liu Y, Yang G, Jin S, Zhang R, Chen P, Tengjisi, et al. J-aggregate-based FRET monitoring of drug release from polymer nanoparticles with high drug loading. *Angew Chem Int Ed Engl* 2020;**59**: 20065−74.
136. Li H, Chen M, Su Z, Sun M, Ping Q. Size-exclusive effect of nanostructured lipid carriers on oral drug delivery. *Int J Pharm* 2016; **511**:524−37.
137. Ng KK, Takada M, Jin CCS, Zheng G. Self-sensing porphysomes for fluorescence-guided photothermal therapy. *Bioconjug Chem* 2015;**26**: 345−51.
138. Nguyen HTP, Allard-Vannier E, Gaillard C, Eddaoudi I, Miloudi L, Soucé M, et al. On the interaction of alginate-based core-shell nanocarriers with keratinocytes *in vitro*. *Colloids Surf B Biointerfaces* 2016;**142**:272−80.
139. Dai T, Jiang K, Lu W. Liposomes and lipid disks traverse the BBB and BBTB as intact forms as revealed by two-step Förster resonance energy transfer imaging. *Acta Pharm Sin B* 2018;**8**:261−71.
140. Duo Y, Luo G, Zhang W, Wang R, Xiao GG, Li Z, et al. Non-cancerous disease-targeting AIEgens. *Chem Soc Rev* 2023;**52**: 1024−67.
141. Huang Y, Xing J, Gong Q, Chen LC, Liu G, Yao C, et al. Reducing aggregation caused quenching effect through co-assembly of PAH chromophores and molecular barriers. *Nat Commun* 2019;**10**:169.
142. Luo J, Xie Z, Lam JWY, Cheng L, Chen H, Qiu C, et al. Aggregation-induced emission of 1-methyl-1,2,3,4,5-pentaphenylsilole. *Chem Commun* 2001;**18**:1740−1.
143. Wang Y, Xia B, Huang Q, Luo T, Zhang Y, Timashev P, et al. Practicable applications of aggregation-induced emission with biomedical perspective. *Adv Healthc Mater* 2021;**10**:e2100945.
144. Yuan WZ, Lu P, Chen S, Lam JW, Wang Z, Liu Y, et al. Changing the behavior of chromophores from aggregation-caused quenching to aggregation-induced emission: development of highly efficient light emitters in the solid state. *Adv Mater* 2010;**22**:2159−63.
145. Ethirajan M, Chen Y, Joshi P, Pandey RK. The role of porphyrin chemistry in tumor imaging and photodynamic therapy. *Chem Soc Rev* 2011;**40**:340−62.
146. Chen M, Zhang X, Liu J, Liu F, Zhang R, Wei P, et al. Evoking photothermy by capturing intramolecular bond stretching vibration-induced dark-state energy. *ACS Nano* 2020;**14**:4265−75.
147. Qi J, Fang Y, Kwok RTK, Zhang X, Hu X, Lam JWY, et al. Highly stable organic small molecular nanoparticles as an advanced and biocompatible phototheranostic agent of tumor in living mice. *ACS Nano* 2017;**11**:7177−88.
148. Zhang Z, Xu W, Kang M, Wen H, Guo H, Zhang P, et al. An all-round athlete on the track of phototheranostics: subtly regulating the balance between radiative and nonradiative decays for multimodal imaging-guided synergistic therapy. *Adv Mater* 2020;**32**: 2003210.
149. Leung NL, Xie N, Yuan W, Liu Y, Wu Q, Peng Q, et al. Restriction of intramolecular motions: the general mechanism behind aggregation-induced emission. *Chem Eur J* 2014;**20**:15349−53.
150. Chen Y, Lam JWY, Kwok RTK, Liu B, Tang BZ. Aggregation-induced emission: fundamental understanding and future developments. *Mater Horiz* 2019;**6**:428−33.
151. Zhang T, Jiang Y, Niu Y, Wang D, Peng Q, Shuai Z. Aggregation effects on the optical emission of 1,1,2,3,4,5-hexaphenylsilole (HPS): a QM/MM study. *J Phys Chem A* 2014;**118**:9094−104.
152. Peng Q, Yi Y, Shuai Z, Shao J. Toward quantitative prediction of molecular fluorescence quantum efficiency: role of duschinsky rotation. *J Am Chem Soc* 2007;**129**:9333−9.
153. Mei J, Leung NL, Kwok RT, Lam JW, Tang BZ. Aggregation-induced emission: together we shine, united we soar. *Chem Rev* 2015;**115**:11718−940.
154. Xiong JB, Yuan YX, Wang L, Sun JP, Qiao WG, Zhang HC, et al. Evidence for aggregation-induced emission from free rotation restriction of double bond at excited state. *Org Lett* 2018;**20**:373−6.
155. Sasaki S, Suzuki S, Sameera WM, Igawa K, Morokuma K, Konishi G. Highly twisted *N,N*-dialkylamines as a design strategy to tune simple aromatic hydrocarbons as steric environment-sensitive fluorophores. *J Am Chem Soc* 2016;**138**:8194−206.
156. Li Q, Blancafort L. A conical intersection model to explain aggregation induced emission in diphenyl dibenzofulvene. *Chem Commun* 2013;**49**:5966−8.
157. Mei J, Hong Y, Lam JW, Qin A, Tang Y, Tang BZ. Aggregation-induced emission: the whole is more brilliant than the parts. *Adv Mater* 2014;**26**:5429−79.
158. He Z, Ke C, Tang BZ. Journey of aggregation-induced emission research. *ACS Omega* 2018;**3**:3267−77.
159. Zhou Q, Cao B, Zhu C, Xu S, Gong Y, Yuan WZ, et al. Clustering-triggered emission of nonconjugated polyacrylonitrile. *Small* 2016; **12**:6586−92.
160. Zhang H, Zheng X, Xie N, He Z, Liu J, Leung NLC, et al. Why do simple molecules with "Isolated" phenyl rings emit visible light?. *J Am Chem Soc* 2017;**139**:16264−72.
161. Dong Y, Lam JWY, Qin A, Li Z, Sun J, Sung HH, et al. Switching the light emission of (4-biphenylyl)phenyldibenzofulvene by morphological modulation: crystallization-induced emission enhancement. *Chem Commun* 2007;(1):40−2.
162. Cheng X, Li D, Zhang Z, Zhang H, Wang Y. Organoboron compounds with morphology-dependent NIR emissions and dual-channel fluorescent ON/OFF switching. *Org Lett* 2014;**16**:880−3.
163. Zheng X, Peng Q, Zhu L, Xie Y, Huang X, Shuai Z. Unraveling the aggregation effect on amorphous phase AIE luminogens: a computational study. *Nanoscale* 2016;**8**:15173−80.
164. Dong Y, Lam JWY, Qin A, Sun J, Liu J, Li Z, et al. Aggregation-induced and crystallization-enhanced emissions of 1,2-diphenyl-3,4-bis(diphenylmethylene)-1-cyclobutene. *Chem Commun* 2007: 3255−7.
165. Qian EA, Wixtrom AI, Axtell JC, Saebi A, Jung D, Rehak P, et al. Atomically precise organomimetic cluster nanomolecules assembled *via* perfluoroaryl-thiol S_NAr chemistry. *Nat Chem* 2017;**9**: 333−40.
166. Du L, Wang P, Huang H, Li M, Roy S, Zhang Y, et al. Light-activatable and hyperthermia-sensitive "all-in-one" theranostics: NIR-II

fluorescence imaging and chemo-photothermal therapy of subcutaneous glioblastoma by temperature-sensitive liposome-containing AIEgens and paclitaxel. *Front Bioeng Biotechnol* 2023;**11**:1343694.
167. Wu W, Feng G, Xu S, Liu B. A photostable far-red/near-infrared conjugated polymer photosensitizer with aggregation-induced emission for image-guided cancer cell ablation. *Macromolecules* 2016;**49**: 5017−25.
168. Ning ZW, Wu SZ, Liu GJ, Ji YM, Jia LY, Niu XX, et al. Water-soluble AIE-active fluorescent organic nanoparticles: design, preparation and application for specific detection of cysteine over homocysteine and glutathione in living cells. *Chem Asian J* 2019;**14**: 2220−4.
169. Qi J, Lu Y, Dong X, Zhao W, Wu W. *In vivo* fate study of drug nanocarriers: the applications of environment-responsive fluorescent dyes. *Acta Pharm Sin* 2019;**54**:1965−75.
170. Hu J, Zhuang W, Ma B, Su X, Yu T, Li G, et al. Redox-responsive biomimetic polymeric micelle for simultaneous anticancer drug delivery and aggregation-induced emission active imaging. *Bioconjug Chem* 2018;**29**:1897−910.
171. Liow SS, Dou Q, Kai D, Li Z, Sugiarto S, Yu CY, et al. Long-term real-time *in vivo* drug release monitoring with AIE thermogelling polymer. *Small* 2017;**13**:1603404.
172. Yang K, Li S, Jin S, Xue X, Zhang T, Zhang C, et al. Micelle-like luminescent nanoparticles as a visible gene delivery system with reduced toxicity. *J Mater Chem B* 2015;**3**:8394−400.
173. Yuan Y, Zhang CJ, Liu B. A photoactivatable AIE polymer for light-controlled gene delivery: concurrent endo/lysosomal escape and DNA unpacking. *Angew Chem Int Ed Engl* 2015;**54**: 11419−23.
174. Zhang C, Jin S, Li S, Xue X, Liu J, Huang Y, et al. Imaging intracellular anticancer drug delivery by self-assembly micelles with aggregation-induced emission (AIE micelles). *ACS Appl Mater Interfaces* 2014;**6**:5212−20.
175. Xue X, Jin S, Zhang C, Yang K, Huo S, Chen F, et al. Probe-inspired nano-prodrug with dual-color fluorogenic property reveals spatiotemporal drug release in living cells. *ACS Nano* 2015;**9**:2729−39.
176. Xue X, Xu J, Wang PC, Liang XJ. Subcellular behaviour evaluation of nanopharmaceuticals with aggregation-induced emission molecules. *J Mater Chem C Mater* 2016;**4**:2719−30.
177. Bozeman TC, Edwards KA, Fecteau KM, Verde MG, Blanchard A, Woodall DL, et al. Tolyl-substituted siloles: synthesis, substituent effects, and aggregation-induced emission. *J Inorg Organomet Polym* 2011;**21**:316−26.
178. Wang D, Su H, Kwok RTK, Hu X, Zou H, Luo Q, et al. Rational design of a water-soluble NIR AIEgen, and its application in ultrafast wash-free cellular imaging and photodynamic cancer cell ablation. *Chem Sci* 2018;**9**:3685−93.
179. Liu Y, Kong M, Zhang Q, Zhang Z, Zhou H, Zhang S, et al. A series of triphenylamine-based two-photon absorbing materials with AIE property for biological imaging. *J Mater Chem B* 2014;**2**:5430−40.
180. Chen W, Zhang C, Chen H, Zang K, Liu SH, Xie Y, et al. Near-infrared thienoisoindigos with aggregation-induced emission: molecular design, optical performance, and bioimaging application. *Anal Chem* 2021;**93**:3378−85.
181. Yuan Y, Yin P, Wang T, Yang Z, Yin W, Zhang S, et al. Synthesis of triphenylamine (TPA) dimers and applications in cell imaging. *Dyes Pigments* 2020;**174**:108009.
182. Gómez R, Seoane C, Segura JL. The first two decades of a versatile electron acceptor building block: 11,11,12,12-tetracyano-9,10-anthraquinodimethane (TCAQ). *Chem Soc Rev* 2007;**36**:1305−22.
183. Wu W, Mao D, Hu F, Xu S, Chen C, Zhang CJ, et al. A highly efficient and photostable photosensitizer with near-infrared aggregation-induced emission for image-guided photodynamic anticancer therapy. *Adv Mater* 2017;**29**:1700548.
184. Li Y, Shao A, Wang Y, Mei J, Niu D, Gu J, et al. Morphology-tailoring of a red AIEgen from microsized rods to nanospheres for tumor-targeted bioimaging. *Adv Mater* 2016;**28**:3187−93.
185. Yuan Y, Kwok RTK, Tang BZ, Liu B. Smart probe for tracing cancer therapy: selective cancer cell detection, image-guided ablation, and prediction of therapeutic response *in situ*. *Small* 2015;**11**:4682−90.
186. Yuan Y, Xu S, Zhang CJ, Liu B. Light-responsive AIE nanoparticles with cytosolic drug release to overcome drug resistance in cancer cells. *Polym Chem* 2016;**7**:3530−9.
187. Qin W, Ding D, Liu J, Yuan WZ, Hu Y, Liu B, et al. Biocompatible nanoparticles with aggregation-induced emission characteristics as far-red/near-infrared fluorescent bioprobes for *in vitro* and *in vivo* imaging applications. *Adv Funct Mater* 2012;**22**:771−9.
188. Zhang W, Wen Y, He DX, Wang YF, Liu XL, Li C, et al. Near-infrared AIEgens as transformers to enhance tumor treatment efficacy with controllable self-assembled redox-responsive carrier-free nanodrug. *Biomaterials* 2019;**193**:12−21.
189. Yang C, Ni X, Mao D, Ren C, Liu J, Gao Y, et al. Seeing the fate and mechanism of stem cells in treatment of ionizing radiation-induced injury using highly near-infrared emissive AIE dots. *Biomaterials* 2019;**188**:107−17.
190. Deng G, Peng X, Sun Z, Zheng W, Yu J, Du L, et al. Natural-killer-cell-inspired nanorobots with aggregation-induced emission characteristics for near-infrared-II fluorescence-guided glioma theranostics. *ACS Nano* 2020;**14**:11452−62.
191. Hu R, Leung NLC, Tang BZ. AIE macromolecules: syntheses, structures and functionalities. *Chem Soc Rev* 2014;**43**:4494−562.
192. Chen J, Law CCW, Lam JWY, Dong Y, Lo SMF, Williams ID, et al. Synthesis, light emission, nanoaggregation, and restricted intramolecular rotation of 1,1-substituted 2,3,4,5-tetraphenylsiloles. *Chem Mater* 2003;**15**:1535−46.
193. Liu S, Li Y, Kwok RTK, Lam JWY, Tang BZ. Structural and process controls of AIEgens for NIR-II theranostics. *Chem Sci* 2020;**12**: 3427−36.
194. Tan Y, Liu P, Li D, Wang D, Tang BZ. NIR-II aggregation-induced emission luminogens for tumor phototheranostics. *Biosensors (Basel)* 2022;**12**:46.
195. Wu J, You L, Lan L, Lee HJ, Chaudhry ST, Li R, et al. Semiconducting polymer nanoparticles for centimeters-deep photoacoustic imaging in the second near-infrared window. *Adv Mater* 2017;**29**:1703403.
196. Gao S, Wei G, Zhang S, Zheng B, Xu J, Chen G, et al. Albumin tailoring fluorescence and photothermal conversion effect of near-infrared-II fluorophore with aggregation-induced emission characteristics. *Nat Commun* 2019;**10**:2206.
197. Dave R, Pandey K, Khatri V, Patel R, Gour N, Bhatia D. Biological AIE molecules: innovations in synthetic design and AI-driven discovery. *Adv Biol (Weinh)* 2025:e2400792.
198. Zhang Y, Fan M, Xu Z, Jiang Y, Ding H, Li Z, et al. Machine-learning screening of luminogens with aggregation-induced emission characteristics for fluorescence imaging. *J Nanobiotechnol* 2023;**21**: 107.
199. Shamay Y. Mastering the complexities of cancer nanomedicine with text mining, AI and automation. *J Control Release* 2025;**379**:906−19.
200. Hua H, Deng Y, Zhang J, Zhou X, Zhang T, Khoo BL. AIEgen-deep: deep learning of single AIEgen-imaging pattern for cancer cell discrimination and preclinical diagnosis. *Biosens Bioelectron* 2024; **253**:116086.
201. Daina A, Michielin O, Zoete V. SwissTargetPrediction: updated data and new features for efficient prediction of protein targets of small molecules. *Nucleic Acids Res* 2019;**47**:W357−64.
202. Lotfollahi M, Klimovskaia Susmelj A, De Donno C, Hetzel L, Ji Y, Ibarra IL, et al. Predicting cellular responses to complex perturbations in high-throughput screens. *Mol Syst Biol* 2023;**19**:e11517.
203. Huang Y, Luo C, Xia F, Song Y, Jiang L, Li F. Multi-analyte sensing strategies towards wearable and intelligent devices. *Chem Sci* 2022; **13**:12309−25.
204. Rajpurkar P, Chen E, Banerjee O, Topol EJ. AI in health and medicine. *Nat Med* 2022;**28**:31−8.
205. Zhang K, Yang X, Wang Y, Yu Y, Huang N, Li G, et al. Artificial intelligence in drug development. *Nat Med* 2025;**31**:45−59.

206. Lee MMS, Yu EY, Chau JHC, Lam JWY, Kwok RTK, Tang BZ. Expanding our horizons: AIE materials in bacterial research. *Adv Mater* 2025;**37**:e2407707.
207. Hou YC, Zhang C, Zhang ZJ, Xia L, Rao KQ, Gu LH, et al. Aggregation-induced emission (AIE) and magnetic resonance imaging characteristics for targeted and image-guided siRNA therapy of hepatocellular carcinoma. *Adv Healthc Mater* 2022;**11**: e2200579.
208. Qian Y, Wang Y, Jia F, Wang Z, Yue C, Zhang W, et al. Tumor-microenvironment controlled nanomicelles with AIE property for boosting cancer therapy and apoptosis monitoring. *Biomaterials* 2019;**188**:96−106.
209. Xu M, Wang X, Wang Q, Hu Q, Huang K, Lou X, et al. Analyte-responsive fluorescent probes with AIE characteristic based on the change of covalent bond. *Sci Chin Mater* 2019;**62**: 1236−50.
210. Fang X, Chen X, Li R, Liu Z, Chen H, Sun Z, et al. Multicolor photocrosslinkable AIEgens toward compact nanodots for subcellular imaging and STED nanoscopy. *Small* 2017;**13**:1702128.
211. Cao H, Yue Z, Gao H, Chen C, Cui K, Zhang K, et al. *In vivo* real-time imaging of extracellular vesicles in liver regeneration *via* aggregation-induced emission luminogens. *ACS Nano* 2019;**13**: 3522−33.
212. Gao W, Lee D, Meng Z, Li T. Exploring intracellular fate of drug nanocrystals with crystal-integrated and environment-sensitive fluorophores. *J Control Release* 2017;**267**:214−22.
213. Wang H, Liu G, Gao H, Wang Y. A pH-responsive drug delivery system with an aggregation-induced emission feature for cell imaging and intracellular drug delivery. *Polym Chem* 2015;**6**: 4715−8.
214. Zhuang W, Xu Y, Li G, Hu J, Ma B, Yu T, et al. Redox and pH dual-responsive polymeric micelles with aggregation-induced emission feature for cellular imaging and chemotherapy. *ACS Appl Mater Interfaces* 2018;**10**:18489−98.
215. Zhang J, Li C, Zhang X, Huo S, Jin S, An FF, et al. *In vivo* tumor-targeted dual-modal fluorescence/CT imaging using a nanoprobe co-loaded with an aggregation-induced emission dye and gold nanoparticles. *Biomaterials* 2015;**42**:103−11.
216. Wang X, Yang Y, Yang F, Shen H, Wu D. PH-triggered decomposition of polymeric fluorescent vesicles to induce growth of tetraphenylethylene nanoparticles for long-term live cell imaging. *Polymer* 2017;**118**:75−84.
217. Hu R, Yang C, Wang Y, Lin G, Qin W, Ouyan Q, et al. Aggregation-induced emission (AIE) dye loaded polymer nanoparticles for gene silencing in pancreatic cancer and their *in vitro* and *in vivo* biocompatibility evaluation. *Nano Res* 2015; **8**:1563−76.
218. Yuan Y, Kwok RT, Zhang R, Tang BZ, Liu B. Targeted theranostic prodrugs based on an aggregation-induced emission (AIE) luminogen for real-time dual-drug tracking. *Chem Commun* 2014;**50**: 11465−8.
219. Wang H, Li B, Sun Y, Ma Q, Feng Y, Jia Y, et al. NIR-II AIE luminogen-based erythrocyte-like nanoparticles with granuloma-targeting and self-oxygenation characteristics for combined phototherapy of tuberculosis. *Adv Mater* 2024;**36**:e2406143.
220. Huang H, Li M, Gu J, Roy S, Jin J, Kuang T, et al. Bright NIR-II emissive cyanine dye-loaded lipoprotein-mimicking nanoparticles for fluorescence imaging-guided and targeted NIR-II photothermal therapy of subcutaneous glioblastoma. *J Nanobiotechnol* 2024;**22**: 788.
221. Li M, Gao Y, Yuan Y, Wu Y, Song Z, Tang BZ, et al. One-step formulation of targeted aggregation-induced emission dots for image-guided photodynamic therapy of cholangiocarcinoma. *ACS Nano* 2017;**11**:3922−32.
222. Song S, Zhao Y, Kang M, Zhang F, Wu Q, Niu N, et al. An NIR-II excitable AIE small molecule with multimodal phototheranostic features for orthotopic breast cancer treatment. *Adv Mater* 2024;**36**: 2309748.
223. Zhang C, Zhang T, Jin S, Xue X, Yang X, Gong N, et al. Virus-inspired self-assembled nanofibers with aggregation-induced emission for highly efficient and visible gene delivery. *ACS Appl Mater Interfaces* 2017;**9**:4425−32.
224. Zhang T, Guo W, Zhang C, Yu J, Xu J, Li S, et al. Transferrin-dressed virus-like ternary nanoparticles with aggregation-induced emission for targeted delivery and rapid cytosolic release of siRNA. *ACS Appl Mater Interfaces* 2017;**9**:16006−14.
225. Wang DP, Zheng J, Jiang FY, Wu LF, Wang MY, Wang YL, et al. Facile and green fabrication of tumor- and mitochondria-targeted AIEgen-protein nanoparticles for imaging-guided photodynamic cancer therapy. *Acta Biomater* 2023;**168**:551−64.
226. Zhang L, Wang Z, Zhang R, Yang H, Wang WJ, Zhao Y, et al. Multi-stimuli-responsive and cell membrane camouflaged aggregation-induced emission nanogels for precise chemo-photothermal synergistic therapy of tumors. *ACS Nano* 2023;**17**:25205−21.
227. Lu Y, Lv Y, Li T. Hybrid drug nanocrystals. *Adv Drug Deliv Rev* 2019;**143**:115−33.
228. Ding D, Li K, Liu B, Tang BZ. Bioprobes based on AIE fluorogens. *Acc Chem Res* 2013;**46**:2441−53.
229. He W, Zhang T, Bai H, Kwok RTK, Lam JWY, Tang BZ. Recent advances in aggregation-induced emission materials and their biomedical and healthcare applications. *Adv Healthc Mater* 2021;**10**: e2101055.
230. Benson CR, Kacenauskaite L, VanDenburgh KL, Zhao W, Qiao B, Sadhukhan T, et al. Plug-and-play optical materials from fluorescent dyes and macrocycles. *Chem* 2020;**6**:1978−97.
231. De S, Das G. Exploring the aggregation and light-harvesting aptitude of naphthalimide-based amphiphile and non-amphiphile AIEgen. *Langmuir* 2022;**38**:6158−63.
232. Zhai DT, Xu W, Zhang LY, Chang YT. The role of "disaggregation" in optical probe development. *Chem Soc Rev* 2014;**43**: 2402−11.
233. Spano FC, Silva C. H- and J-Aggregate behavior in polymeric semiconductors. *Annu Rev Phys Chem* 2014;**65**:477−500.
234. Sun Q, Ren JJ, Jiang T, Peng Q, Ou Q, Shuai ZG. Intermolecular charge-transfer-induced strong optical emission from herringbone H-aggregates. *Nano Lett* 2021;**21**:5394−400.
235. Li K, Duan XC, Jiang ZY, Ding D, Chen YC, Zhang GQ, et al. J-Aggregates of meso- 2.2 paracyclophanyl-BODIPY dye for NIR-II imaging. *Nat Commun* 2021;**12**:2376.
236. Sun CX, Li BH, Zhao MY, Wang SF, Lei ZH, Lu LF, et al. J-Aggregates of cyanine dye for NIR-II *in vivo* dynamic vascular imaging beyond 1500 nm. *J Am Chem Soc* 2019;**141**:19221−5.
237. Chakraborty S, Debnath P, Dey D, Bhattacharjee D, Hussain SA. Formation of fluorescent H-aggregates of a cyanine dye in ultrathin film and its effect on energy transfer. *J Photochem Photobiol A Chem* 2014;**293**:57−64.
238. Yu HL, Wang YS, Chen Y, Cui MY, Yang F, Wang P, et al. Transmissible H-aggregated NIR-II fluorophore to the tumor cell membrane for enhanced PTT and synergistic therapy of cancer. *Nano Convergence* 2023;**10**:3.
239. Cao W, Sletten EM. Fluorescent cyanine dye J-aggregates in the fluorous phase. *J Am Chem Soc* 2018;**140**:2727−30.
240. Chen Z, Liu Y, Wagner W, Stepanenko V, Ren X, Ogi S, et al. Near-IR absorbing J-aggregate of an amphiphilic BF_2-azadipyrromethene dye by kinetic cooperative self-assembly. *Angew Chem Int Ed Engl* 2017;**56**:5729−33.
241. Bae W, Yoon TY, Jeong C. Direct evaluation of self-quenching behavior of fluorophores at high concentrations using an evanescent field. *PLoS One* 2021;**16**:e0247326.
242. Wu YL, Wang J, Zeng F, Huang SL, Huang J, Xie HT, et al. Pyrene derivative emitting red or near-infrared light with monomer/excimer conversion and its application to ratiometric detection of hypochlorite. *ACS Appl Mater Interfaces* 2016;**8**: 1511−9.
243. Wang X, Huang J, Guo M, Zhong Y, Huang Z. Aggregation-caused quenching dyes as potent tools to track the integrity of

antitumor nanocarriers: a mini-review. *Pharmaceuticals* 2025;**18**:176.
244. Yu Z, Fan W, Wang L, Qi J, Lu Y, Wu W. Effect of surface charges on oral absorption of intact solid lipid nanoparticles. *Mol Pharm* 2019;**16**:5013−24.
245. Huang Z, Huang Y, Wang W, Fu F, Wang W, Dang S, et al. Relationship between particle size and lung retention time of intact solid lipid nanoparticle suspensions after pulmonary delivery. *J Control Release* 2020;**325**:206−22.
246. Wang T, Qi J, Ding N, Dong X, Zhao W, Lu Y, et al. Tracking translocation of self-discriminating curcumin hybrid nanocrystals following intravenous delivery. *Int J Pharm* 2018;**546**:10−9.
247. Ji X, Cai Y, Dong X, Wu W, Zhao W. Selection of an aggregation-caused quenching-based fluorescent tracer for imaging studies in nano drug delivery systems. *Nanoscale* 2023;**25**:9290−6.
248. Xie Y, Shi B, Xia F, Qi J, Dong X, Zhao W, et al. Epithelia transmembrane transport of orally administered ultrafine drug particles evidenced by environment sensitive fluorophores in cellular and animal studies. *J Control Release* 2018;**270**:65−75.
249. Li Y, Wang C, Zong S, Qi J, Dong X, Zhao W, et al. The trigeminal pathway dominates the nose-to-brain transportation of intact polymeric nanoparticles: evidence from aggregation-caused quenching probes. *J Biomed Nanotechnol* 2019;**15**:686−702.
250. Yoon S, Cheon SY, Park S, Lee D, Lee Y, Han S, et al. Recent advances in optical imaging through deep tissue: imaging probes and techniques. *Biomater Res* 2022;**26**:57.
251. Bashkatov AN, Genina EA, Kochubey VI, Tuchin VV. Optical properties of human skin, subcutaneous and mucous tissues in the wavelength range from 400 to 2000 nm. *J Phys D Appl Phys* 2005;**38**:2543−55.
252. Zhang Z, Liu C, Lu Y, Zhao W, Zhu Q, He H, et al. *In vivo* fluorescence imaging of nanocarriers in near-infrared window II based on aggregation-caused quenching. *J Nanobiotechnol* 2024;**22**:488.
253. Liu C, Cai Y, Zhang Z, Lu Y, Zhu Q, He H, et al. Julolidinyl aza-BODIPYs as NIR-II fluorophores for the bioimaging of nanocarriers. *Acta Pharm Sin B* 2024;**14**:3155−68.
254. Gonçalves MS. Fluorescent labeling of biomolecules with organic probes. *Chem Rev* 2009;**109**:190−212.
255. Liu X, Yang L, Long Q, Weaver D, Hajnóczky G. Choosing proper fluorescent dyes, proteins, and imaging techniques to study mitochondrial dynamics in mammalian cells. *Biophys Rep* 2017;**3**:64−72.
256. Hu X, Fan W, Yu Z, Dong X, Zhao W, Wu W. Evidence does not support absorption of intact solid lipid nanoparticles *via* oral delivery. *Nanoscale* 2016;**8**:7024.
257. Ahmad E, Feng Y, Qi J, Fan W, Ma Y, He H, et al. Evidence of nose-to-brain delivery of nanoemulsions: cargoes but not vehicles. *Nanoscale* 2017;**9**:1174.
258. Su R, Fan W, Yu Q, Dong X, Qi J, Zhu Q, et al. Size-dependent penetration of nanoemulsions into epidermis and hair follicles: implications for transdermal delivery and immunization. *Oncotarget* 2017;**8**:38214−26.
259. Xia F, Fan W, Jiang S, Ma Y, Lu Y, Qi J, et al. Size-dependent translocation of nanoemulsions *via* oral delivery. *ACS Appl Mater Interfaces* 2017;**9**:21660.
260. Cai Y, Zhang Z, Liu C, Tai Z, Zhu Q, Qi J, et al. Size-dependent translocation and lymphatic transportation of polymeric nanocarriers post intraperitoneal administration. *J Control Release* 2024;**376**:553−65.
261. He H, Xie Y, Lv Y, Qi J, Dong X, Zhao W, et al. Bioimaging of intact polycaprolactone nanoparticles using aggregation-caused quenching probes: Size-dependent translocation *via* oral delivery. *Adv Healthc Mater* 2018;**7**:e1800711.
262. Li L, He H, Jiang S, Qi J, Lu Y, Ding N, et al. Simulation of the *in vivo* fate of polymeric nanoparticles traced by environment-responsive near-infrared dye: a physiologically based pharmacokinetic modelling approach. *Molecules* 2021;**26**:1271.
263. Wang W, Yang B, Huang Z, Huang Y, Hu P, Pan X, et al. Investigating the effect of particle size on cellular uptake by aggregation-caused quenching probe−encapsulating solid lipid nanoparticles, inhaled. *J Pharm Innov* 2022;**17**:1109−15.
264. Huang Z, Huang Y, Ma C, Ma X, Zhang X, Lin L, et al. Endotracheal aerosolization device for laboratory investigation of pulmonary delivery of nanoparticle suspensions: *in vitro* and *in vivo* validation. *Mol Pharm* 2018;**15**:5521−33.
265. Wang W, Huang Z, Xue K, Li J, Wang W, Ma J, et al. Development of aggregation-caused quenching probe-loaded pressurized metered-dose inhalers with fluorescence tracking potentials. *AAPS PharmSciTech* 2020;**21**:296.
266. Lv Y, Wu W, Corpstein CD, Li T, Lu Y. Biological and intracellular fates of drug nanocrystals through different delivery routes: recent development enabled by bioimaging and PK modeling. *Adv Drug Deliv Rev* 2022;**188**:114466.
267. Liu D, Wan B, Qi J, Dong X, Zhao W, Wu W, et al. Permeation into but not across the cornea: bioimaging of intact nanoemulsions and nanosuspensions using aggregation-caused quenching probes. *Chin Chem Lett* 2018;**29**:1834−8.
268. Shen C, Yang Y, Shen B, Xie Y, Qi J, Dong X, et al. Self-discriminating fluorescent hybrid nanocrystals: efficient and accurate tracking of translocation *via* oral delivery. *Nanoscale* 2017;**10**:436−50.
269. Yang Y, Lv Y, Shen C, Shi T, He H, Qi J, et al. *In vivo* dissolution of poorly water-soluble drugs: proof of concept based on fluorescence bioimaging. *Acta Pharm Sin B* 2021;**11**:1056−68.
270. Shen B, Shen C, Zhu W, Yuan H. The contribution of absorption of integral nanocrystals to enhancement of oral bioavailability of quercetin. *Acta Pharm Sin B* 2021;**11**:978−88.
271. Hang L, Shen C, Xue Y, Wu W, Shen B, Yuan H. Exploring the translocation behaviours *in vivo* of herpetrione amorphous nanoparticles *via* oral delivery. *J Drug Target* 2023;**31**:278−85.
272. Hang L, Shen C, Shen B, Yuan H. Insight into the *in vivo* fate of intravenous herpetrione amorphous nanosuspensions by aggregation-caused quenching probes. *Chin Chem Lett* 2022;**33**:4948−51.
273. Wang X, Wang X, Qiu L, Ouyang H, Xu W. Cytotoxicity and cellular uptake of paclitaxel-loaded carboxymethyl chitosan-rhein polymeric micelles in MCF-7 cells. *J China Pharm Univ* 2020;**51**:33−7.
274. Wang X, Qiu L, Wang X, Ouyang H, Li T, Han L, et al. Evaluation of intestinal permeation enhancement with carboxymethyl chitosan-rhein polymeric micelles for oral delivery of paclitaxel. *Int J Pharm* 2020;**573**:118840.
275. Wang X, Zheng Y, Qiu L, Ouyang H, Xu X, Xu W, et al. Evaluation and antitumor mechanism of functionalized chitosan-based polymeric micelles for oral delivery of paclitaxel. *Int J Pharm* 2022;**625**:122138.
276. Zhang X, Xu X, Wang X, Lin Y, Zheng Y, Xu W, et al. Hepatoma-targeting and reactive oxygen species-responsive chitosan-based polymeric micelles for delivery of celastrol. *Carbohydr Polym* 2023;**303**:120439.
277. Wu W, Ding Q, Zhou Z, Kuang W, Jiang L, Liu P, et al. Transcellular transport behavior of the intact polymeric mixed micelles with different polymeric ratios. *AAPS PharmSciTech* 2023;**24**:69.
278. Ahmad E, Lv Y, Zhu Q, Qi J, Dong X, Zhao W, et al. TAT modification facilitates nose-to-brain transport of intact mPEG-PDLLA micelles: evidence from aggregation-caused quenching probes. *Appl Mater Today* 2020;**19**:100556.
279. Zhang R, Liu C, Lu R, Yang Y, Zhang Z, Cai Y, et al. Head-to-head comparison between ACQ and FRET in probing polymeric micelles. *View* 2025:20250037.

280. Jiang Y, Liu C, Zhai W, Zhuang N, Han T, Ding Z. The optimization design of lactoferrin loaded HupA nanoemulsion for targeted drug transport *via* intranasal route. *Int J Nanomed* 2019;**14**:9217−34.
281. Jiang Y, Jiang Y, Ding Z, Yu Q. Investigation of the "nose-to-brain" pathways in intranasal HupA nanoemulsions and evaluation of their *in vivo* pharmacokinetics and brain-targeting ability. *Int J Nanomed* 2022;**17**:3443−56.
282. Fan W, Yu Z, Peng H, He H, Lu Y, Qi J, et al. Effect of particle size on the pharmacokinetics and biodistribution of parenteral nanoemulsions. *Int J Pharm* 2020;**586**:119551.
283. Yang J, Dong Z, Liu W, He H, Fan W, Lu Y, et al. Discriminating against injectable fat emulsions with similar formulation based on water quenching fluorescent probe. *Chin Chem Lett* 2020;**31**:875−9.
284. Xia F, Chen Z, Zhu Q, Qi J, Dong X, Zhao W, et al. Gastrointestinal lipolysis and trans-epithelial transport of SMEDDS *via* oral route. *Acta Pharm Sin B* 2021;**11**:1010−20.
285. Zheng XZ, Fang ZZ, Huang WZ, Qi JP, Dong XC, Zhao WL, et al. Ionic co-aggregates (ICAs) based oral drug delivery: solubilization and permeability improvement. *Acta Pharm Sin B* 2022;**12**:3972−85.
286. Fu Y, Shi C, Li X, Wen T, Wu Q, Zhang A, et al. Demonstrating biological fate of nanoparticle-loaded dissolving microneedles with aggregation-caused quenching probes: influence of application sites. *Pharmaceutics* 2023;**15**:169.
287. Shi C, Yang D, Zhao Y, Wen T, Zhao W, Hu P, et al. The spatial-dimensional and temporal-dimensional fate of nanocarrier-loaded dissolving microneedles with different lengths of needles. *Med in Drug Discov* 2022;**14**:100124.